Rotational Optomechanics

Hu, Yanhui

Awarding institution:
King's College London

Rotational Optomechanics

Yanhui Hu

A thesis submitted in partial fulfillment

of the requirements for the degree of

Doctor of Philosophy

Department of Physics

Faculty of Natural, Mathematical & Engineering Sciences

King's College London

September 2022

Declaration

Declaration of Originality

I confirm that no part of the material offered has previously been submitted by myself for a degree in this or any other University. Where material has been generated through joint work, the work of others has been indicated.

Declaration of Copyright

List of Publications

This thesis is based on the following publications and preprints:

- **Direct and clean loading of nanoparticles into optical traps at millibar pressures**

  Maryam Nikkhou[†], Yanhui Hu[†], James A. Sabin, and James Millen

  ([†]*contributed equally*)

  Photonics **8**, 458 (2021)

- **Structured transverse orbital angular momentum probed by a levitated optomechanical sensor**

  Yanhui Hu, Jack J. Kingsley-Smith, Maryam Nikkhou, James A. Sabin, Francisco J. Rodríguez-Fortuño, Xiaohao Xu, and James Millen

  arXiv:2209.09759 (2022)

Acknowledgements

Frist and foremost, I would like to thank my supervisor Dr. James Millen for all the mentoring and guidance he provided throughout the period of my PhD studies. I am very lucky and it is a great honour to be one of his first students and founding member of the fascinating Levitated Nanophysics Group at King's College London. I am grateful to him for always great advice to me and discussions about designing and performing experiments, understanding and thinking about physics and science, and how to present them. His open mind, endless passion on research, and always organizing and involvement in fantastic academic events, research networks and public engagements which I really enjoyed and have profited from a lot.

I also would like to thank my secondary supervisor Prof. Anatoly Zayats for his support and encouragement. I also benefit a lot from his different research topics in the field of optics and photonics, which expands my knowledge and research interest.

I would like to thank Dr. Benjamin Stickler for his leading expertise in the research field of quantum rotational optomechanics and his brilliant proposals which motivates my PhD research. I feel always inspired and encouraged every time talking to him, and had great lectures at Imperial and online.

Thank you Dr. Maryam Nikkhou and Dr. Muddassar Rashid for always giving me guidance and support using your expertise and rich experience in the research. It is really enjoyable to discuss physics, science and life with you, and solve problems in the lab.

Thank you Dr. Jack J. Kingsley-Smith, Dr. Francisco J. Rodríguez-Fortuño

and Dr. Xiaohao Xu for the great collaboration and your excellent work during the last stage of my PhD. Many thanks to the excellent work done by Julio Figueroa Quintana for the programming of numerical simulations.

Thank you Katie O'Flynn, James Sabin, and Yugang Ren for all the best time we spent together inside and outside the lab.

Thank you to all the colleagues and good friends in the department of physics at King's and from other departments, especially for creating the best working atmosphere here. Special thanks to the support and help from technical staff William Luckhurst, Alastair Symon and Ben Blackburn for successfully running experiments in the lab.

Thank you to all my friends who give me continued support and encouragement and make me enjoyable throughout the whole process outside the lab.

Last but not least, I would like to express my sincere gratitude to my family for their continuous love and support over the special period of time.

Abstract

Levitated optomechanics opens the door for many quantum experiments and sensing applications with the advantage of minimising the dissipation to the environment. It provides a unique research platform to control and cool the motion of micro/nano-size objects to the quantum regime, pushing the mass limit of exploring macroscopic quantum phenomena. Apart from the centre-of-mass motion of levitated nanoparticles, control and cooling of rotational degrees of freedom are of significant research interest, which explores another avenue for studying fundamental physics and developing quantum technologies.

This thesis focuses on ro-translational optomechanics with optically levitated nanoparticles in vacuum. A 1550 nm counter-propagation standing-wave optical trap experimental platform has been established for studying levitated optomechanics in high vacuum. Direct loading, optical trapping and corresponding detection techniques for high-efficiency measuring ro-translational degrees of freedom of levitated nanoparticles have been built. A clean, vacuum-compatible method based on laser-induced acoustic desorption (LIAD) is developed for directly loading nanoparticles into the optical trap, enabling us to load tailored silicon nanorods from the substrate with very high efficiency. The translational and rotational dynamics of levitated nanoparticles in vacuum have been systematically studied. Besides driving the levitated silicon nanorotor by circularly polarised light, it has been driven to full rotations at tens of MHz in several millibars in the transverse plane by transferring transverse orbit angular momentum, achieving five orders of magnitude higher applied torque compared to other reported nanorotors with the same optical power. Furthermore, the ro-translational motion of levitated

nanoparticles can be cooled by implementing feedback cooling schemes, such as parametric feedback for centre-of-mass and polarization feedback for librational motion. These paves way for next-step tests of rotational macroscopic quantum superposition experiments, such as orientational quantum revivals.

Contents

List of Figures

Chapter 1

Introduction

1.1 Levitated optomechanics

Testing the quantum nature of macroscopic objects is an outstanding challenge in modern physics [1, 2]. By controlling and cooling the mechanical motion of a macroscopic oscillator via light-matter interactions, optomechanics provides a prominent approach to exploring the boundary between the quantum and classical world [3, 4, 5, 6].

Compared to tethered oscillators, levitated mechanical oscillators take the advantage of ultra-low dissipation (a quality factor up to $Q \sim 10^{12}$ by theoretical prediction) due to being thermally isolated from the environment in ultra-high vacuum, leading to very low quantum decoherence and achievement of quantum ground state [7, 8, 9]. Moreover, the levitated nanoparticle can be released with free evolution for a macroscopic quantum state, which paves the way to study macroscopic quantum mechanics [10, 11, 12].

Optically levitating mechanical oscillators in high vacuum were proposed to observe macroscopic quantum behaviours by cavity cooling its centre-of-mass motion to the quantum ground state in around 2010 [13, 14, 15]. Such proposals have been first experimentally demonstrated [16, 17, 18, 19], which is a big step towards room-temperature quantum experiments with macroscopic mechanical systems. Remarkable progress has been made in recent years, the cavity cooling of a levitated silica nanoparticle via coherent scattering has been demonstrated to

the effective mode temperature of a few hundred millikelvin [20, 21], and achieved motional quantum ground state cooling of a 143 nm diameter nanosphere which comprises 10^8 atoms [22].

Without using a cavity, active feedback cooling of an optically levitated 4.7 μm silica particle to millikelvin by an additional three pairs of counter-propagating cooling beams has been demonstrated [23], and successfully measured the instantaneous velocity of a Brownian particle [24]. Meanwhile, a parametric feedback cooling method applied to cool a 70 nm radius silica nanosphere from room temperature to 50 mK has been presented [25], and this method has been further developed to phase-based linear feedback cool a nanoparticle to the centre-of-mass temperature of 450 μK (corresponding to the mean occupation number $\bar{n} \simeq 63$) in ultra-high vacuum (UHV), where the photon recoil heating from a macroscopic object was directly measured [26]. Another linear measurement-based feedback technique termed cold damping has been implemented to cool one translational mode of a levitated nanoparticle to microkelvin temperature [27] and observed motional sideband asymmetry which is a signature of the quantum ground state of motion [28]. Later on, optimizations on quantum-limited measurement, optimal control and detection efficiency enabled the active feedback technique to demonstrate quantum ground state cooling at room temperature [29] and cryogenic environments [30]. Based on the feedback cooling on centre-of-mass motions, levitated nanoparticles have been widely used for studying and investigating non-equilibrium fluctuation theorems [31], nonlinear dynamics and synchronization [32], collapse model of continuous spontaneous localization (CSL) [11] and thermodynamics theorem [33].

Levitated mechanical oscillators possess remarkably high mechanical quality factors and can be cooled to very low effective temperatures, as they are free from mechanical vibrations and thermal contact in UHV. These facilitate the excellent ability and potential in the aspect of technological applications, such as ultra-sensitive force, torque, acceleration and pressure sensing [34, 35, 36].

The limit of a detectable force $F_{\min}$ is based on the thermal energy of the oscillator:

$$F_{\min} = \sqrt{\frac{4\mathrm{k}_q k_{\mathrm{B}} T_{\mathrm{CM}} b}{\omega_q Q}}, \tag{1.1}$$

where k_q is the spring constant, k_{B} is the Boltzmann constant, T_{CM} is the temperature of the oscillator, ω_q is the resonance frequency, Q is the quality factor and b is the measurement bandwidth. From Equation (1.1), the higher quality factor and lower temperature of the oscillator indicate higher sensitivity.

In terms of applications, a yoctonewton force sensitivity experimental scheme by using a levitated nanoparticle in a cavity optomechanical system was proposed [37], and attonewton force measurement using a charged levitated microsphere [38] has been presented, which is expected to detect Casimir forces [39]. Larger levitated particles are also very sensitive to acceleration, achieving a sensitivity of 0.4×10^{-6} g/Hz for a 12 ng sphere [40]. In addition, levitated mechanical sensors have been used for searching dark matter [41, 42] and gravitational waves [43].

1.2 Rotational dynamics of levitated nanoparticles

Another distinguishing aspect of the levitated optomechanical system from other optomechanical systems is that levitated nanoparticles possess the ability to rotate, exhibiting abundant rotational dynamics in both classical and quantum manners [44, 45]. The controllability of rotational dynamics is of fundamental as well as practical importance, especially for quantum rotations since it determines a quantum system can be manipulated and brought to a desired target state to what extent [46].

Typically, the rotational dynamics of optically trapped nanoparticles can be manipulated through the angular momentum transfer between the light field and particles via light-matter interactions [47, 48, 49]. The properties of the light field play a crucial role in the way of transferring momentum, including but not limited to the form of linearly polarised light, circularly polarised light and struc-

tured light field [50, 51]. The specific characteristics of the nanoparticle and the way of its interactions with the light field also determine different ways of momentum transfer and hence influence its motion. If the levitated nanoparticle has anisotropic polarizability via their geometry [52, 53, 54, 55, 56] or if they are birefringent [57, 58, 59], they can manifest significant observable dynamics in rotational degrees of freedom $\{\alpha, \beta, \gamma\}$ in addition to translational modes $\{x, y, z\}$.

In this thesis, we mainly focus on the research of geometry-induced anisotropic polarizability with silicon nanorods. As shown in Figure 1.1, here we define the propagation direction of the trapping light as along the z-axis, and α is the angle between x-axis and the projection onto the x-y plane, β is the angle between the cylinder's symmetry axis and z-axis, and γ is the angle around the symmetry axis.

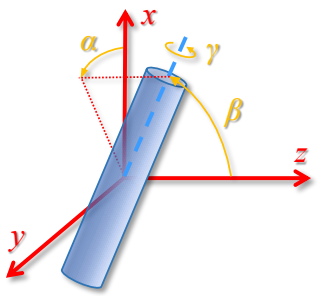

Figure 1.1: Definition of translational and rotational degrees of freedom of a cylinder. The propagation direction of the trapping light is along the z-axis. All degrees of freedom that can be observed and possible controlled: translational $\{x, y, z\}$ and rotational $\{\alpha, \beta, \gamma\}$.

Illuminated by the circularly polarised light, levitated nanoparticles in vacuum can be optically driven to full rotations up to several GHz [54, 55, 60, 61]. Such high rotation rate nanorotors are promising to detect the long-sought vacuum friction and weak forces or torque sensing with unprecedentedly high sensitivity [62, 56, 63], and even possibly tests of the fundamental mechanisms of dissipation in rotating systems [64, 65, 66].

In another scenario, within a linearly polarised light, the anisotropic nanoparticle would align one of its axes to the polarisation direction of the trapping light where it has minimum potential energy. When the particle strays away from the equilibrium angle, a restoring torque pushes it back to its original orientation. This

manifests a librational motion of the levitated nanoparticle [52, 53], which expands new degrees of freedom $\{\alpha, \beta, \gamma\}$ for studying quantum effects in addition to the centre-of-mass motion $\{x, y, z\}$. Similar to translation, librational motion can be described as a harmonic oscillator, namely "librator", which is reasonably promising to reach a quantum ground state and is therefore a stark contender in the race towards the quantum regime. In the quantum regime, the non-harmonicity of the rotational spectrum of the rigid object can give rise to pronounced interference effects which have no analogy in free centre-of-mass motion [8, 44], which will be discussed in the next section.

The motion must be cooled first for the preparation of quantum experiments, since the "hot" particle which occupies a broad distribution of states will average over all these states during the subsequent evolution, leading to wash-out quantum signatures such as the interference pattern which is the evidence of quantum superposition [12, 67].

In previous research, cooling the rotational state into the quantum ground state has been successfully implemented for small-size molecules [68, 69, 70]. The theoretical research works on cooling nanometre and micrometre-size particles have also been proposed, assessing and predicting that efficient cavity cooling and feedback cooling the ro-translational motion into the quantum regime is achievable [71, 72, 73, 74]. By coupling rotational and translational degrees of freedom, a micrometre-size vaterite crystal was observed to be effectively cooled to 40 K without any active cooling method [57]. Rotational cooling via coupling the librations of nanoscale nitrogen-vacancy(NV) colour centre diamond to its internal quantum system has been proposed and implemented to a few kelvins [75]. Active feedback cooling on the librational motion of levitated silica nanodumbells has been introduced and achieved sub-kelvin cooling [76], and extended to more degrees of freedom [77, 78]. Compared to nanospheres and nanodumbells, nanocylinders with higher geometric aspect ratio and thus larger moment of inertia would be exploited for exploring rotational quantum phenomena, and might be useful for quantum information [79, 80].

1.3 Rotational macroscopic quantum experiments

The superposition principle is the core feature that distinguishes quantum mechanics from classical mechanics [2, 10]. One of the most established schemes to observe macroscopic superpositions is the matter-wave interferometry via diffraction using optical gratings [81, 82]. The recent highlights include the first demonstration of Bragg diffraction of organic molecules through laser beams [83] and the record-breaking near-field Talbot-Lau interference with 2.5×10^4 amu molecules [84]. In macroscopic quantum observations, different quantum interference protocols using even larger mass objects (e.g., micro/nano-scale particles) have also been proposed and demonstrated [11, 85, 86, 87]. These are all based on the superposition of different centre-of-mass positions before the coherent interactions with the grating.

Intriguingly, cooling the librational motion of the levitated macroscopic oscillator to the quantum regime provides a new approach to testing macroscopic quantum superpositions [44]. B. Stickler *et al.* proposed a radically new, exper-

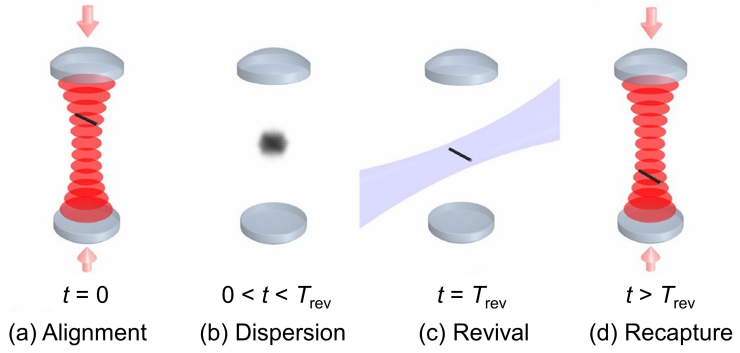

Figure 1.2: The four-step scheme to observe orientational quantum revivals of a levitated nanorotor. (a) The nanorotor is levitated and aligned with a linearly polarised light (red beam), and its librations are cooled to sub-kelvin temperatures. (b) The orientation states of the nanorotor quickly and freely disperse after switching off the trapping laser. (c) At integer multiples of the quantum revival time, a probe light pulse (blue beam) is used to measure the rotor orientation by light scattering. (d) The nanorotor is recaptured by the trapping laser after a short distance of free fall and prepared for recycling to experimental repetitions. Reproduced from [88].

imentally viable orientational quantum interference scheme via a single levitated nanoparticle with librational motion cooling, enabling the first test of macroscopic angular momentum quantization with massive objects [88]. Figure 1.2 illustrates the proposed scheme consisting of four steps: (a) alignment, (b) dispersion, (c) revival and (d) recapture. The basic principle is that an initially tightly oriented quantum rotor rapidly disperses, and the collective interference of all occupied angular momentum states leads to a complete re-appearance of the initial state after multiples of a longer quantum revival time [89, 90]. The width and height of the orientational quantum revival are determined by the initial librational temperature of the nanorotor, however, the revival time only depends on the moment of inertia I by $T_{\mathrm{rev}} = 2\pi\hbar/I$.

Figure 1.3 shows the time evolution of the orientational alignment of levitated carbon nanotubes with the mass $M = 1.9 \times 10^5$ amu and the length $l = 50$ nm at $T = 100$ μK. For the initial temperature of $T = 1$ K, it is possible to observe the rotational quantum revival phenomenon during the free fall with the revival time $T_{\mathrm{rev}} \simeq 3.8$ ms for carbon nanotubes and $T_{\mathrm{rev}} \simeq 28$ ms for silicon nanorods.

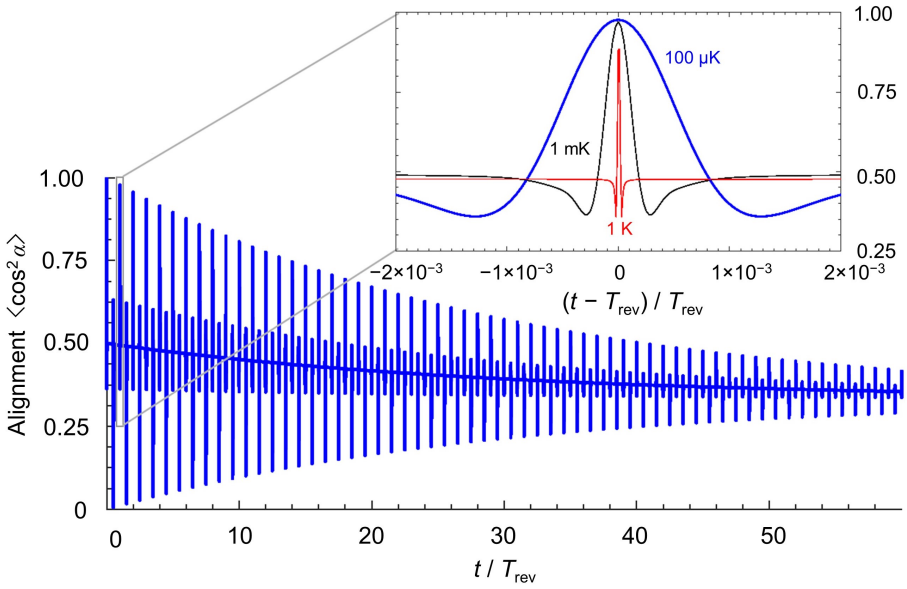

Figure 1.3: The time evolution of orientational alignment signal of levitated carbon nanotubes ($M = 1.9 \times 10^5$ amu and $l = 50$ nm) at 100 μK in the unit of the revival time T_{rev}. The inset shows the quantum revival for 3 different initial temperatures of 1 K, 1 mK and 100 μK. Reproduced from [88].

This strategy requires no beamsplitters, which removes a major technological hurdle and decoherence source [8]. Meanwhile, it demands moderate motional temperature (i.e., the initial temperature of rotational motion below 1 K by cavity or feedback cooling) with feasible experimental implementation conditions at room temperature, which provides an exciting alternative to test the quantum superposition principle.

1.4 Thesis outline

In this thesis, we aim to develop a new experimental setup that would allow us to achieve full control and cooling of the ro-translational motion of levitated nanoparticles in vacuum, as this is a necessary prerequisite to achieving quantum control of motional states in all degrees of freedom and further research on macroscopic quantum experiments.

This doctoral thesis is divided into three parts: (i) Optical trapping and levitation in Chapters 2 and 3; (ii) Control of full rotations in Chapter 4; (iii) Ro-translational optomechanical cooling in Chapter 5.

To be specific, Chapter 2 provides the theoretical framework and the experimental details of our optical levitation platform.

In Chapter 3, we develop and demonstrate a clean and vacuum-compatible method for direct loading nanoparticles with high efficiency in the optical trap under vacuum conditions.

Chapter 4 presents the control of full rotations of levitated nanomechanical rotors by transferring spin angular momentum via circularly polarised light and orbit angular momentum via structured transverse optical vortices.

Chapter 5 focuses on the implementation of parametric feedback cooling on centre-of-mass motion of levitated nanoparticles, and proposes a new polarisation feedback scheme for simultaneous cooling librational motion of levitated nanorods.

This thesis is concluded in Chapter 6 where the main results are summarised and present an outlook about the coming exciting quantum optomechanics experiments based on the same setup and further sensing applications.

Chapter 2

Fundamentals of Levitated Optomechanics

2.1 Introduction

Back in the 1970s, Nobel laureate A. Ashkin invented optical tweezers which can trap and manipulate micrometre-size particles by the radiation pressure of light in air [91, 92]. Later on, the research of optical tweezers mainly focused on trapping in liquid or air for various applications of biophysics and materials research [48, 93]. In recent years, the levitated optomechanical system operating in vacuum is rapidly developed due to its unique properties differentiating the platform from conventional mechanical oscillators for exploring macroscopic quantum behaviour.

In this chapter, the experimental system for studying rotational optomechanics with levitated nanoparticles in vacuum is presented. The underlying physical understanding of the interface between light and levitated mechanical oscillators is the foundation of the experiments discussed in this thesis. Section 2.2 provides a basic theoretical description of mechanical oscillators, optical fields, and their optomechanical interactions. Section 2.3 models the stochastic dynamics of levitated nanoparticles including nanospheres with homogeneous spherical symmetry and nanocylinders with anisotropic geometry. The last Section 2.4 presents the details of each component and the performance of the experimental apparatus constructed for this thesis.

2.2 Optomechanical interactions

2.2.1 Mechanical oscillator

The harmonic oscillator is a prominent and basic model in both classical and quantum mechanical systems, which is widely found in almost any kind of physical system in nature. A mechanical oscillator has an oscillation of some parameter around a central value. Classically, the motion of a mechanical oscillator is given by:

$$x(t) = A\sin(\omega_m t + \varphi), \tag{2.1}$$

where A is oscillation amplitude which is determined by the initial conditions and $\omega_m = 2\pi f_m$ is its eigenfrequency. The phase φ denotes the relative position of the oscillator to the point of origin at $t = 0$ and is also determined by the initial conditions.

The eigenfrequency ω_m of the mechanical system is given by:

$$\omega_m = \sqrt{\frac{\mathrm{k}}{M}}, \tag{2.2}$$

where M is the mass of the harmonic oscillator and it is driven by a linear restoring force F:

$$F = -\mathrm{k}x, \tag{2.3}$$

where k is a positive constant, usually referred to as the spring constant.

For a perfect harmonic oscillator without any damping, the total energy E_{tot} of the system is conserved:

$$E_{\mathrm{tot}} = E_{\mathrm{k}} + E_{\mathrm{p}} = \frac{M}{2}\omega_m^2 A^2, \tag{2.4}$$

with its kinetic E_{k} and potential E_{p} components varying over time:

$$\begin{aligned} E_{\mathrm{k}}(t) &= \frac{M}{2}\dot{x}^2 = \frac{\mathrm{k}}{2}A^2\cos^2(\omega_m t + \varphi), \\ E_{\mathrm{p}}(t) &= \frac{\mathrm{k}}{2}x^2 \ = \frac{\mathrm{k}}{2}A^2\sin^2(\omega_m t + \varphi). \end{aligned} \tag{2.5}$$

However, any real mechanical oscillator experiences friction as it interacts with its environment, which leads to an unavoidable damping term in the system. This alters the motion and energy of the mechanical oscillator, which will be discussed in later sections.

If we replace the classical variables with their corresponding quantum mechanical Hamiltonian operators, we can obtain the quantum form of a harmonic oscillator in phase space:

$$\hat{H} = \frac{\hat{p}^2}{2M} + \frac{1}{2}M\omega_m^2\hat{x}^2, \tag{2.6}$$

where $\hat{x}$ is the position operator, $\hat{p}$ is the momentum operator. They fulfill the commutation relation $[\hat{x}, \hat{p}] = i\hbar$, where $\hbar$ is the reduced Plank constant.

In the occupation number representation, the operator $\hat{x}$ and $\hat{p}$ can be rewritten in the form of the creation operator $\hat{a}^\dagger$ and the annihilation operator $\hat{a}$ [94]:

$$\begin{aligned} \hat{a} &= \frac{1}{\sqrt{2}}(\hat{X} + i\hat{P}), \\ \hat{a}^\dagger &= \frac{1}{\sqrt{2}}(\hat{X} - i\hat{P}), \end{aligned} \tag{2.7}$$

where $\hat{X}$ and $\hat{P}$ are the dimensionless position and momentum operators of the oscillator with the definition of $\hat{x} = \sqrt{\hbar/(M\omega_m)}\,\hat{X}$ and $\hat{p} = \sqrt{\hbar M\omega_m}\,\hat{P}$. The creation operator $\hat{a}^\dagger$ and the annihilation operator $\hat{a}$ still obey the commutation relation $\left[\hat{a}^\dagger, \hat{a}\right] = 1$.

Therefore, the Hamiltonian in Equation (2.6) can be expressed as:

$$\hat{H} = \hbar\omega_m\left(\hat{a}^\dagger\hat{a} + \frac{1}{2}\right). \tag{2.8}$$

By solving the Schrödinger equation, the corresponding eigenstates can be represented by the Number states (or Fock states) $\{|n\rangle,\, n = 0, 1, 2, \cdots\}$ and are eigenstates of the number operator $\hat{n} = \hat{a}^\dagger\hat{a}$ [95]:

$$\hat{a}^\dagger\hat{a}|n\rangle = \hat{n}|n\rangle = n|n\rangle, \quad |n\rangle = \sqrt{\frac{1}{n!}}\left(\hat{a}^\dagger\right)^n|0\rangle, \tag{2.9}$$

corresponding to the n^{th} discrete energy levels:

$$E_n = \hbar\omega_m \left(n + \frac{1}{2}\right). \tag{2.10}$$

The lowest energy state $|0\rangle$, which is also called the ground state for a quantum mechanical oscillator, is represented in the coordinate representation as:

$$\langle \hat{x}|0\rangle = \left(\frac{M\omega_m}{2\hbar}\right)^{\frac{1}{4}} \exp\left(-\frac{M\omega_m}{2\hbar}\hat{x}^2\right), \tag{2.11}$$

with the associated minimum non-zero energy "zero-point energy" compatible with the Heisenberg uncertainty principle:

$$E_0 = \frac{1}{2}\hbar\omega_m. \tag{2.12}$$

We can also calculate the expectation value for the position operator $\hat{x}$ and the position operator squared $\hat{x}^2$ as:

$$\begin{aligned} \langle \hat{x}\rangle_n &= \langle n|\hat{x}|n\rangle = 0, \\ \langle \hat{x}^2\rangle_n &= \langle n|\hat{x}^2|n\rangle = \frac{\hbar}{M\omega_m}\left(n + \frac{1}{2}\right). \end{aligned} \tag{2.13}$$

From Equation (2.13), the mechanical zero-point fluctuation associated with zero-point energy is given by:

$$x_{\text{zpf}} = \sqrt{\langle \hat{x}^2\rangle_0 - \langle \hat{x}\rangle_0^2} = \sqrt{\frac{\hbar}{2M\omega_m}}. \tag{2.14}$$

When a harmonic oscillator is in thermal equilibrium with temperature T, its average occupation number in the Bose-Einstein distribution can be written as:

$$\bar{n} = \langle \hat{n}\rangle = \text{Tr}(e^{-\hat{H}/k_{\text{B}}T}\,\hat{n}) = \frac{1}{e^{(\hbar\omega_m)/(k_{\text{B}}T)} - 1}, \tag{2.15}$$

where k_{B} is the Boltzmann constant.

In the large temperature limit (i.e., $k_{\text{B}}T \gg \hbar\omega_m$), the average thermal occu-

pation $\bar{n}$ of the mechanical oscillator becomes:

$$\bar{n} \approx \frac{k_B T}{\hbar \omega_m}. \tag{2.16}$$

However, this approximation does not hold for near the ground state (i.e., $\bar{n} = \mathcal{O}(1)$), which has to use the full Bose-Einstein statistics.

For a levitated mechanical oscillator with the mass of $\sim 10^{-18}$ kg and the oscillation frequency of $\sim$ 500 kHz, its zero-point fluctuation is about 10 pm. According to Heisenberg's uncertainty principle, this is the minimum uncertainty in the position measurement given by the zero-point motion. In order to resolve the quantum ground state which normally requires $\bar{n} < 1$, the effective centre-of-mass temperature of the mechanical oscillator needs to be cooled down below $T_{\text{eff}} \sim 25\,\mu$K.

2.2.2 Gaussian beam

In most cases of levitated optomechanics, the optical field provided by a focused laser can be simply described by the fundamental Gaussian mode TEM_{00}. A Gaussian beam with the wavelength of λ has its electric field intensities with Gaussian function:

$$E(\mathbf{r}, z) = E_0 \frac{\mathrm{w}_0}{\mathrm{w}(z)} \exp\left(-\frac{\mathbf{r}^2}{\mathrm{w}(z)^2} - ikz - ik\frac{\mathbf{r}^2}{2R(z)} + i\varphi_{\mathrm{G}}(z)\right), \tag{2.17}$$

where $\mathbf{r}$ is the radial vector from the centre of the optical axis of the beam, E_0 is the electric field amplitude at the origin point, w_0 is the beam waist, $k = 2\pi/\lambda$ is the wavenumber and $\varphi_{\mathrm{G}}(z)$ is the Gouy phase.

The beam width $\mathrm{w}(z)$ with respect to the axial distance z from the beam waist is defined as:

$$\mathrm{w}(z) = \mathrm{w}_0 \sqrt{1 + \left(\frac{z}{z_R}\right)^2}, \tag{2.18}$$

where z_R is the Rayleigh range:

$$z_R \approx \frac{\pi w_0^2}{\lambda}. \tag{2.19}$$

The radius of curvature $R(z)$ is defined as:

$$R(z) = z\left(1 + \left(\frac{z_R}{z}\right)^2\right). \tag{2.20}$$

The intensity distribution of the Gaussian beam can be written as:

$$I(x,y) = I_0 e^{-\frac{2(x^2+y^2)}{\mathrm{w}(z)^2}} = \frac{2P_{\mathrm{opt}}}{\pi \mathrm{w}(z)^2} e^{-\frac{2(x^2+y^2)}{\mathrm{w}(z)^2}}, \tag{2.21}$$

where P_{opt} is the total power of the laser beam.

The Gaussian beam is focused by a lens with a given numerical aperture (NA). By using the paraxial approximation of geometric optics with small-angle limit, the beam waist of the focused Gaussian beam becomes:

$$\mathrm{w}_0 \approx \frac{\lambda}{\pi \mathrm{NA}}, \tag{2.22}$$

and the Rayleigh range as:

$$z_R = \frac{\lambda}{\pi \mathrm{NA}^2}, \tag{2.23}$$

which is the region around the focus where the electric field wavefronts are mostly planar for a relatively small NA.

2.2.3 Optical forces

Via the exchange of momentum of light, the nanomechanical oscillator can be trapped, levitated, and controlled by optical forces. According to the classical mechanics of Newton's law, force is a derivative of momentum with respect to time. Each photon carries energy $E_{\mathrm{p}} = h\nu$ (with the frequency of ν) and momentum $p_{\mathrm{p}} = E_{\mathrm{p}}/c = \hbar k_0$, where c is the speed of light and $k_0 = 2\pi\nu/c$ is the vacuum wave vector. The momentum of photons normally can be transferred to objects in three different ways: photon absorption, photon reflection, and photon deflection. A dielectric particle can acquire and exchange momentum from a light field by absorbing and scattering the incident photons.

Optical forces are based on the rate of the exchange of momentum between light and matter, and their calculations are based on the change in the total momentum of light before their interaction and after. Depending on the ratio between the wavelength of light and the size of particles, the calculation of the optical forces either given by the full solution of Maxwell's equations or certain simplified assumptions can be made analytically and numerically.

In our case of dielectric nanoparticles levitated in vacuum, the interaction between the optical field and levitated nanoparticles can be described by the dipole approximation model in the Rayleigh regime when the particle radius r is much smaller than the wavelength λ ($r \ll \lambda$) [96, 47]. The dipole moment induced by an applied electric field $\mathbf{E}(\mathbf{r})$ can be written as [97]:

$$\mathbf{p}(\mathbf{r}) = \alpha_0 \mathbf{E}(\mathbf{r}), \tag{2.24}$$

where $\mathbf{r}$ is the position of the particle, α_0 is the dipolar polarizability determining the strength of interaction with the light field, which depends on the material property and geometry of the nanoparticles.

The time-averaged force acting on the dipole is:

$$\langle \mathbf{F}(\mathbf{r}) \rangle = \frac{1}{2} \Re \left(\alpha_0 \mathbf{E}(\mathbf{r}) \nabla \mathbf{E}^*(\mathbf{r}) \right), \tag{2.25}$$

The optical force can be divided into two parts, the gradient force and the scattering force:

$$\langle \mathbf{F}(\mathbf{r}) \rangle = \langle \mathbf{F}_{\text{grad}}(\mathbf{r}) \rangle + \langle \mathbf{F}_{\text{scat}}(\mathbf{r}) \rangle. \tag{2.26}$$

The first term is the gradient force, representing the force pointing towards the highest intensity region due to the gradient of the electric field intensity, which allows three-dimensional confinement in the beam focus. The direction of the scattering force is along the beam propagation axis and therefore pushes the particle away from the trap centre.

When the dipole is placed in the non-uniform light field, the conservative

gradient force can be calculated with the real part of dipolar polarizability $\Re(\alpha)$:

$$\langle \mathbf{F}_{\mathrm{grad}}(\mathbf{r}) \rangle = \frac{\Re(\alpha_0) \nabla \langle |\mathbf{E}(\mathbf{r})|^2 \rangle}{4}, \tag{2.27}$$

and the non-conservative scattering force is:

$$\langle \mathbf{F}_{\mathrm{scat}}(\mathbf{r}) \rangle = \sigma_{\mathrm{tot}} \left(\frac{\mathbf{S}(\mathbf{r})}{c} + c \nabla \times \mathbf{L} \right), \tag{2.28}$$

where the total cross-section σ_{tot} is the sum of absorption and scattering cross-sections, and the time-averaged Poynting vector is $\mathbf{S} = \langle \mathbf{E} \times \mathbf{H}^* \rangle$ with magnetic field $\mathbf{H}$. The scattering force has two contributions: one from the radiation pressure which is proportional to the Poynting vector; the other is a curl force associated with the distribution of the time-averaged spin density of the light field:

$$\mathbf{L} = -\frac{i\epsilon_0}{8\pi\nu} \langle \mathbf{E} \times \mathbf{E}^* \rangle. \tag{2.29}$$

This curl force must be considered as a significant contribution for a tightly focused beam, while it becomes zero for a plane wave.

In a stable optical trap, the gradient force must be much larger than the scattering force. Due to the scattering force mainly resulting from the absorption (proportional to the imaginary part of polarizability $\Im(\alpha_0)$) and $\Re(\alpha_0)/\Im(\alpha_0) \propto r^3$, it is negligible for small and transparent particles in the following discussions. Moreover, in the standing wave trap formed by a pair of counter-propagation beams, the scattering force can mostly be cancelled, since the direction of the scattering force exerted on particles in each arm is opposite [48]. Therefore, the gradient force dominates the dynamics of the levitated particle. However, the scattering force is not eliminated even if the experimental set-up is perfect (i.e., the laser beams are perfectly aligned) because the momentum transfer from photon scattering in turn modifies the optical field [96].

2.2.4 Optical potential

When we trap a dielectric nanosphere with the radius of r $\ll \lambda$ in a Gaussian beam, the dynamics of the levitated particle are approximately analysed as a harmonic oscillator confined in a harmonic potential with the Rayleigh approximation. The harmonic optical potential U_{opt} can be obtained by integrating the conservative force $\mathbf{F}_{\text{opt}}$ (here we consider it is provided by the gradient force):

$$U_{\text{opt}} = \int \mathbf{F}_{\text{opt}} \mathrm{d}V, \tag{2.30}$$

and the optical force can be well-approximated in the way of a linear restoring force:

$$\mathbf{F}_{\text{opt}} = -\mathrm{k}_q q, \tag{2.31}$$

where k_q is the spring constant (or trap stiffness) for the degrees of freedom of q.

The trapping angular frequency is characterised as:

$$\omega_q = \sqrt{\frac{\mathrm{k}_q}{M}}. \tag{2.32}$$

Harmonic potential for levitated nanospheres

The polarizability of silica nanospheres, from the Clausius-Mossotti relation, can be described as [7]:

$$\alpha = 4\pi\epsilon_0 r^3 \frac{(\epsilon_r - 1)}{(\epsilon_r + 2)}, \tag{2.33}$$

where ϵ_0 is the vacuum permittivity, and ϵ_r is the relative permittivity which is dependent on the trapping light frequency.

By neglecting the scattering force on the small nanosphere and considering small oscillations around the potential minimum, the potential well can be approximated to be harmonic and the centre-of-mass motion is independent in three translational degrees of freedom $\{x, y, z\}$. The optical potential is given by [7]:

$$U_{\text{opt,sphere}} = -\frac{\Re(\alpha_0) E_0^2}{4}, \tag{2.34}$$

where E_0 is related to the optical power P_{opt} of Gaussian beam:

$$P_{\text{opt}} = \frac{c\epsilon_0 \pi \mathrm{w}_x \mathrm{w}_y E_0^2}{4}, \tag{2.35}$$

where w_x and w_y are the beam waist along x and y direction respectively. It follows $\mathrm{w}_0^2 = \mathrm{w}_x \mathrm{w}_y$, where w_0 is the beam waist shown in Equation (2.21).

Thus, the trap stiffness can be written as:

$$\mathrm{k}_q = \frac{4\Im(\alpha_0) P_{\text{opt}}(t)}{\pi c \epsilon_0 \mathrm{w}_0^2 \mathrm{w}_q^2}, \tag{2.36}$$

where w_q denotes the beam waist along the q-direction. The time-dependent optical power shows the possibility of controlling the dynamics through this variable and this ability to dynamically vary the spring constant is a crucial advantage of optically levitated oscillators.

Further, we can derive the angular oscillation frequencies $\omega_{x,y}$ and ω_z of the levitated nanosphere as:

$$\begin{aligned} \omega_{x,y} &= \sqrt{\frac{4\Re(\alpha_0) P_{\text{opt}}}{M \pi c \epsilon_0 \mathrm{w}_0^4}}, \\ \omega_z &= \sqrt{\frac{8\Re(\alpha_0) P_{\text{opt}}}{M \pi c \epsilon_0 \mathrm{w}_0^2 z_R^2}}, \end{aligned} \tag{2.37}$$

where w_z is given by the Rayleigh range in Equation (2.23) with $z_R = \mathrm{w}_z/\sqrt{2} \approx \pi \mathrm{w}_0^2/\lambda$.

Optical potential for anisotropic nanoparticles

In terms of anisotropic particles such as nanocylinders, the polarizability α_0 is a tensor due to its anisotropic geometry [98], and the orientation with respect to the optical field polarisation axis leads to different interaction strengths [71]. This introduces the ro-translational dynamics of the levitated nanocylinder. The translational motion depends on mass M, while the rotational motion depends on the moment of inertial I. Moreover, an anisotropic particle exhibits different dynamics with different polarisation states of the light field. In the case of lin-

early polarised light, the nanocylinder tends to align with the polarisation axis of the light; while for circularly polarised light, the levitated nanocylinder starts to rotate, which demonstrates more degrees of freedom compared to the basis of the centre-of-mass motion. We use levitated silicon nanorods as an excellent tool for exploring and controlling all the rotational and translational motions [53, 62].

The polarizability of a levitated nanorod can be described by the form of susceptibility tensor $\chi_0 = \mathrm{diag}(\chi_\perp, \chi_\perp, \chi_\parallel)$ with a component $\chi_\perp$ perpendicular and a component $\chi_\parallel$ parallel to the symmetry axis:

$$\begin{aligned} \chi_\parallel &= \epsilon_r - 1, \\ \chi_\perp &= \frac{2(\epsilon_r - 1)}{\epsilon_r + 1}. \end{aligned} \tag{2.38}$$

When the long axis of the nanorod is aligned along the axis of polarisation, its polarizability achieves a maximal value $\chi_{||}$, when its long axis is orthogonal to the axis of the polarisation, the polarizability decreases to the minimal value $\chi_\perp$. Compared to a sphere of the equivalent volume, the maximal polarizability of a cylinder is $(\epsilon_r + 2)/3$ times larger. This factor is 2 for silica, whereas it is a factor of 4.6 for silicon [99].

We introduce the rotation matrix $R(\Omega)$ to translate between the body-fixed (coordinates with origin at the centre-of-mass of the particle) and the space-fixed (coordinates with origin at the focus of the trap) coordinates $\hat{\mathbf{n}}_j = R(\Omega)\hat{\mathbf{e}}_i$ with $j \in \{a, b, c\}$, where $\hat{\mathbf{n}}_j$ denoted three orthonormal basis vectors which are aligned with the main three axes of the cylinder, and $\hat{\mathbf{e}}_i$ denotes the common orthonormal basis with $i \in \{x, y, z\}$.

The rotation matrix $R(\Omega)$ characterizes the orientation Ω for the particle by the Euler angles $\alpha \in (0, 2\pi]$, $\beta \in (0, \pi]$ and $\gamma \in (0, 2\pi]$, and is defined by rotations around the z-y'-z'' convention [100]. The α angle is with respect to the x-axis and the project of the particle in the x-y plane, the β is the angle between the rod's symmetry axis and the beam propagation axis z-axis, and the γ quantifies the angle around the symmetry axis. The orientation-dependent susceptibility tensor

is described by the usual rules of matrix transformation:

$$\chi(\Omega) = R(\Omega)\chi_0 R(\Omega)^{\mathrm{T}}. \tag{2.39}$$

The general form of the optical potential centred of the focus is [73]:

$$U(\Omega) = -\frac{\epsilon_0 V}{4}\mathbf{E}_0^* \cdot \chi(\Omega)\mathbf{E}_0, \tag{2.40}$$

where E_0 is the electric field acting on the dielectric particle and V is the volume of the particle.

We define linearly polarised light as $\mathbf{E} = E_0\mathbf{e} = E_0(e_x\hat{\mathbf{e}}_x + e_y\hat{\mathbf{e}}_y)$, where E_0 is the amplitude of the electric field and e_x, e_y are the components in the x and y space-fixed coordinates respectively satisfying $e_x^2 + e_y^2 = 1$. The optical potential for a nanorod as a function of its radial displacement $\mathbf{r}$ and Euler angles can be expressed as:

$$U_{\text{opt, rod}}(\mathbf{r}, \Omega) = -\frac{\epsilon_0 V_{\text{rod}}\chi_{\parallel}E_0^2}{4} f(\mathbf{r}) \left[\frac{\chi_{\perp}}{\chi_{\parallel}} + \frac{\Delta\chi}{\chi_{\parallel}}(\mathbf{m}\cdot\mathbf{e})^2\right], \tag{2.41}$$

where V_{rod} is the volume of the nanorod, $\Delta\chi = \chi_{\parallel} - \chi_{\perp}$ is the susceptibility anisotropy, and the symmetry axis of the rod is aligned along the vector $\mathbf{m}$. $f(\mathbf{r}) = \cos^2(kz)$ represents a standing wave trap along the beam propagation z-direction. The dot product term $\mathbf{m}\cdot\mathbf{e}$ characterises the orientation of the nanorod $\mathbf{m}$ with respect to the polarisation direction of the tapping beam $\mathbf{e}$ in terms of Euler angles $\{\alpha, \beta, \gamma\}$ with $\mathbf{m}\cdot\mathbf{e} = \sin\beta(e_x\cos\alpha + e_y\sin\alpha)$.

From this equation, it is straightforward to show that the minimum potential for a linearly polarised light along x-direction can be achieved when $\alpha = 0$ and $\beta = \pi/2$, which means the trapped nanorod tends to align with the polarisation of the optical field. For a linearly trapped nanorod, we can consider the angular momentum with a small deflection from the polarisation axis as harmonic.

For a harmonically trapped nanorod, the translational frequency is $\omega_q = \sqrt{\mathrm{k}_q/M}$ with the translational spring constant k_q, whereas the librational fre-

quency is $\omega_\theta = \sqrt{\mathrm{k}_\theta / I}$ with the librational spring constant k_θ and the moment of inertia I. Since the mass $M \propto r^3$ and the moment of inertial $I \propto r^5$, the frequencies of the librational modes are normally higher than translational modes for nanoparticles. The Rayleigh-Gans approximation can be used for numerically analysing the optical forces on a non-spherical particle in the polarisation-dependent field [101]. It is worth noticing that this approximation is suitable for the case that no length scale exceeds the wavelength of the light and at least one dimension is much smaller than the wavelength of the light [102].

The trapping frequencies (three translational $\{x, y, z\}$ and two librational $\{\alpha, \beta\}$) of a levitated nanorod in a harmonical potential are given by [71]:

$$\begin{aligned} f_{x,y} &= \frac{1}{2\pi}\sqrt{\frac{8P_{\mathrm{opt}}\chi_\parallel}{\pi\rho c \mathrm{w}_0^4}}, \\ f_z &= \frac{1}{2\pi}\sqrt{\frac{4k^2 P_{\mathrm{opt}}\chi_\parallel}{\pi\rho c \mathrm{w}_0^2}}, \\ f_\alpha &= \frac{1}{2\pi}\sqrt{\frac{48P_{\mathrm{opt}}\Delta\chi}{\pi\rho c \mathrm{w}_0^2 l^2}}, \\ f_\beta &= \frac{1}{2\pi}\sqrt{\frac{48P_{\mathrm{opt}}\chi_\parallel}{\pi\rho c \mathrm{w}_0^2 l^2}\left(\frac{\Delta\chi}{\chi_\parallel} + \frac{(kl)^2}{12}\right)}, \end{aligned} \tag{2.42}$$

where $\rho = 2330$ kg m^{-3} is the density of silicon, and l is the length of the nanorod.

When the trapping light is circularly polarised, the trapping potential in rotational degrees of freedom (i.e., α on the x-y plane) vanishes while the force in the translational degrees of freedom remains, so that the optical potential confines the nanorod to rotate in the polarisation plane under a radiation torque. These physical characteristics of nanorotors provide fertile ground for exploring the rotational quantum behaviours and ultra-sensitive sensing applications such as torque and pressure measurements, which will be discussed in Chapter 4 in detail.

2.3 Dynamics of levitated nanoparticles

2.3.1 Stochastic differential equation

In a more practical scenario, the nanoparticle is not levitated in a perfect vacuum with completely adiabatic conditions but coupled to a thermal bath at a tempera-

ture T_b with dissipation rate Γ_CM. It has interactions with the environment from mechanical (collisions with gas molecules) and radiative (blackbody and scattering) contributions, which leads to dissipation acting on its ro-translational motions and is the source of the random forces acting on the nanoparticle.

The decoupled centre-of-mass motion can be described by a Langevin equation in three translational degrees of freedom ($q \in \{x, y, z\}$) based on the Fluctuation-Dissipation Theorem:

$$\ddot{q}(t) + \Gamma_\mathrm{CM}\dot{q}(t) + \omega_q^2 q(t) = \frac{1}{M}F_\mathrm{fluct}(t). \tag{2.43}$$

In most practical purposes, the fluctuation force F_fluct can be considered as frequency-independent white noise which satisfies:

$$\langle F_\mathrm{fluct}(t)F_\mathrm{fluct}(t')\rangle = 2M\Gamma_\mathrm{CM}k_\mathrm{B}T_\mathrm{b}\delta(t-t'), \tag{2.44}$$

where T_b is the temperature of the bath or environment, ω_q is the natural mechanical oscillation frequency of the levitated particle in the q-direction and Γ_CM is the total momentum damping rate on the particle. When $\omega_q \ll \Gamma_\mathrm{CM}$, it means the motion is overdamped; critically damped at $\omega_q \approx \Gamma_\mathrm{CM}$; and $\omega_q \gg \Gamma_\mathrm{CM}$ in underdamped regime. In our scenarios, the levitated nanoparticles are normally in the underdamped regime.

Figure 2.1 shows the simulations of three translational motions of a 300 nm diameter silica nanosphere levitated in a standing-wave trap along z-axis with the total trapping power of 300 mW. The ambient environment is at the pressure of $P_\mathrm{gas} = 0.1$ mbar (corresponding to a gas damping rate $\simeq 150$ Hz) at room temperature $T_b = 298$ K. Since the trap stiffness of k_z is $\mathrm{k}_z/\mathrm{k}_{x,y} = (k^2\mathrm{w}_0^2)/2$ tighter than that of $\mathrm{k}_{x,y}$ from Equation (2.36), we can notice that the oscillation amplitude in z-direction is about 51 times smaller than x, y-direction, and the oscillation frequency ω_z is about 7 times larger than the other two which is also shown in Figure 2.2.

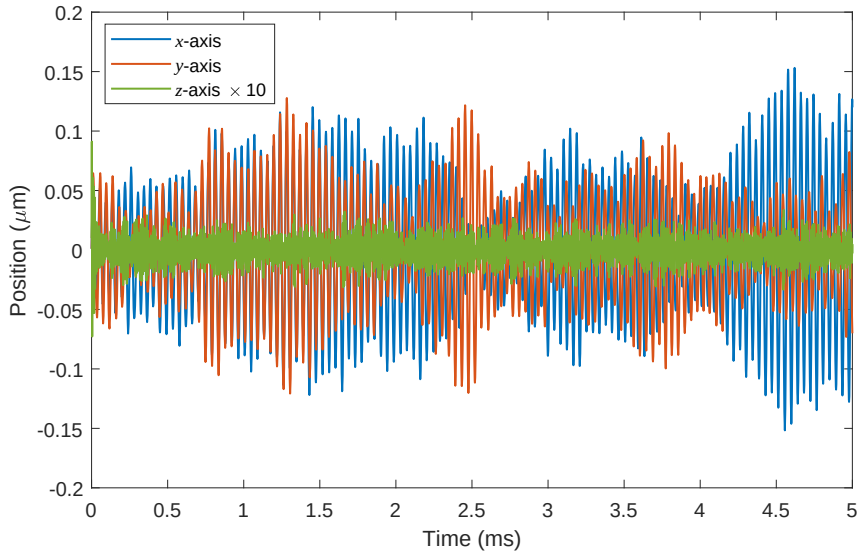

Figure 2.1: Simulation of translational dynamics of a levitated silica nanosphere in the underdamped regime at a thermal bath of $T_b = 298$ K. The beam waist is 2.5 μm. The pressure is set to 0.1 mbar, corresponding to a gas damping rate of $\simeq 150$ Hz. The fluctuation term is set as white noise with a timestep of 10^{-7} s. The blue and orange lines show the dynamics in the x and y directions. The green line represents the dynamics in the z direction and is amplified by 10 times.

The autocorrelation function of the stochastic force is $\langle F_{\rm fluc}(t)F_{\rm fluc}(t')\rangle = 2\pi S_{\rm ff}\delta(t-t')$, where $S_{\rm ff}$ is the total fluctuation force spectral density, and $\delta(t-t')$ denotes that each collision on the particle surface by a gas molecule is independent of any other at any given time.

After a period of time $\sim 1/\Gamma_{\rm CM}$, the centre-of-mass motion of the nanoparticle reaches an effective thermal equilibrium characterized by an effective temperature:

$$T_{\rm CM} = \frac{\pi S_{\rm ff}}{k_{\rm B} M \Gamma_{\rm CM}}. \tag{2.45}$$

In higher pressures (about ≥ 10 mbar), we can consider that the centre-of-mass temperature $T_{\rm CM}$ is approximately equal to the temperature of the environment T_b due to very fast energy exchange. The thermal energy of the environment follows a Maxwell-Boltzmann distribution with a mean value of $k_{\rm B}T_{\rm b}$. Usually, it is suggested that the potential depth of a reasonable stable optical trap should be

at least $\approx 10k_{\mathrm{B}}T_{\mathrm{CM}}$ to prevent it from escaping, since the probability of finding the particle with energy $\geq 10k_{\mathrm{B}}T_{\mathrm{CM}}$ is less than 0.02% [31].

The position autocorrelation functions of $\langle q(t)q(0)\rangle$ is a common tool for analysing the position variable $q(t)$:

$$\langle q(t)q(0)\rangle = \frac{k_{\mathrm{B}}T_{\mathrm{CM}}}{M\omega_q^2} - \frac{1}{2}\sigma_q^2(t), \tag{2.46}$$

where $\sigma_q^2(t)$ is the position variance. The power spectral density (PSD) is defined by the position autocorrelation function:

$$S_{qq}(\omega) = \int_{-\infty}^{+\infty} \langle q(t)q(0)\rangle e^{i\omega t}\mathrm{d}t. \tag{2.47}$$

The PSD spectrum converts the time-trace signal to a frequency spectrum, providing a convenient tool for analysing the response of each degree of freedom in the frequency domain. Equation (2.45) can be further given by [7]:

$$S_{qq}(\omega) = \frac{k_{\mathrm{B}}T_{\mathrm{CM}}}{\pi M} \frac{\Gamma_{\mathrm{CM}}}{(\omega^2 - \omega_q^2)^2 + \Gamma_{\mathrm{CM}}^2\omega^2}. \tag{2.48}$$

Figure 2.2 presents the simulated PSD spectra of the centre-of-mass motion of a levitated nanosphere converted from the dynamics shown in Figure 2.1, from which we can obtain the oscillation frequency of 23.5 kHz in x, y-direction and 168.6 kHz in z-direction but with different amplitudes. The spectra of x and y-direction motion are completely overlapped in the simulation because of the systemic optical potential and perfect spherical shape of the nanoparticle; however, it shows some discrepancies in the experiments due to the asymmetry of the trap and geometry of nanoparticles. By fitting the PSD spectrum with Equation (2.48), the total damping rate Γ_{CM} and the temperature T_{CM} can be extracted. The integral of the peak area is proportional to the effective temperature of the motion of the levitated nanoparticle based on Equations (2.46) and (2.47).

In the case of two additional librational modes of the levitated nanorod, we assume the angle θ between the equilibrium position of the nanorod (normally

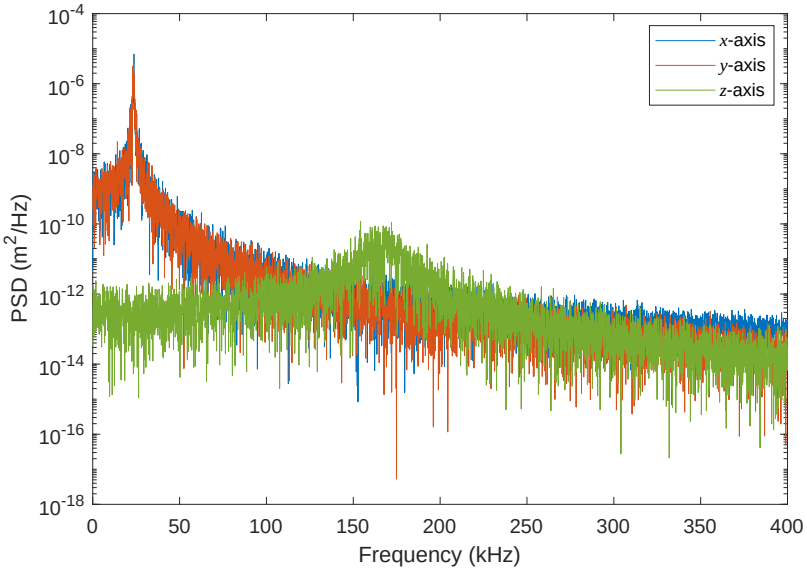

Figure 2.2: PSD spectrum converted from the dynamics of a 300 nm diameter levitated silica nanosphere in Figure 2.1. The PSD spectra of x, y-direction have the overlap frequency peak at 23.5 kHz, and a peak at 168.6 kHz appeared in the PSD spectrum of z-direction.

the polarisation direction of the linearly polarised light) and its angular position is small and the potential remains harmonic. The decoupled librational motions ($\theta \in \{\alpha, \beta\}$), by modifying Equation (2.43) accordingly, can be expressed as:

$$\ddot{\theta}(t) + \Gamma_{\mathrm{ROT}}\dot{\theta}(t) + \omega_\theta^2\theta(t) = \frac{1}{I}N_{\mathrm{fluc}}(t), \tag{2.49}$$

where $N_{\mathrm{fluc}}(t)$ is the associated stochastic torque which also can be regarded as:

$$\langle N_{\mathrm{fluct}}(t)N_{\mathrm{fluct}}(t')\rangle = 2I\Gamma_{\mathrm{ROT}}k_{\mathrm{B}}T_{\mathrm{b}}\delta(t-t'), \tag{2.50}$$

with the autocorrelation function of $\langle N_{\mathrm{fluc}}(t)N_{\mathrm{fluc}}(t')\rangle = 2\pi S_{\mathrm{nn}}\delta(t-t')$, where S_{nn} is the total fluctuation torque spectral density.

In analogue to the centre-of-mass motion discussed above, the effective temperature of librational motion becomes:

$$T_{\mathrm{ROT}} = \frac{\pi S_{\mathrm{nn}}}{k_{\mathrm{B}}I\Gamma_{\mathrm{ROT}}}. \tag{2.51}$$

and its PSD spectrum is given by:

$$S_{\theta\theta}(\omega) = \frac{k_{\mathrm{B}}T_{\mathrm{ROT}}}{\pi I}\frac{\Gamma_{\mathrm{ROT}}}{(\omega^2-\omega_\theta^2)^2+\Gamma_{\mathrm{ROT}}^2\omega^2}. \tag{2.52}$$

The linear stochastic dynamics of librational modes (α and β) of a levitated nanorod and its PSD spectrum are similar to translational modes shown in Figure 2.1 and Figure 2.2 but with the unit of the angle of $\mathrm{rad}^2/\mathrm{Hz}$.

2.3.2 Damping rate

Gas damping

For pressures higher than 10^{-6} mbar, the stochastic forces due to collisions with surrounding gas molecules is the dominant contribution to the total damping rate. The gas damping rate for a spherical nanoparticle is given by [99]:

$$\Gamma_{\mathrm{gas}} = \frac{6\pi\eta_{\mathrm{gas}}r}{M}\frac{0.619}{0.619+\mathrm{Kn}}(1+c_k), \tag{2.53}$$

where η_{gas} is the dynamic viscosity coefficient of gas, $\mathrm{Kn} = \bar{l}/r$ is the Knudsen number for the mean free path $\bar{l} = k_{\mathrm{B}}T_{\mathrm{gas}}/(\sqrt{2}\sigma_{\mathrm{gas}}P_{\mathrm{gas}})$ with the cross-sectional area σ_{gas} of the air molecules at the pressure P_{gas}. In the Knudsen regime (for pressures below $\sim$ 50 mbar), the mean free path of the gas molecules increases (e.g., $\bar{l} \sim 60\ \mu$m at 1 mbar) which is much larger than the radius of the nanoparticle $\mathrm{Kn} \gg 1$, the gas damping rate becomes linear with pressure [103]:

$$\Gamma_{\mathrm{gas}}^{\mathrm{Kn}>1} = \frac{8}{3}\sqrt{\frac{2m_{\mathrm{gas}}}{\pi k_{\mathrm{B}}T_{\mathrm{b}}}}r^2P_{\mathrm{gas}}, \tag{2.54}$$

where m_{gas} is the mass of gas molecules.

So far we have not considered the rotational degrees of freedom for a rotating nanosphere, which is given by:

$$\frac{\Gamma_{\mathrm{ROT,sphere}}}{2\pi} = \frac{30c_{\mathrm{acc}}}{8\sqrt{2}\pi}\frac{\eta_{\mathrm{gas}}\sigma_{\mathrm{gas}}}{k_{\mathrm{B}}T_b\rho}\frac{P_{\mathrm{gas}}}{r}, \tag{2.55}$$

where ρ is the density of particles, c_{acc} is accommodation coefficient character-

ized by $c_{\mathrm{acc}} = (T_{\mathrm{em}} - T_{\mathrm{gas}})/(T_{\mathrm{int}} - T_{\mathrm{gas}})$ with the surface temperature T_{int} and the temperature of the gas molecules emitted from the surface T_{em}. The accommodation coefficient quantifies the fraction of the thermal energy that the colliding gas molecule removes from the surface of the particle [103].

In our experiments, we also use the nanorod with geometry anisotropy, the gas damping rate becomes more complicated because the damping rate is orientation dependent, and the friction coefficient has to be replaced by a tensor [104]:

$$\begin{aligned}
\Gamma_{\mathrm{CM,rod}} &= \Gamma^{\perp}_{\mathrm{CM,rod}}(\mathbb{1} - \mathbf{m}\otimes\mathbf{m}) + \Gamma^{\parallel}_{\mathrm{CM,rod}}(\mathbb{1} - \mathbf{m}\otimes\mathbf{m}),\\
\Gamma^{\perp}_{\mathrm{CM,rod}} &= \frac{n_g r l\sqrt{2\pi m_{\mathrm{gas}} k_{\mathrm{B}} T_{\mathrm{gas}}}}{M}\left[2 + c_{\mathrm{acc}}\left(-\frac{1}{2} + \frac{\pi\gamma_s}{4} + \frac{r}{l}\right)\right],\\
\Gamma^{\parallel}_{\mathrm{CM,rod}} &= \frac{n_g r l\sqrt{2\pi m_{\mathrm{gas}} k_{\mathrm{B}} T_{\mathrm{gas}}}}{M}\left[4\frac{r}{l} + c_{\mathrm{acc}}\left(1 - 2\frac{r}{l} + \frac{\pi\gamma_s}{2}\frac{r}{l}\right)\right],
\end{aligned} \tag{2.56}$$

where n_g is the gas density, and the cylinder has a radius of r and length of l with symmetry axis $\mathbf{m}(\Omega)$. γ_s is given by the ratio of the surface temperature T_{int} of the trapped particle with respect to that of the gas temperature T_{gas} through $\gamma_s^2 = T_{\mathrm{int}}/T_{\mathrm{gas}}$.

Correspondingly, the rotational damping rate of a cylinder can be expressed as:

$$\begin{aligned}
\Gamma_{\mathrm{ROT,rod}} &= \Gamma^{\perp}_{\mathrm{ROT,rod}}(\mathbb{1} - \mathbf{m}\otimes\mathbf{m}) + \Gamma^{\parallel}_{\mathrm{ROT,rod}}(\mathbb{1} - \mathbf{m}\otimes\mathbf{m}),\\
\Gamma^{\perp}_{\mathrm{ROT,rod}} &= \frac{n_g r l\sqrt{2\pi m_{\mathrm{gas}} k_{\mathrm{B}} T_{\mathrm{gas}}}}{M}\frac{l^2}{3r^2 + l^2}\cdot\\
&\qquad \left\{2 + 12\frac{r^3}{l^3} + c_{\mathrm{acc}}\left[-\frac{1}{2} + \frac{\pi\gamma_s}{4} + 3\frac{r}{l} + 6\frac{r^2}{l^2} + \left(\frac{3\pi\gamma_s}{2} - 6\right)\frac{r^3}{l^3}\right]\right\},\\
\Gamma^{\parallel}_{\mathrm{ROT,rod}} &= \frac{n_g r l\sqrt{2\pi m_{\mathrm{gas}} k_{\mathrm{B}} T_{\mathrm{gas}}}}{M}\frac{l^2}{3r^2 + l^2} c_{\mathrm{acc}}\left(2 + \frac{r}{l}\right).
\end{aligned} \tag{2.57}$$

Radiation damping

When the gas pressure decreases to very low values (normally $\leq 10^{-6}$ mbar), the photon shot noise starts to dominate the damping term rather than the gas damping. The photon shot noise is due to the discrete photon nature of light,

leading to a damping rate of [26]:

$$\Gamma_{\mathrm{rad}} = \frac{c_{\mathrm{dp}} P_{\mathrm{scat}}}{Mc^2}, \tag{2.58}$$

where c_{dp} is the coefficient characterizing the direction of motion of the nanoparticle with respect to the polarisation of the laser: $c_{\mathrm{dp}} = 2/5$ for motion parallel to the polarisation direction while $c_{\mathrm{dp}} = 4/5$ for perpendicular. The scattered light power P_{scat} is:

$$P_{\mathrm{scat}} = \sigma_{\mathrm{scat}} I_{\mathrm{opt}}, \tag{2.59}$$

with the scattering section area $\sigma_{\mathrm{scat}} = (|\alpha_0|^2 k^4)/(6\pi\epsilon_0^2)$ and trapping light intensity I_{opt}. The equilibrium temperature provided by the photon energy when assuming the nanoparticle is only exposed to photon shot noise is given by:

$$T_{\mathrm{CM,PSN}} = \frac{\hbar\nu}{2k_{\mathrm{B}}}, \tag{2.60}$$

which is generally very high and necessitates continuous additional stabilizing and cooling [26]. The strong scattering introduces photon recoil heating, which destroys the coherent particle motion in high vacuum.

The photon shot noise also needs to be considered when we implement a quantum measurement of the position of levitated nanoparticles and feedback cooling its motions. There is a standard quantum limit that determines the minimized measurement uncertainty achieved by the balance between the measurement precision and the backaction from the photon shot noise.

Additional damping

In addition, the random forces and damping can be introduced via external fields which are under experimental control. For instance, the parametric feedback or cold damping schemes introduce additional damping to the levitated mechanical oscillator. This also alters the energy of the levitated nanoparticle with a different effective temperature which will be further discussed in Chapter 5.

Quality factor

The quality factor of a mechanical oscillator is defined by the total damping rates Γ_{CM} and the oscillation frequency ω_q:

$$Q = \frac{\omega_q}{\Gamma_{\mathrm{CM}}}. \tag{2.61}$$

This leads to a mechanical quality factor of levitated nanoparticles ranging from ~ 10 at 10 mbar to $\sim 10^8$ at 10^{-6} mbar, even can up to 10^{12} in ultra-high vacuum. Such a high-quality factor is normally difficult to achieve in many macroscopic mechanical systems due to the fundamental limits of dissipation. However, the significant improvement of quality factor in levitated mechanical oscillators will be beneficial to facilitate quantum coherent manipulation of mesoscopic objects.

2.4 Experimental apparatus

2.4.1 Overview

In this section, the experimental apparatus developed and implemented over the course of this thesis is presented in detail. This experimental apparatus is designed for studying the ro-translational optomechanics of levitated silica nanospheres and silicon nanorods, including trapping, control and cooling. Figure 2.3 shows the schematic of the experimental setup. All the optical components are placed on an air-compressed floating optical table for mechanical vibration isolation.

The following sections outline the optical layout, laser intensity and polarisation modulation, vacuum system, motion detection techniques and feedback loop. The nanoparticle sample preparation, nanoparticle loading method and its optical setup will be discussed in Chapter 3 in detail.

2.4.2 Optical layout

The core of the experimental setup is an optical trap formed by two counter-propagating laser beams and the nanoparticle is trapped at the centre of the optical trap. Compared to a single-beam dipole gradient dipole trap which requires a very high numeric aperture lens (e.g., NA > 0.8), the dual-beam optical trap takes the

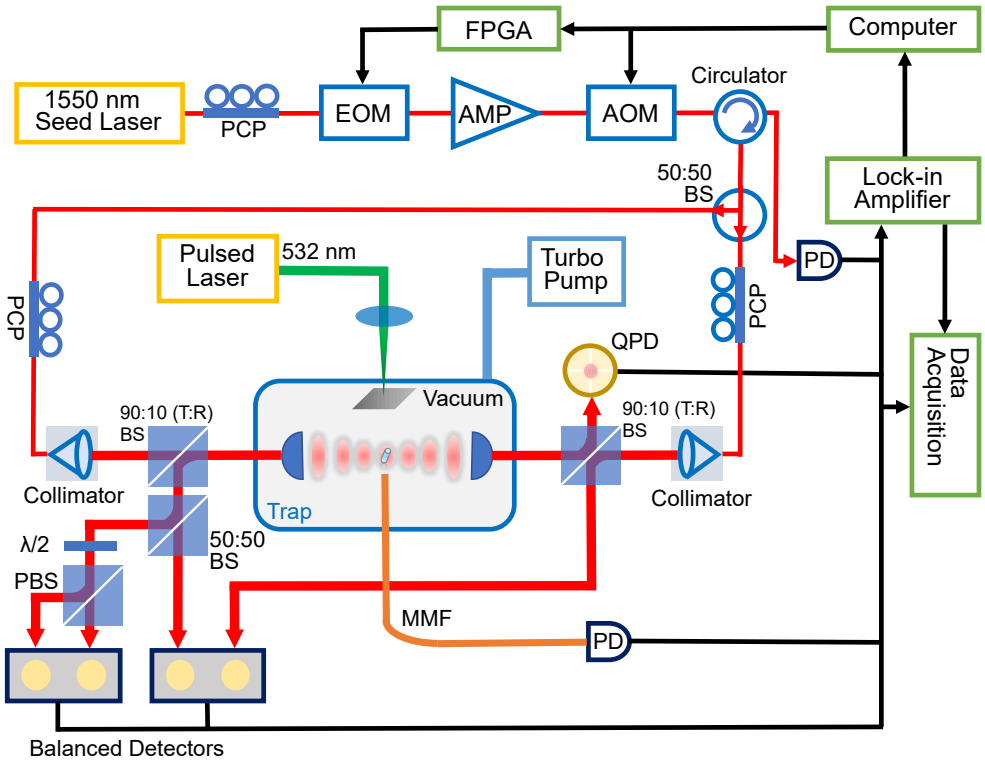

Figure 2.3: Schematic of the experimental setup. Two counter-propagating laser beams focused by a pair of lenses form a dual-beam optical trap inside a vacuum chamber. All the optical path is built with optical fibres, except for light propagating in free space output from two fibre collimators before incident into the vacuum chamber. The main optical path is started with a 1550nm high-power laser source. The intensity and polarisation state of two beams can be controlled by an in-fibre Acousto-optic modulator (AOM), in-fibre Electro-optic modulator (EOM) and polarisation control paddles (PCP). After the fibre circulator, the light is equally split into two branches by a 50:50 fibre beam splitter (BS). Before incident into a pair of focusing lenses inside the chamber, two beams are converted to free space to form a standing wave trap. The motion of levitated nanoparticles is detected by different detection schemes by using a single diode photodetector (PD) from a fibre circulator for all degrees of freedom, a balanced detector for z-motion, quadrant photodetector (QPD) for x, y-motion, polarisation beam splitter (PBS) and half-wave plate ($\lambda/2$) for α-motion and multimode fibre (MMF) for all degrees of freedom. These detection signals are sent to a data acquisition unit, lock-in amplifiers, and a computer with an FPGA module for data recording, processing and feedback. The vacuum condition is provided by connecting a turbo pump backed by a roughing pump. A separate optical setup for directly launching nanoparticles in vacuum consists of a 532 nm pulsed laser, reflecting mirrors and a focusing lens. The nanoparticle sample is held in a designed metal tube with a thin slot, making it closer to the trap centre and movable by a pair of magnets.

advantage of a lower NA lens, longer working distance and a larger trapping region. This takes the advantage of the scattering force from counter-propagating beams being mostly cancelled, therefore the gradient force with lower power is sufficiently strong to form a stable trap in all dimensions of confinements.

The laser source is provided by a 40 mW narrow linewidth, ultra-low frequency and intensity noise seed laser at the wavelength of 1550 nm (Koheras ADJUSTIK E15, NKT Photonics) and an erbium-doped fibre laser amplifier (Koheras BOOSTIK HP, NKT Photonics) which can amplify the seed laser up to about 2 W. At the wavelength of $\lambda = 1550$ nm, silica and silicon both have a relatively high permittivity and negligible absorption. After the light propagates through an optical fibre circulator, the light is equally split into two branches by a 50:50 fibre splitter. In order to form a standing wave trap, the in-fibre light becomes free space light with a beam size of 2.27 mm by two triplet fibre optic collimators (Thorlabs TC12FC-1550) before passing through the vacuum chamber. The two fibre collimators are mounted on two three-dimensional translational stages, which is not only good for beam alignment but also can adjust the position of antinodes of the standing wave by moving the stage along z-direction.

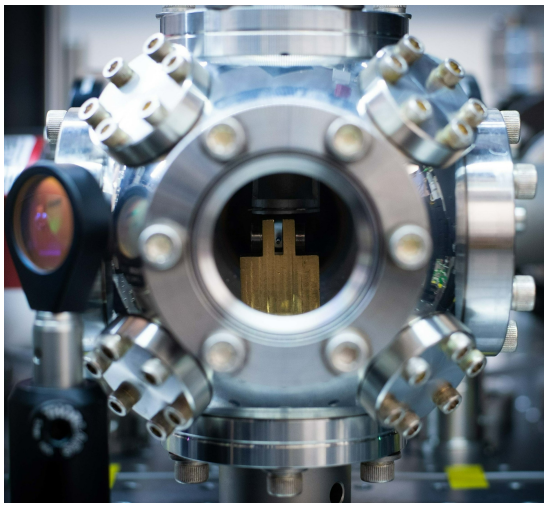

Figure 2.4: Parallel focusing lenses holder structure installed inside the vacuum chamber. A pair of aspheric lenses are screwed in and mounted on a designed and manufactured all-metal lens holder structure with its base firmly and flatly attached to the flange of the chamber.

Inside the vacuum chamber, as shown in Figure 2.4, a pair of aspheric lenses are screwed in and mounted on a designed and manufactured all-metal lens holder structure with its base firmly attached to the flange of the chamber. We have used lenses of NA = 0.30, 0.43 and 0.60 (Thorlabs C171TMD-C, C350TMD-C and C660TME-C) with an effective focal length of 6.20, 4.50 and 2.97 mm respectively, for different experiments.

During the setup process, these two beams need to be well-aligned with each other, yielding two beams exactly counter-propagating and focused on the same point. If these two beams are misaligned, the scattering force from each beam will not be cancelled, leading to a non-conservative trap and making it hard to trap particles stably, especially in a vacuum environment with very low gas damping. We use the fibre circulator for monitoring the quality of the alignment. After beam alignment, the amount of light in both arms passing the vacuum chamber achieves about 95%, and more than 50% in total is returned to the opposite collimator. The reason why the amount of light is not very high is the coupling loss from the collimator and insertion loss from other fibre components.

2.4.3 Laser intensity and polarisation modulation

By modifying the properties of the trapping light field, we can control the ro-translational dynamics of the levitated mechanical oscillator, and decrease (or increase) its energy through feedback control of the trapping laser. The parametric feedback cooling method we used to cool down the centre-of-mass temperature of the levitated nanoparticle requires a real-time modulation of light intensity [25], and the polarisation feedback cooling method for librational motion cooling requires a modulation of the polarisation state of light.

The light intensity of two beams is controlled by an in-fibre 80 MHz acoustic-optic modulator (AOM, Gooch & Housego FIBER-Q) before the light is into a 50:50 fibre splitter. The AOM is driven by a digital multi-function RF Synthesizer (MOGLabs Agile RF Synthesizer). It can also be amplitude-modulated with an input signal (or feedback signal) from detectors or lock-in amplifier outputs with a modulation bandwidth of 10 MHz. Normally, the amplitude of modulation is

small (less than 5%) based on the detection signal of the motion of the particle, thus the modulation range has a linear response to the input signal within the maximum driven power of the AOM driver.

The control of the polarisation state of light is achieved by a low-loss, high-speed lithium-niobate electro-optic polarisation modulator (EOM, EOSPCACE Polarisation Controller) with the combination of fibre polarisation paddles (PCPs) to set initial input polarisation state and phase compensation. The calibration process of the polarisation state is presented in Appendix A in detail.

2.4.4 Vacuum system

The main vacuum chamber (2.75" spherical cube, Kimball Physics) is evacuated by a combination of roughing pump (nXDS dry scroll pumps, Edwards vacuum) as first-stage evacuation and turbo-molecular pump (HiPace 300, Pfeiffer vacuum) with electronic drive unit (TC400, Pfeiffer vacuum) for further pumping. Between the vacuum chamber and the turbo-molecular pump is a vibration damper to isolate mechanical vibrations from pumps. A manually actuated angle valve (AVCO25, Pfeiffer vacuum) is installed between the chamber and the turbo-molecular pump, which is used to control the pressure inside the chamber and release the vacuum back into the atmosphere.

For the measurement and reading of the pressure inside the vacuum chamber, a wide-range vacuum Pirani/cold cathode gauge (PKR 360, Pfeiffer vacuum) is used and directly connected to the main chamber. This compact pressure gauge integrates two sensors with different measurement ranges, enabling accurate measurements from 1×10^{-9} mbar to atmospheric pressure. It also can be read out and controlled by the digital interface and integrated controller of the turbo-molecular pump.

In our system, the pressure can ultimately achieve the order of magnitude of 10^{-7} mbar (without bakeout) after several hours, which satisfies the requirement of our experimental conditions at the current stage. This vacuum system can also be modified and upgraded to go to lower pressure (e.g., below 10^{-9} mbar, ultra-high vacuum) with an ion pump.

2.4.5 Measurement techniques

Measurements of the displacement information of levitated nanoparticles are of critical importance for further manipulation and feedback cooling. Via the interactions with the optical field, the levitated nanoparticle scatters a part of the trapping light field, and its motion is primarily imprinted into the phase of the scattered light. Therefore, we can obtain the position information by directly detecting the scattered light from the nanoparticle, the interference with the trapping field, or mixing it with other reference signals.

Multi-mode fibre detection

To directly collect the scattered light, a bare, flat polished end of a 1 mm diameter multimode fibre (MMF, Thorlabs FP1000ERT) is placed close to the position where the nanoparticle is trapped around the beam waist, orthogonal to the axial axis of the standing wave trap, as shown in Figure 2.5.

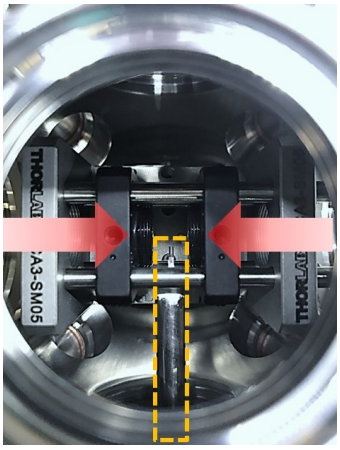

Figure 2.5: The top view of the optical trap with multi-mode fibre detection. The red arrows indicate the two counter-propagation trapping beams which are focused by a pair of lenses mounted on a cage structure in the base of a single-axis fibre bench. The yellow dashed line shows the MMF detection fibre.

The scattered light collected by MMF contains information on all degrees of freedom. Specifically for levitated nanorods, the scattered light also contains two additional rotational degrees of freedom $\{\alpha, \beta\}$. The light is guided by the MMF and focused on a fast, low-noise, and amplified InGaAs detector with a graded-

index (GRIN) lens (Thorlabs, GRIN2915) at the output port of MMF. Because the scattered light from the nanoparticle is very weak and only a proportion of it gets collected, we normally need to use a very sensitive photodetector with amplified circuits.

Since the light field scattered by the particle depends on the local intensity, and the intensity is symmetric about the field maximum, the MMF measurement returns the second harmonic of the particle motion. Figure 2.6 shows the time trace (top) and its frequency spectrum (bottom) of a levitated 300 nm diameter silica nanosphere in the standing wave trap under the pressure of 1 mbar. The first peak at $\sim$ 18 kHz frequency represents the trapping frequencies of x, y-direction and its second harmonic at $\sim$ 36 kHz. The other two peaks at $\sim$ 120 and $\sim$ 240 kHz represent the fundamental and second harmonic oscillation frequencies in z-direction. In this figure, the fundamental frequencies also appear owing to the slightly asymmetric position of the MMF, but the amplitude of peaks at the second harmonics are much stronger than the fundamental ones.

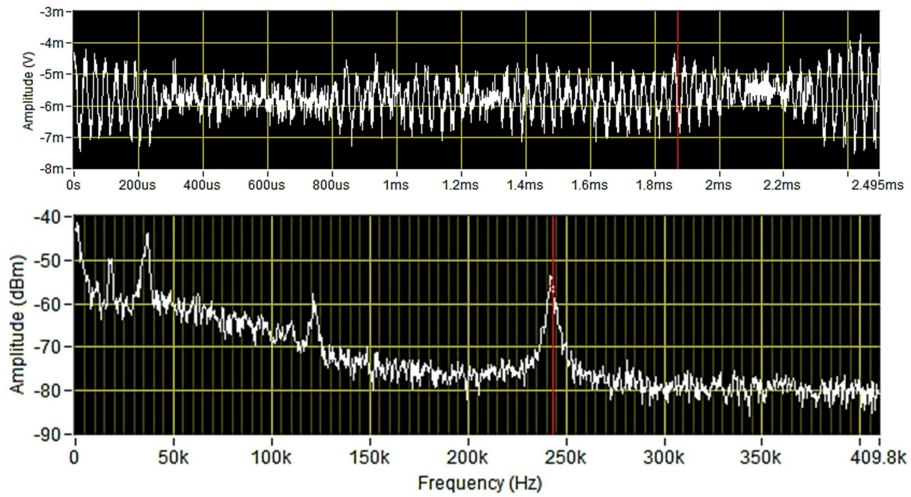

Figure 2.6: The time trace (top) and its frequency spectrum (bottom) of a levitated 300 nm diameter silica nanosphere in the standing wave trap under the pressure of 1 mbar. The peaks at the frequency of $\sim$ 18 and $\sim$ 36 kHz represent the trapping frequencies of x, y-direction and its second harmonic. The other two peaks at $\sim$ 120 and $\sim$ 240 kHz represent the fundamental frequency and its second harmonic in z-direction.

Differential detection

The differential detection method is a conventional interferometric detection technique for motion detection. It is based on the superposition of the unscattered field and the forward scattered field with a phase difference, which requires the common propagation path for both the trapping and scattered fields with matched wavefronts and phases.

In our experimental setup, the lens on each side naturally becomes the collection lens for the transmitted light from the other side. In the paraxial approximation, the scattered power coupled to the collection lens is approximately proportional to $(\mathrm{NA})^2$, which means increasing the NA of the illumination and collection optics would increase the amount of scattered field collected from the trap and the overall measurement cooperativity [105]. This is crucial for feedback cooling levitated oscillators by acquiring more information of their motion.

The interference of two fields has a constant phase relation of $\Delta\varphi = \pi/2$ due to the Gouy phase of transmitted light, which is detected by a photodetector. Therefore, the photodetector is sensitive to the phase of the scattered field imprinting the information of motion [31]. In this scenario, it has the highest sensitivity to the motion along the z-axis. In order to cancel the constant background trapping light offset, we focus a second beam (split from one of the trapping beams before the trap, as shown in Figure 2.3) on another port of the balanced detector with equal intensity.

In order to enhance the detection of the transverse motion in x- and y-direction, we use a quadrant photodiode detector (QPD) to detect x- and y-motion. When the nanoparticle moves in the transverse directions, its scattered field shifts with respect to the focus, causing a deflection of the transmitted light field in vertical x-direction or horizontal y-direction. A displacement in x-direction results in a light intensity increase of the top two quadrants of QPD while the bottom two decrease when the nanoparticle moves up, and vice versa. Similarly, a displacement in the y-direction results in an intensity change in the left and right halves of the detected interference on the QPD.

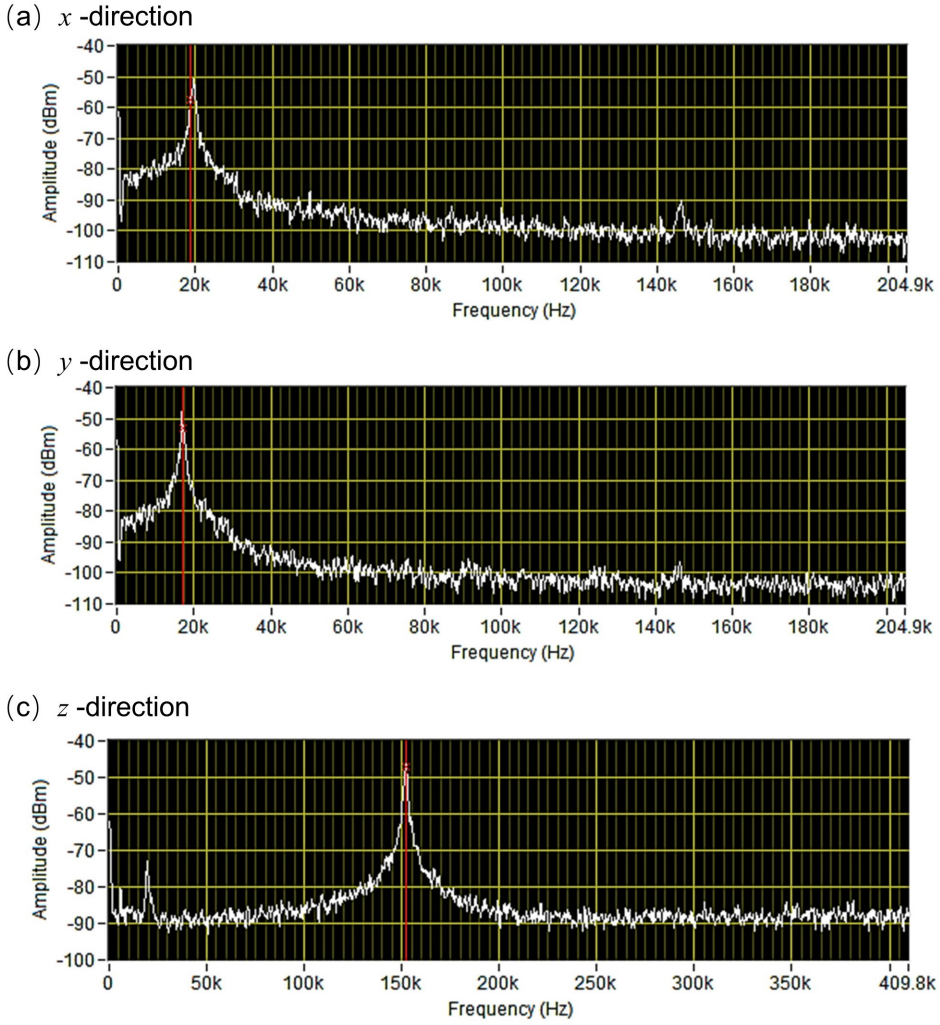

Figure 2.7: The frequency spectrum of a levitated 300 nm diameter silica nanospheres in the standing wave trap at 1 mbar. The x, y-direction signal (a) and (b) is detected by a QPD and z-direction (c) from a balanced detector.

Figure 2.7 shows the PSD spectrum of a levitated 300 nm diameter silica nanosphere with a pair of NA = 0.43 lenses and total trapping power of $\sim$ 300 mW under the pressure of 1 mbar. In practice, it shows a small z-motion in x-direction detector, but the elimination of the y-motion. This can be explained by the imperfect alignment of the optics. Similarly, the frequency spectrum of z-motion also contains the x, y-motion which in principle should be completely suppressed. As a critical experimental technical challenge in various optomechanical systems, the laser intensity fluctuations and drifts cause the drifts of trapping frequencies, as shown in three subfigures of the frequency drift in z-motion at different data

acquisition time. This laser intensity noise could heat up the levitated mechanical oscillator and increase the phase error in the feedback scheme, which may need to be suppressed by intensity stabilization techniques.

For detecting the rotational motion of levitated nanorods, we implement a differential detection based on a polarisation measurement. The nanorod rotates the polarisation of the trapping light [53]. A polarizing beam splitter (PBS) and a half waveplate are placed in front of a balanced detector which is sensitive to the α-motion. A similar detection scheme for β-motion in the transverse plane is implemented, which is not shown in Figure 2.3.

Figure 2.8 (a) and (b) present the frequency spectrum from α-motion detector of a levitated silicon nanorod trapped with linearly polarised and circularly

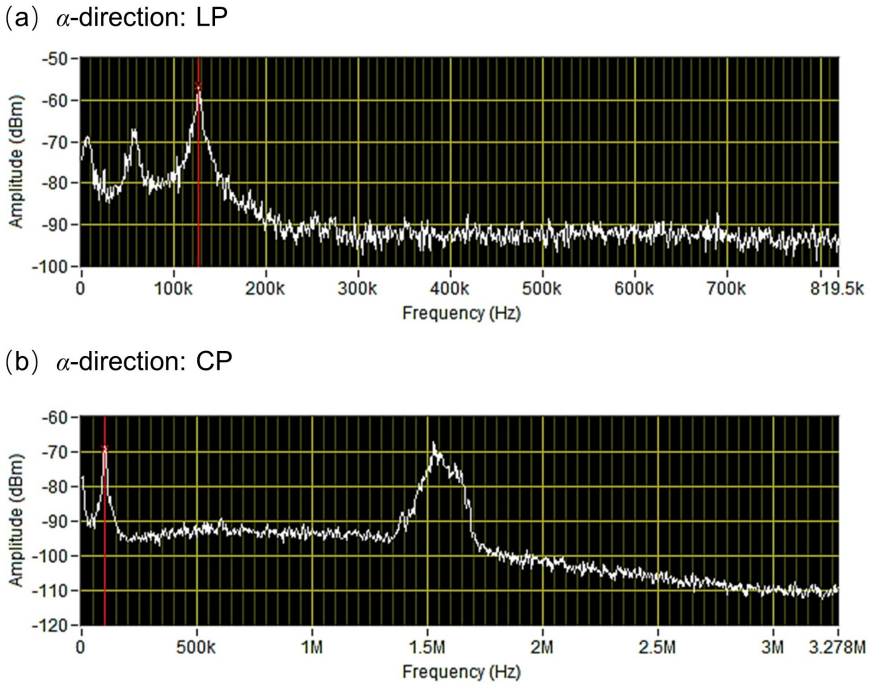

Figure 2.8: Frequency spectrum from α-direction detector of a levitated silicon nanorod trapped with linearly polarised light (a) and circularly polarised light (b). With the linearly polarised light, the nanorod shows a librational motion at $\sim$ 60 kHz in addition to x, y-motion at $\sim$ 9 kHz and z-motion (red line) at $\sim$ 128 kHz. When the polarisation state of the trapping light switches to circularly polarised, the librational mode vanishes and the nanorod is driven to a full rotation in the polarisation plane (α-direction), and a signal at $\sim$ 1.5 MHz is observed corresponding to a rotation rate of $\sim$ 0.75 MHz.

polarised light respectively. With the linearly polarised light, the nanorod exhibits a librational motion at $\sim$ 60 kHz in addition to x, y-motion at $\sim$ 9 kHz and z-motion at $\sim$ 128 kHz. When the polarisation state of the trapping light switches to circularly polarised, the librational mode vanishes and the nanorod is driven to a full rotation in the polarisation plane (α-direction) and a signal at $\sim$ 1.5 MHz observed corresponding to a rotation rate of $\sim$ 0.75 MHz.

Balanced homodyne and heterodyne detection

Alternatively, we can choose a different reference beam with adjustable optical intensity, rather than using the trapping field discussed above, mixing with the scattered light for balanced interferometric detection. When the reference beam has the same optical frequency as the frequency of the signal, the detection scheme is called homodyne detection; on the contrary, the reference beams have different oscillation frequencies in heterodyne detection. By adopting the balanced scheme, it can effectively cancel out the average DC components while the high frequency oscillation term remains.

Figure 2.9 sketches the balanced homodyne and heterodyne detection methods. The homodyne detection has two inputs: one is from the scattered field $\mathbf{E}_{\text{scat}}$ and another is an independent reference $\mathbf{E}_{\text{LO}}$ from the local oscillator. After being mixed by a beam splitter, two outputs E_+ and E_- are sent to a balanced

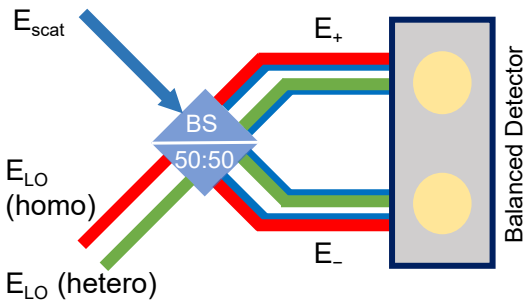

Figure 2.9: Sketch of balanced homodyne (red) and heterodyne (green) detection methods for detecting the scattered filed (blue) of levitated nanoparticles. Two input fields are mixed by a 50:50 beam splitter, and two outputs E_+ and E_- are differentiated by a balanced detector.

photodetector with:

$$\begin{aligned} E_+ &= \frac{1}{\sqrt{2}}\left(E_{\mathrm{scat}}e^{i\varphi_{\mathrm{scat}}} + E_{\mathrm{LO}}e^{i\varphi_{\mathrm{LO}}}\right), \\ E_- &= \frac{1}{\sqrt{2}}\left(E_{\mathrm{scat}}e^{i\varphi_{\mathrm{scat}}} + E_{\mathrm{LO}}e^{i(\varphi_{\mathrm{LO}}+\pi)}\right), \end{aligned} \tag{2.62}$$

for the case of two outputs with equal intensity. The output from the balanced detector is:

$$I_{\mathrm{out}} = 2E_{\mathrm{scat}}E_{\mathrm{LO}}\cos(\varphi_{\mathrm{scat}} - \varphi_{\mathrm{LO}}), \tag{2.63}$$

where the phase of the reference beam φ_{LO} is adjustable for measuring the phase quadrature of the signal (i.e., the scattered field). Usually, the amplitude of the signal E_{scat} is much weaker than the reference beam, thus it can be amplified by E_{LO}. Therefore, the amplitude of the reference beam E_{LO} can be optimised to acquire an optimal signal-to-noise ratio.

For a balanced heterodyne measurement with a frequency difference $\Delta\nu$, the balanced detector output becomes:

$$I_{\mathrm{out}} = 2E_{\mathrm{scat}}E_{\mathrm{LO}}\cos(\varphi_{\mathrm{scat}} - \varphi_{\mathrm{LO}} + \Delta\nu t). \tag{2.64}$$

Looking at the spectrum of balanced detector output, it is shifted to $\Delta\nu$ with sidebands at $\Delta\nu \pm \omega_{\mathrm{scat}}$. This is beneficial to shift high frequencies with a lower noise floor when choosing $\Delta\nu \gg \omega_{\mathrm{scat}}$. In contrast to homodyne detection, where the phase relationship between two fields is fixed, the reference beam from the local oscillator) in the heterodyne measurement is continuously scanning between the amplitude and phase quadrature of the output. By using a lock-in amplifier that locks to the modulation frequency $\Delta\nu$, we can measure the amplitude and extract the phase information. The heterodyne detection can be used to perform an out-of-loop measurement of the particle's energy via Raman scattering thermometry by measurement of the ratio of the Stokes and anti-Stokes scattering rates [30, 29, 27].

2.4.6 Feedback loop

In order to feedback cool the centre-of-mass and rotational motion of the levitated particle by modulating the intensity and polarisation of the trapping light, it is crucial to build a high-speed, low-electronic noise feedback loop. In a simple way, the feedback electronics consists of a bandpass filter, a phase shifter, a frequency doubler, an amplitude amplifier, and an adder [25], which are already integrated into the 50 MHz lock-in amplifier (HF2LI, Zurich Instruments). We use the phase-locked loop (PLL) of the lock-in amplifier to simultaneously track the phase of the particle's motion at different oscillation frequencies and generate a feedback signal.

A PLL uses a local voltage-controlled oscillator (VCO), and a phase comparator to maintain a constant phase difference between the local oscillator and an input signal from photodetectors. The VCO has a starting phase, and a phase detector measures the difference between this and the input signal. The resulting error signal is then passed through a filter system which removes phase noise and generates a DC signal. The DC signal is used to feed into the VCO and used to change the VCO output frequency. This loop continues until the phase difference between the input signal and VCO is minimal or reaches some set phase difference.

The output signal from PLLs is added and amplified as needed before sending to the amplitude modulation input of the AOM driver in parametric feedback cooling, or EOM in polarisation feedback cooling.

This function also can be achieved by programming a fast FPGA module (e.g., STEMlab 125-10, Red Pitaya) which is expected to meet the requirement of high-speed signal acquisition, processing, and output signals in the range of several hundreds of kHz.

Chapter 3

Direct Loading of Nanoparticles in Vacuum

3.1 Introduction

Controllable nanoparticle loading into an optical trap in vacuum is one of the main challenges for optical levitation and control. There are some strategies to transport externally trapped particles into the chamber using a load-lock technique [106, 107] or a hollowcore fibre [108]; however, developing direct loading methods in vacuum is also important for precision measurements and sensing applications.

Due to the conservative nature of optical potentials, a dissipation mechanism is required to load nanoparticles into the optical trap. A current common direct loading technique is to suspend nanoparticles in a solvent and then introduce them into the gas phase through nebulization in ambient conditions. The particles then diffuse to the optical trap and are captured, typically after a few minutes in the atmosphere, after which the pressure is reduced for the next step of experiments. This method has some drawbacks, one of which is the risk of easily contaminating the vacuum system and delicate optics in the trapping region. In addition, absorption of the solvent into porous dielectric nanoparticles. Nebulization also relies on having a large number of nanoparticles available, since the method is highly probabilistic, therefore, it is not suitable for small samples of tailored nanorods we used for the research of rotational optomechanics in this thesis.

In this chapter, we report on a dry and vacuum-compatible method for directly launching nanoparticles into optical traps, namely Laser-Induced Acoustic Desorption (LIAD). In this method, a high-energy pulsed laser is focused onto the back side of a substrate upon which particles are distributed or grown. The pulse can generate acoustic shock waves through thermo-mechanical stress to locally eject particles from the substrate, and then fall into the optical trap.

LIAD has been used for launching biological cells [109], strands of DNA [110] and silicon particles [17]. This method can overcome Van der Walls force between the particles coated onto a surface, and launch tethered silicon nanoparticles directly from their silicon substrate. The particles are only ejected from the region of the laser focus, allowing selective and efficient launching. LIAD works for dielectric particles from <100 nm up to several micrometres at pressures down to 1 mbar or even lower for other types of traps (e.g., Paul traps) [111]. This method is also possible to practically launch individual nanoparticles during each launch.

We characterized the LIAD method as a technique for loading nanoparticles into our standing-wave optical trap, presenting an efficient, flexible, clean, and vacuum-compatible tool for the field of levitated optomechanics.

3.2 Launch mechanism

3.2.1 Buffer gas model

The interactions between nanoparticles and residual gas molecules provide the dissipative mechanism when we use LIAD to load nanoparticles directly into the conservative optical trap. Different from the previously mentioned nebulization techniques, this loading method does not over-rely on the diffusion of nanoparticles into the trapping region; on the contrary, nanoparticles are directed towards the trapping region by the LIAD mechanism, dramatically increasing the efficiency of trap loading. During the transit through a gas, launched nanoparticles get slowed down and lose some energy before reaching the conservative trap.

We begin by assuming that the nanoparticles are launched with a constant initial vertical velocity without initial transverse velocity spread. The equation

describing this process, without considering diffusion, is given by:

$$M\ddot{x} = -Mg - \Gamma_{\text{gas}}\dot{x}, \tag{3.1}$$

where M is the mass of nanoparticles, g is the acceleration due to gravity, and x is the position of the nanoparticle where positive x is upwards. In this chapter, we consider the total damping rate is only from the gas damping Γ_{gas}.

By solving Equation (3.1), the vertical position (along the gravity direction) of the particles is:

$$x(t) = \left(1 - e^{-\frac{\Gamma_{\text{gas}}t}{M}}\right)\left(\frac{gM^2}{\Gamma_{\text{gas}}^2} + \frac{v_0 M}{\Gamma_{\text{gas}}}\right) - \frac{gMt}{\Gamma_{\text{gas}}}, \tag{3.2}$$

where v_0 is the initial velocity, which, in our case, is negative, and normally of the order 30 ms^{-1} (referring to the experimentally measured data shown in Figure 3.7 (a) in Section 3.4).

In the experiment, we detect the scattered light of nanoparticles only when they arrive at the optical trap, from which we can extract the information on how long they take during falling and how fast they are going. The distance between the substrate and the optical trap centre is defined as x_{trap}, the time to reach the trap centre as t_{trans}, and the velocity at the trap as v_{fin}. It is straightforward to numerically solve Equation (3.2) to extract t_{trans} for a given x_{trap}. The velocity is then found by differentiating Equation (3.2):

$$v_{\text{fin}} = -\frac{gM}{\Gamma_{\text{gas}}} + \left(\frac{gM}{\Gamma_{\text{gas}}} + v_0\right) e^{-\frac{\Gamma_{\text{gas}} t_{\text{trans}}}{M}}. \tag{3.3}$$

The momentum damping coefficient for the nanoparticle Γ_{gas} gives the rate at which an object of a given mass relaxes to its terminal velocity v_{T}:

$$\Gamma_{\text{gas}}(v_{\text{T}}) = \frac{gM}{v_{\text{T}}}. \tag{3.4}$$

The terminal velocity v_{T} depends on the viscosity μ_{N} of the fluid, Nominally, viscosity is independent of pressure, however, one must consider the interaction

with the surface of the particle when considering fluid dynamics, as well as the fact that small particles can travel quite some distance in gas between collisions. The slip factor C_S accounts for this, and is shape dependent. The terminal velocity is given by:

$$v_\mathrm{T} = \frac{4\rho_\mathrm{S} R_\mathrm{S} g C_\mathrm{S}}{18\mu_\mathrm{N}}. \tag{3.5}$$

For a spherical nanoparticle,

$$C_\mathrm{S} = 1 + \frac{\bar{l}}{2r}\left(2.34 + 1.05e^{-0.39\frac{2r}{\bar{l}}}\right), \tag{3.6}$$

where $\bar{l}$ is the mean free path of the gas molecules with number density n_g and effective radius of N_2 gas r_b given by:

$$\bar{l} = \frac{1}{4\sqrt{2}\pi n_g r_\mathrm{b}}, \tag{3.7}$$

and the viscosity of N_2 gas μ_N is gas temperature T_gas dependent, given by:

$$\mu_\mathrm{N} = 1.781 \times 10^{-5} \frac{411.55}{T + 11}\left(\frac{T_\mathrm{gas}}{300.55}\right)^{\frac{3}{2}}. \tag{3.8}$$

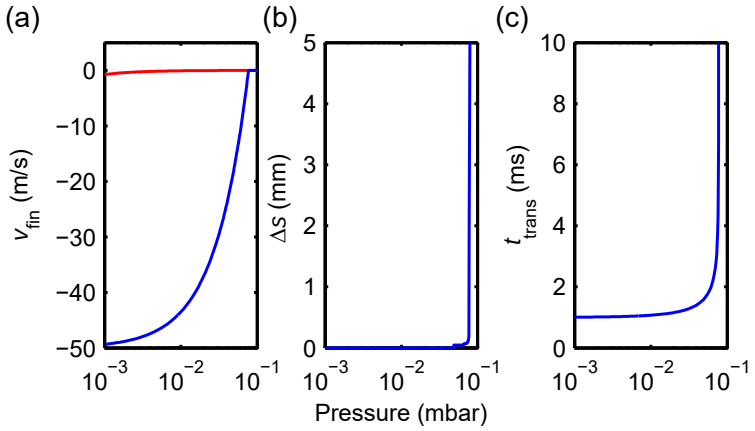

Figure 3.1: The simulation of a nanosphere during transit of a buffer gas with a set initial velocity. The particle is launched downwards at $v_0 = 50$ ms^{-1} through room temperature N_2 of varying pressure from a substrate with the distance away from the trap of $x_\mathrm{trap} = 5$ cm. (a) The final velocity approaches the terminal velocity (red line) at high pressures. (b) The divergence of the beam sharply increases with pressure, since the particle has more time to undergo multiple collisions with the gas, as shown in (c).

The simulation of the effect of buffer gas on the velocity of a nanoparticle of a fixed initial velocity v_0 is shown in Figure 3.1 (a). The velocity v_{fin} at the plane of interest x_{trap} decreases with increasing pressure, until it reaches the terminal velocity v_{T}, which for these conditions is less than 1 mm s^{-1} by 10^{-1} mbar. Practically, nanoparticles are not launched with a single velocity, but with a velocity distribution. In Figure 3.2, we consider the effect of a buffer gas on an initial Maxwell-Boltzmann distribution of velocities. As the pressure of the buffer gas increases, once the particles reach x_{trap} they have been redistributed to lower velocity.

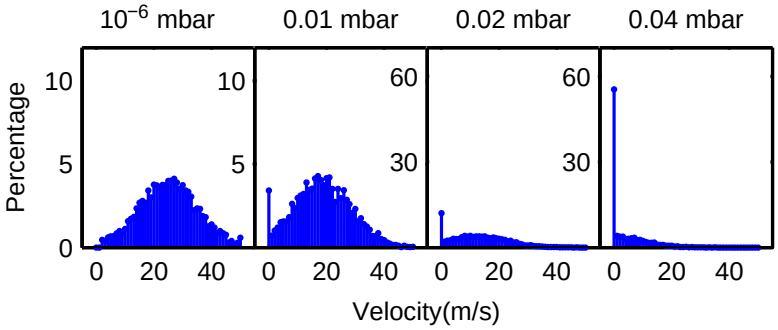

Figure 3.2: Simulation on the effect of buffer gas on nanoparticles with a Maxwell-Boltzmann velocity distribution. Here the distribution has a mean value of 25 ms^{-1} with a width of 10 ms^{-1}. As the pressure of the gas increases, the lowest velocity class is predominantly populated. The vertical scale in the first two is 6 times smaller than the latter two.

For other types of nanoparticles in which we are interested, nanorods are roughly cylinders of length l and radius r, with the aspect ratio of $p = l/(2r)$. In order to compare the behaviour of these particles to nanospheres, it is convenient to define the equivalent sphere radius $\tilde{R}_{\text{S}}$ of a sphere with the same volume as the nanorod. We also define an effective hydrodynamic (or Stokes) radius $\tilde{R}_{\text{C}}$ to describe the interaction of the sphere with the gas, which for a cylinder is [112]:

$$\begin{aligned}\frac{\tilde{R}_{\text{C}}}{\tilde{R}_{\text{S}}} = 1.0304 &+ 0.0193\ln p + 0.06229(\ln p)^2 \\ &+ 0.00476(\ln p)^3 + 0.00166(\ln p)^4 \\ &+ 2.66 \times 10^{-6}(\ln p)^7.\end{aligned} \tag{3.9}$$

Due to the fact that cylinders in dilute fluids (i.e., low pressure gas) have not been studied much, we assume the slip factor C_S in Equation (3.6) should be applicable for any solid object. Thus, for the slip factor C_C of a cylinder, we simply replace the radius in the Equation (3.6) by $\tilde{R}_C$. The diffusion constant for translational motion of a cylinder D_t becomes [113]:

$$D_t = \frac{C_C k_B T_{gas}(\ln p + c_t)}{3\pi\mu_N L}, \tag{3.10}$$

where c_t is the translational end-effect coefficient, given by [113]:

$$c_t = 0.312 + \frac{0.565}{p} - \frac{0.1}{p^2}. \tag{3.11}$$

The translational momentum damping factor Γ_t is then given by the Fluctuation-Dissipation theorem as $\Gamma_t = k_B T/D_t$, and this also can be applicable for the sphere by following the same process.

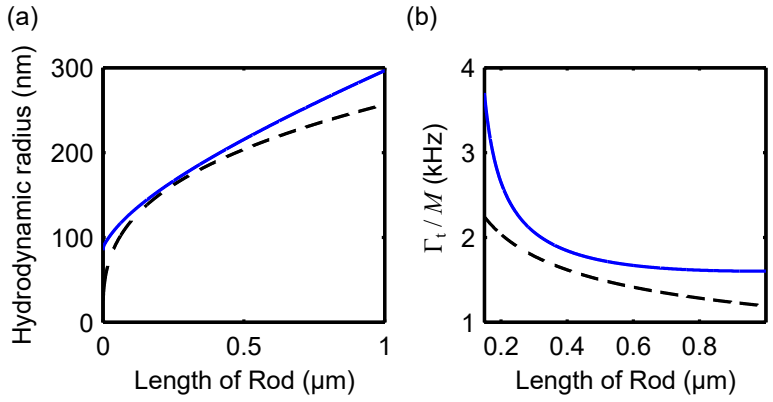

Figure 3.3: Comparison of the hydrodynamic radius and momentum damping rate of cylinders and spheres with the same volume and mass. Solid blue lines show the cylinder data and dashed black lines are spheres. These results are for N_2 at 1 mbar pressure. The diameter of cylinders is fixed to 300 nm. (a) The variation in hydrodynamic radius with cylinder length. When the length and diameter of the cylinders are similar the cylinders and spheres behave similarly, but the radii diverge when the cylinders become disc-like ($L \ll d$) or very long ($L \gg d$). (b) The variation in momentum damping rate Γ_t/M with cylinder length. It is noted that the cylinders only vary from the spheres when they become very disc-like or very long.

The hydrodynamic radius $\tilde{R}_{\mathrm{C}}$ and the momentum damping factor Γ_{t} for cylinders is compared to the equivalent quantities for spheres in Figure 3.3. Neither quantity varies by a significant amount compared to a sphere, unless the rods are very long and thin, or very disc-like. In our experiments, $p \approx 2 \sim 5$, and hence all of the conclusions showed in this chapter hold for spheres and rods.

Another important discussion is about the rotation of the nanorods or nanospheres. It is possible to calculate the damping on this motion, but it is considerably smaller than the translational damping [113]. The translational damping on the motion of a sphere is approximately proportional to r, whereas the rotational damping is proportional to r^3, and both types of damping have proportionality constants of the same order of magnitude. The same proportionalities hold for cylinders, but one must consider the length l replaced by r. This means that for a cylinder of length 1 μm the rotational damping is 12 orders of magnitude smaller than the translational damping. The argument holds for all axes of rotation. This means buffer gasses are not a good way of slowing rotation, only very viscous fluids have the capability. This is also consistent with our experimental observations on the slowing of rotating nanorods.

3.2.2 Brownian diffusion

In this section, we consider the effect of diffusion in the transverse direction ($s \in \{y, z\}$) during the falling of launched nanoparticles due to Brownian motion. The mean transverse position of the particle should be zero $\langle s(t) \rangle = 0$ due to the average force being zero; however, its variance or the mean-square displacement is non zero [99]:

$$\sigma_s^2(t) = \left\langle [s(t) - s(0)]^2 \right\rangle = \frac{2k_{\mathrm{B}}T_{\mathrm{CM}}}{M\Gamma_{\mathrm{CM}}^2} \left[\Gamma_{\mathrm{CM}} t - 1 + e^{-\Gamma_{\mathrm{CM}} t} \right]. \tag{3.12}$$

For a long time scale ($t \gg 1/\Omega_{\mathrm{CM}}$), the variance is the same as that predicted by Einstein's theory of diffusion:

$$\sigma_s^2(t) = 2Dt, \tag{3.13}$$

where $D = (k_B T_{CM})/(M\Gamma_{CM})$ is the diffusion constant. In this regime, the dynamics are completely random which indicates the trajectory of the nanoparticle is fractal and, thus, is continuous but not differentiable. But at short time scales ($t \ll 1/\Gamma_{CM}$), the trajectory of the particle becomes ballistic as a free particle, which is dominated by its inertia.

We define the transverse spread Δs as:

$$\Delta s(t) = \sqrt{2Dt}. \tag{3.14}$$

with an average time τ between collisions given by:

$$\tau = \frac{l_s}{v_{th}}, \tag{3.15}$$

where $l_s = (8D)/(\pi v_{th})$ is the mean free path of the particle with thermal velocity of:

$$v_{th} = \sqrt{\frac{8k_B T_{gas}}{\pi M}}, \tag{3.16}$$

and the transit time t_{trans} is compared to τ with each collision causing a displacement $\Delta s(\tau)$.

The spread Δs is shown in Figure 3.1 (b). For a large range of pressures, there are too few collisions during t_{trans} to cause significant diffusion. However, once there are enough collisions, the forward velocity is also significantly slowed, t_{trans} increases, shown in Figure 3.1(c), and there is a further chance for diffusion to occur. Hence both the diffusion and the arrival time increase exponentially as the nanoparticle is slowed.

We simulate the Brownian motion of the particles undergoing transverse diffusion by numerically solving the stochastic differential equation (i.e., Equation (2.43)) with a white noise term $W(t)$. This term $W(t)$ satisfies the Wiener process:

$$W(t) \sim \sqrt{t} \cdot N(0,1), \tag{3.17}$$

where $N(0,1)$ is the normal distribution.

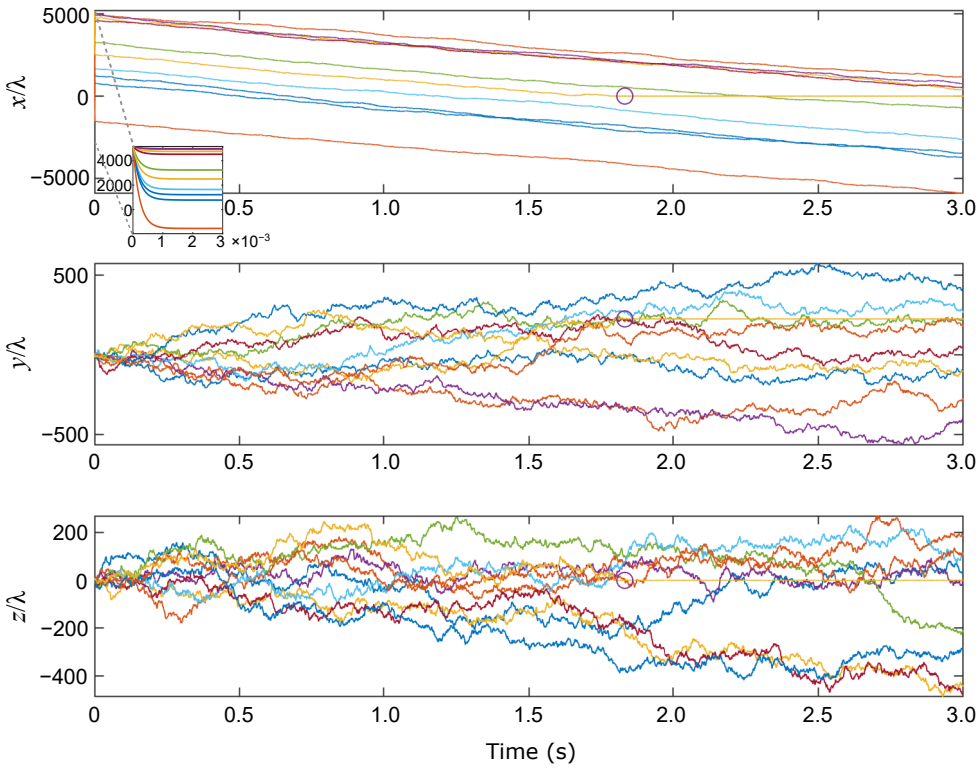

Figure 3.4: Simulation on the dynamics of nanoparticles undergoes Brownian diffusion during falling. Example of time traces showing the positions of 10 silica nanospheres (150 nm radius) released from a position of 8 mm right above the trap centre in three directions (the vertical axis is set to the position in units of wavelength). The initial velocity along x-direction (gravity direction) is set to velocity distribution based on the experimental result. The left bottom inset shows the zoom-in of the initial 3×10^{-3} s. The wavelength of the trapping light is $\lambda = 1550$ nm and the optical power is 0.3 W. The optical trap beam waist is 3.0 μm. The gas pressure is 2 mbar at the temperature of 298 K. In this figure, one of ten nanoparticles successfully get trapped during a 3 seconds transit process, indicated by a circle after about 1.83 s. The threshold defined for judging the trap events is the motion of the nanoparticle is within the range of two wavelengths in all axes.

For a differential form of the Wiener process, it is proportional to $\sqrt{\mathrm{d}t}$ with a discretization time $\mathrm{d}t$ in the time variable:

$$\mathrm{d}W(t) \simeq \sqrt{\mathrm{d}t} \cdot N(0,1). \tag{3.18}$$

The continuous-time solution $s(t)$ of the stochastic differential equation is

approximated by a discrete-time sequence s_i at time t_i with a sufficiently small time step $t_i = i\mathrm{d}t$, and replacing $s(t), \dot{s}(t)$ and $\ddot{s}(t)$ by s_i, $(s_i - s_{i-1})/\mathrm{d}t$ and $(s_i - 2s_{i-1} + s_{i-2})/(\mathrm{d}t)^2$ based on the Euler method [114]. The solution of this Euler approximation remains a Markov process. Other generalized numerical methods for solving the stochastic differential equations such as Runge-Kutta methods can be used for higher orders.

Figure 3.4 shows an example of the trajectories of 10 silica nanospheres with a radius of 150 nm released from a position of 8 mm right above the trap centre in three directions. The initial velocity along y-direction is set to velocity distribution based on the experimental result in Figure 3.7. The wavelength of the trapping light is $\lambda = 1550$ nm and the optical power is set to 0.3 W with a beam waist of 3.0 μm. The gas pressure is 2 mbar at the temperature of 298 K. From this figure, we can see the Brownian diffusion in y- and z-direction while the gravity direction along x-axis is approximately ballistic in such a short time scale in a dilute gas environment. In this simulation, one of ten nanoparticles successfully get trapped during a 3 seconds transit process, indicated by a circle after about 1.83 s. The threshold defined for judging the trap events is that the motion of the nanoparticle is within the range of two wavelengths in all axes.

3.3 Nanoparticle source and optical setup for LIAD

3.3.1 Sample preparation

We use non-functionalize dry silica nanospheres (Bangs Laboratory) with 300 nm diameter and nano-fabricated silicon nanorods (Kelvin Nanotechnology) with a length of 880 nm and diameter of 210 nm etched with a separation of 8 μm and an under etched breaking-point, following the work presented in [115], as shown in Figure 3.5 (a) and (b). We first use silica nanospheres to test the performance of the optical trap and obtain important experimental parameters.

About 1 mg of 300 nm diameter silica nanospheres are dispersed in 2 mL of isopropanol solution and sonicated in an ultrasonic bath for an hour to prevent

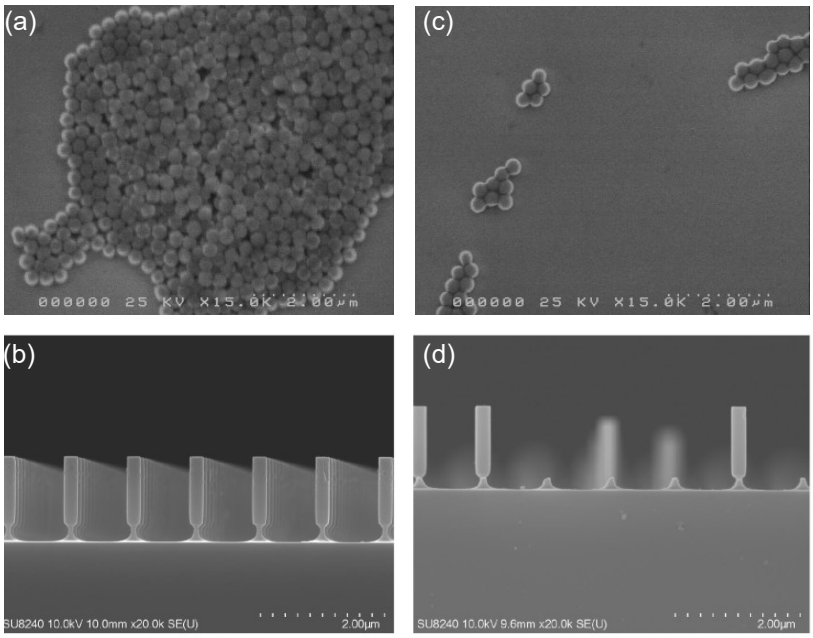

Figure 3.5: (a) Scanning Electron Micrograph (SEM) image of 300 nm diameter silica nanospheres spin-coated on an aluminium foil. (b) SEM image of Nano-fabricated silicon nanorods etched on a silicon substrate with narrow break-points near the base; after serval rounds of LIAD launch, SEM images of (c) nanospheres sample and (d) nanorods sample.

aggregation and uniformly disperse the particles in the liquid. A drop of diluted solution containing evenly suspended nanoparticles is pipetted onto around 1 cm^2 of an aluminium sheet of 400 μm thickness. A rigid aluminium sheet as a substrate has been shown to produce a lower mean launch velocity than aluminium foil, silicon wafer, or titanium foil [116]. The sample is allowed to dry for several hours and placed inside the vacuum chamber 8 mm above the optical trap with the nanoparticles facing towards the trap.

3.3.2 Optical setup

As discussed in the previous chapter, our optical trap is formed within the vacuum system by two counter-propagating focused laser beams with a wavelength of 1550 nm, where each beam possesses an identical polarisation. The trapping light is back coupled through the optical system and separated by an optical fibre circulator onto a photodiode. This signal is maximized to ensure optimal alignment of the trapping beams and provides a read-out of the trapped nanoparticle motion.

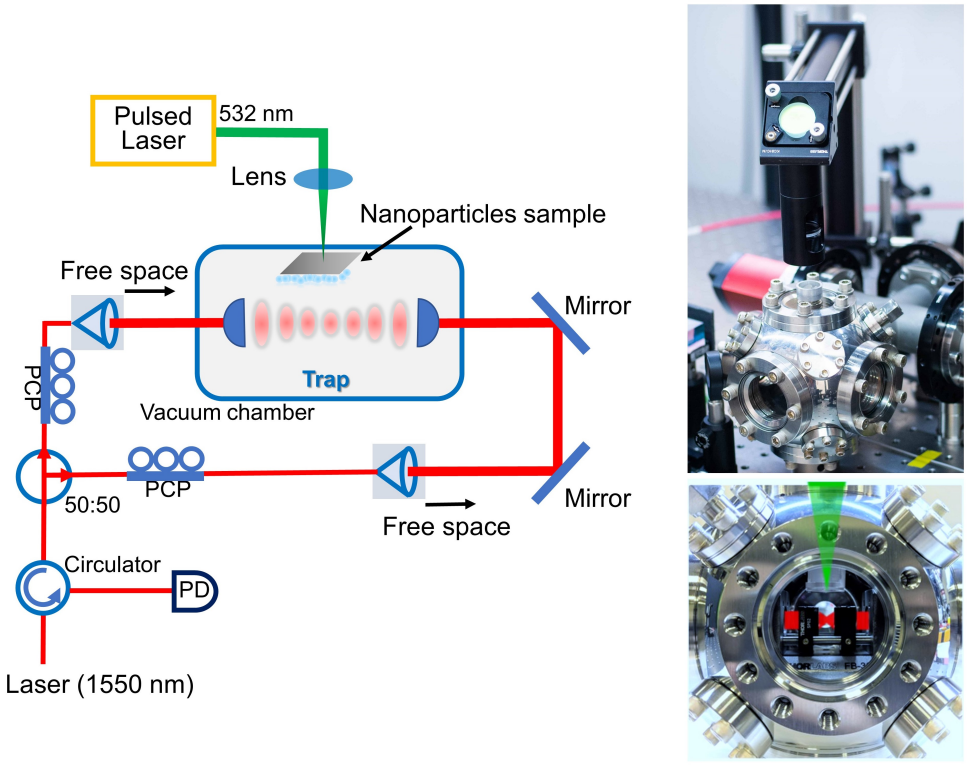

Figure 3.6: Optical setup for LIAD and related trapping and detection systems. Nanoparticles are trapped in a counter-propagating standing wave trap formed by two beams of equal power and the same linear polarisation, at the wavelength of 1550 nm. The optical trap is formed using aspheric lenses with NA = 0.43. Unless otherwise stated, the total optical power in the trap is 200 mW. The particles are launched downwards using LIAD from a substrate located about 8 mm above the optical trap. The particle's motion is encoded in the light, which travels back through the optical system and is directed to a photodetector (PD) by an optical circulator. Polarisation controlling paddles (PCPs) are used to modify the polarisation of the light. The right column presents photos of the optical setup.

As shown in Figure 3.6, the pulsed laser beam (Litron Lasers NANO-S 120-20) is focused by a plano-convex lens with a focal length of about 100 cm (LA1608-A, Thorlabs) onto the backside of the aluminium substrate to create an acoustic shock, causing a release of the nanoparticles via LIAD. The pulsed laser has a wavelength of 532 nm, and a pulse length of $\sim$ 4.6 ns, and we typically operate it in single-shot mode with a peak intensity of $\sim$ 588 GW/cm^2. The waist of the pulsed laser spot focus on the backside of the substrate is estimated to $\sim$ 17 μm.

The front side of the sample substrate is placed to face the optical trap, such

that nanoparticles are launched towards the optical trap, well directed along the Poynting vector of the pulsed laser. It is worth noting that precise alignment of the launch laser relative to the optical trap centre is vital. This is achieved by strictly ensuring the launch laser propagates normally to the horizontal surface of the optical bench. The optical trap is located at the centre of the vacuum chamber, thus alignment of the optical spot of the launch laser through the centre of the top viewport of the vacuum chamber is sufficient to ensure relatively good overlap. In addition, the intensity profile of the focused launch laser beam is not uniform, the launch area with enough energy to desorb nanoparticles from the substrate is typically smaller than the area described by the beam waist. Figure 3.5 (c) and (d) present scanning electron micrograph (SEM) images of an aluminium substrate coated by silica nanospheres and silicon wafer grown with silicon nanorods before and after several rounds of LIAD launch. This also implies the ability to even launch single particles from a very localized region via LIAD.

3.4 Experimental results

3.4.1 Nanoparticle velocity distribution

As discussed in the previous Section 3.2, the launched nanospheres have a velocity distribution. We measured their arrival time at the optical trap and estimated their corresponding velocities. The result is shown in Figure 3.7. The particles are launched using laser pulses with a peak intensity of 588 GW/cm^2, and we calculate the average velocity over the observed timescales of the particle passing through the trap.

Due to the finite transit time of the particles from launch until observation, the gas pressure plays a significant role in determining the velocity distribution at the optical trap. By working at a low pressure of 2.5×10^{-7} mbar (where it is impossible to directly load into the trap) the mean free path of the nanoparticle between collisions with gas molecules is much longer than the transit path. Hence, the velocity distribution at the optical trap, as presented in Figure 3.7 (a), can be considered an accurate representation of the initial launch velocity distribution.

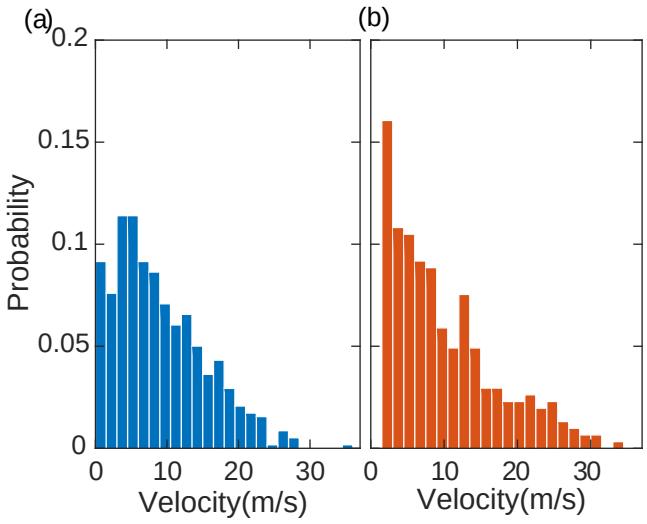

Figure 3.7: Velocity distributions at the position of the optical trap for 300 nm diameter silica nanospheres launched from a 400 μm thick aluminium sheet under the pressure of (a) 2.5×10^{-7} mbar and (b) 1.2×10^{-1} mbar. Histograms are reconstructed from over 120 events for each pressure.

However, the nanoparticles experience thousands of collisions with gas molecules before reaching the trap region at a higher pressure of 1.2×10^{-1} mbar. This heavily lowers their mean velocity, as presented in Figure 3.7 (b), and also removes the slowest particles because they have a large diffusion in the transverse direction and never reach the trap region.

3.4.2 Identifying trapping events

In the experiments, it is normally required to only trap a single nanoparticle. In this section, we describe the optimal conditions for achieving this. We divided the trapping events into three categories: single particle trapping, single cluster trapping, and multiple separated particle or cluster trapping. Trapping events cause a sudden change in our detected signal amplitude due to the amount of light scattering, and particle motion can be subsequently tracked.

Figure 3.8 (a) shows a histogram of the signal amplitude change in response to a trapping event, reconstructed from over 800 events. We observe a peak corresponding to trapping single particles and a long tail corresponding to clusters or multiple particles. The width of the single-particle peak is due to the variability in the exact trapping location within the optical standing wave; hence, we do not

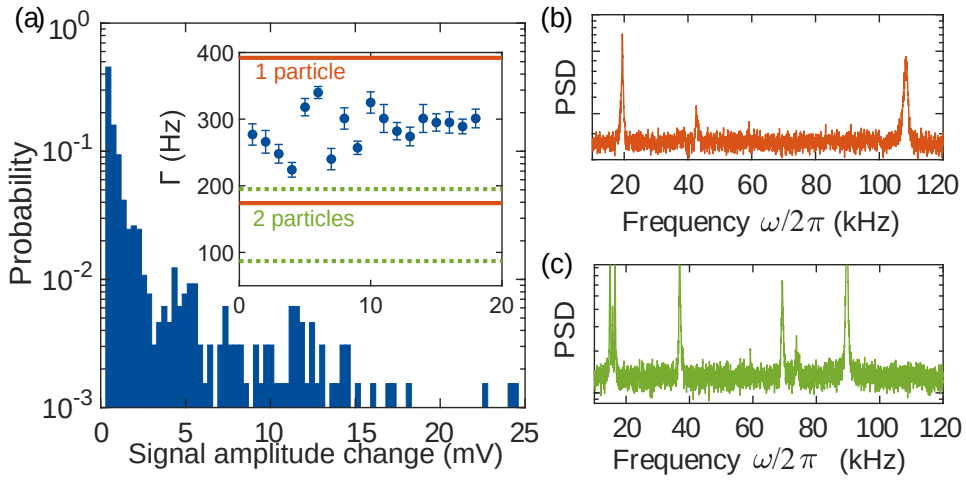

Figure 3.8: Identifying and characterizing trapping events. (a) Histogram of the signal change due to the trapping events with a bin width of 0.3 mV. Trapping a particle changes the signal amplitude for the minimum amount of 0.3 mV. The majority of trapped particles cause a signal change between 0.3 and 0.6 mV, with a long tail due to clusters and multiple trapped particles. The inset shows the extracted momentum damping rate Γ for a set of experiments where the signal change is between 0.3 and 0.6 mV, which is compatible with the theoretical predictions for a single particle. Solid red lines define the upper and lower limits of the theoretical prediction for a single particle, and dotted green lines define the upper and lower limits of the theoretical prediction for a pair of particles. (b) The Power Spectral Density (PSD) of the centre-of-mass motion of a single particle or cluster. (c) The PSD corresponds to multiple trapped particles.

sharply and distinctly resolve integer numbers of trapped particles.

The signal can be analysed to reconstruct the power spectral density (PSD) of trapped particle motion (Figure 3.8 (b)) yielding frequencies corresponding to centre-of-mass motion. Trapping multiple particles yields a more complex PSD with multiple oscillation peaks, as shown in Figure 3.8 (c). The PSD of the motion of a single particle looks very similar to the one obtained by a cluster in Figure 3.8 (a). To identify trapping events corresponding to single trapped particles from clusters, we extract the centre-of-mass momentum damping rates, Γ_{CM} [117]. The damping rate depends on both the gas pressure and the size of the particle.

We randomly analysed experiments with the signal amplitude change that we attribute to a single particle at the pressure of 1 mbar and extracted the damping rate, as shown in the inset of Figure 3.8 (a). These values are in good agreement with the theoretical predictions. There is very large uncertainty on the

theoretical predictions that arise from the uncertainty in the pressure measurement (∼20%) and the particle size (∼10%). We do not aim to carefully distinguish single particles in this study, though this could be verified using other methods [118].

3.4.3 Trapping efficiency with pressure

This LIAD technique is highly efficient across a wide range of pressures, as shown in Figure 3.9 (a). Once particles are released from the substrate via LIAD, they travel towards the trap region in a direction defined by the Poynting vector of the launch laser, continuously losing energy through collisions with gas molecules. Eventually, they slow to their terminal velocity, at which point they fall under gravity and diffuse.

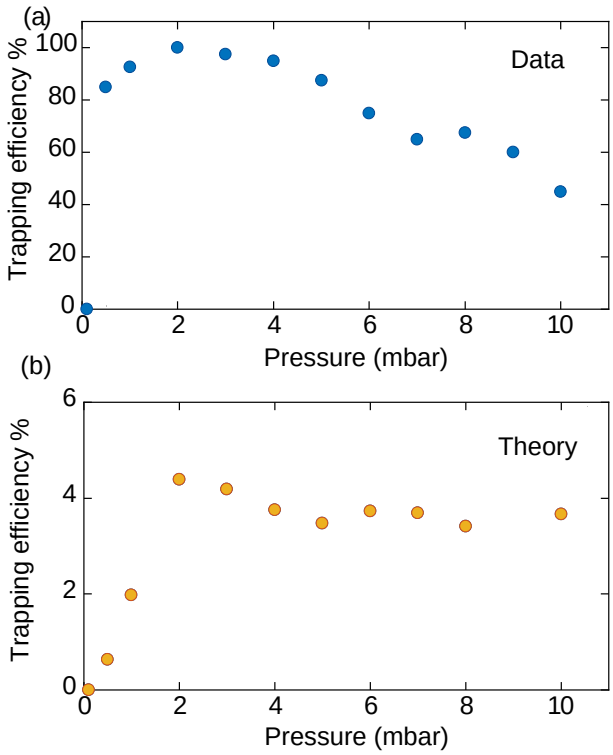

Figure 3.9: Dependence of the loading efficiency upon pressure. (a) The probability of trapping events as a function of residual gas pressure with a launch laser intensity of 588 GW/cm^2. Each data point represents 20 LIAD pulses. (b) Theoretical simulation of optical trap loading. Each point represents 10,000 launching events. Experimentally, multiple particles are launched per shot, explaining the higher efficiency compared with when theoretically predicted. The experimental result shows the same optimal pressure at about 2 mbar as the theory predicted.

By constructing a stochastic simulation of a particle launched toward an optical potential described in previous Section 3.2.2, we model the efficiency of our trap loading process, as shown in Figure 3.9 (b). When the pressure is too low, the particles pass through the trap region without slowing down and are unable to get trapped, leading to a pressure threshold in terms of the minimum trapping pressure. Above this threshold pressure, particles can reach the trapping region by diffusion, and the trapping probability levels off. Under these conditions, the particles may take many hundreds of seconds to be trapped.

The experimental data with different pressures is shown in Figure 3.9 (a). We can see that the trapping efficiency decreases with increasing pressure, which we believe is probably due to experimental runs being terminated too early before the hundreds of seconds it can take for trapping to occur. The overall trapping efficiency in the experiments is much higher than in the simulation. This is because multiple particles are launched at the same time increasing the trapping efficiency. Including the velocity distribution in the directions orthogonal to gravity, which we have not measured, would further improve the accuracy of the simulation model. However, we can see that the optimally efficient pressure is accurately predicted.

3.4.4 Launch laser intensity

The effect of the launch laser intensity on the LIAD process is very complex and, surprisingly, does not significantly alter the launch velocity above a minimum threshold, as discussed in [116]. However, the launch laser intensity strongly affects the number of particles launched per shot and the effective area from which the particles are launched, as shown in Figure 3.10. Each colour bar represents a different launch laser intensity with about 980, 588, 196 GW/cm^2. The solid bars in the histogram represent single particle trapping events, and the empty bars represent the trapping of clusters or multiple particles. When the intensity is low (196 GW/cm^2), the trapping efficiency drops due to fewer particles being desorbed from the substrate. For higher launch intensities, the overall trapping probability is not significantly increased, but the chance of trapping multiple particles increases.

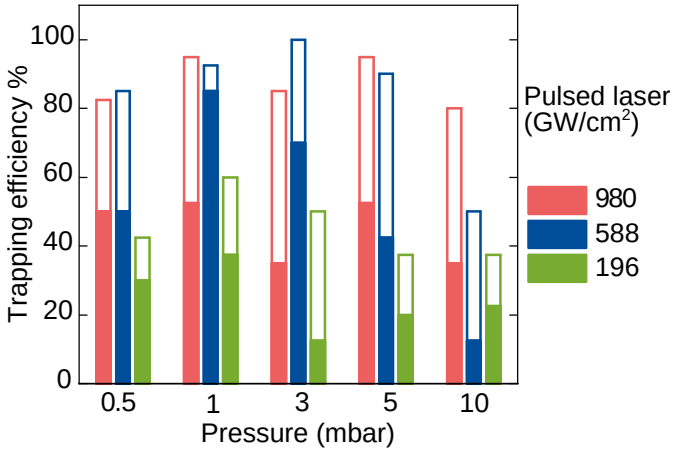

Figure 3.10: Effects of the launch laser intensity and pressure on the efficiency of trapping single particles. Solid bars represent single trapped particles, and empty bars represent clusters or multiple particles, as identified using the methods described above in Figure 3.8. Lower launch laser intensities yield fewer particles, whereas higher intensities lead to multiple trapping events per shot. Each bar represents 40 LIAD pulses.

3.4.5 Optimal optical trap depth

The optical trap is formed by two counter-propagating tightly focused laser beams, as described above. We choose a counter-propagating trap over a single-beam trap to create a larger trapping volume to maximize the probability of the particle trapping. Figure 3.11 shows the effect of optical trap power over the trapping efficiency. The optical trap must be at least deep enough to confine a particle in thermal equilibrium with the environment, and realistically it must be significantly deeper due to thermal fluctuations, yielding a threshold of minimum trap power required to capture a particle. In our experiment, we were able to trap with optical powers as low as $\sim$ 10 mW. Also, for higher pressures, the optical power can be even lower with the assistance of the additional dissipation provided by gas.

From Figure 3.11, we also observe that the trapping efficiency dropped at high optical trap power, which we attribute to particle heating as a result of the absorption of trapping light by impurities in the material, which is further supported by the increased stability at higher pressures where residual gas can cool particles through faster collisions [103]. Another reason for the reduced trapping efficiency is due to the heating from the laser phase noise at high powers [119].

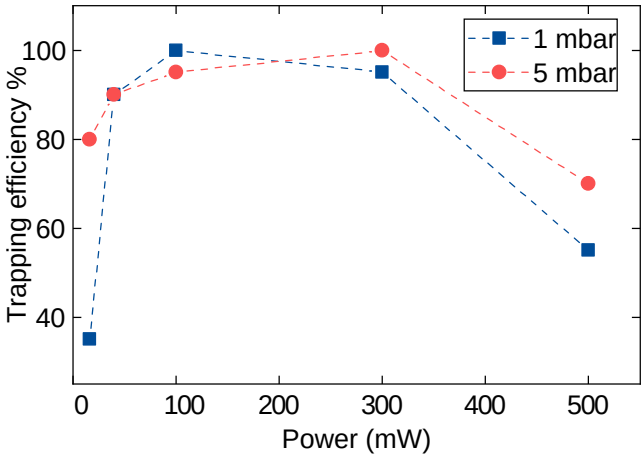

Figure 3.11: Effects of the optical trap power on trapping efficiency for two different pressures. The optical trap power must be high enough to be able to confine a particle that is in thermal equilibrium with the environment. Each data point represents 40 LIAD pulses.

3.5 Summary and discussion

This chapter presents a clean, dry, and efficient method for directly loading nanoparticles into optical traps using LIAD. There is an optimal pressure at which the traps can be loaded, which depends on the size of the particle and the distance between the sample and the trap. The optimal spacing between the sample and the trap, in terms of loading efficiency for a given pressure, depends on the exact initial velocity distribution and the size of launched particles.

Unless the exact loading pressure is critical, any separation below 10 mm is adequate for efficient loading. By tuning the launch laser intensity, the probability of trapping single particles could be enhanced. Around the optimal pressure, the particle motion is near ballistic, and trapping occurred in a few milliseconds, and at higher pressures, particles diffused into the trapping region. We are also able to launch particles from localized regions of a sample, thus, enabling the launch and trapping of sparse particles.

We note that Bykov *et al.* [111] developed a technique combining LIAD and the temporal control of a Paul trap potential to launch and capture charged nanoparticles directly under ultrahigh vacuum (UHV) conditions. This technique does not require a dissipation mechanism, since the potential is turned on when

the particle is at the centre of the trap, at which point, it does not have enough energy to escape. However, since, in general, optical potentials are much less deep than those in a Paul trap, direct UHV loading into an optical trap would only work for nanoparticles with velocities $<< 0.1$ ms^{-1}, requiring the development of new soft-launching techniques [120].

Chapter 4

Rotational Control of a Levitated Nanomechanical Rotor

4.1 Introduction

While optical trapping relies on the transfer of linear momentum from the light field to nanoparticles, the rotational dynamics of trapped nanoparticles can be introduced via the transfer of angular momentum carried by light in the way of spin angular momentum associated with circularly polarised light or orbital angular momentum within the structured light.

With circularly polarised light, electrically levitated graphene has been rotated in excess of 50 MHz rotation rates [121], and optically levitated silica nanospheres [60, 61] and nanodumbells can be rotated up to the order of magnitude of GHz in high vacuum [54, 55, 63]. Silicon nanorods also have been optically driven to $\sim$ 1 MHz at about 1 mbar [53], and frequency locked to an external clock at MHz rotation rate which demonstrated ultra-stable frequency stability of 1 part in 7.7×10^{11} [62]. Besides, the spin angular momentum of light can be transferred to birefringent particles due to its material-induced optical inhomogeneity in all spatial directions of crystals [45], for example, sub-micron diameter Vaterite spheres have been reported to rotate at $\sim$10 MHz and exhibit gyroscopic effects [57, 58]. Spatially inhomogeneous optical fields with orbital angular momentum (OAM) are an alternative way to transfer another kind of angular momentum to

levitated nanoparticles. It has the advantage of transferring no limit of quanta $\hbar k_0$ of angular momentum, since each photon can carry more than one quanta, referred to as the topological charge. With OAM trapping light, the motion of levitated nanoparticles becomes more complex, including spinning, orbit, and spin-orbit interactions [51]. The rotation rate can be increased by increasing the topological charge carried by the light beam. This has only recently been explored for levitated nanoparticles in vacuum [122, 123, 124].

These fast rotating nanomechanical rotors have been proposed to detect the fluctuation-induced quantum friction by rotating a sphere above a surface [65, 63], and vacuum friction using a neutral rotating particle which is predicted to dissipate energy through the emission of radiation at the rotational frequency [125, 64]. Moreover, the largely unexplored rotational quantum phenomena provide great opportunities for quantum superposition experiments by involving more degrees of freedom and promising sensing applications [44].

The approaches to manipulating and controlling the rotational degrees of freedom of levitated nanomechanical rotors are the crucial prerequisite for the exploitation of the angular momentum states in the quantum regime. In this chapter, we first discuss the full rotations with different controlling strategies, before presenting techniques to cool their mechanical rotation into the quantum regime in the next chapter.

4.2 Rotation driven by circularly polarised light

4.2.1 Optical torque and rotational damping rate

For anisotropic nanoparticles, the light-matter interactions are more complicated, which manifests the orientational dependence of the object relative to the polarisation direction of the light field. The optical torque experienced by the nanoparticle is:

$$\mathbf{N}_{\text{opt}} = \langle \mathbf{P} \times \mathbf{E}^* \rangle \,, \tag{4.1}$$

where $\mathbf{P} = \alpha_0 \mathbf{E}$ is the induced polarisation.

When the trapping light is circularly polarised, the radiation pressure of the

laser exerts a torque on the polarisation plane (here is α direction) can be expressed [71, 53]:

$$N_\alpha = \frac{\Delta\chi l^2 d^4 k^3}{48 c \mathrm{w}_0^2} \left[\Delta\chi \eta_1(kl) + \chi_\perp \eta_2(kl)\right] P_{\mathrm{opt}}, \tag{4.2}$$

where $\Delta\chi$ is the susceptibility anisotropy, l and d are the length and diameter of nanorods, and $\eta_{1,2}(kl)$ are two correction terms given by:

$$\begin{aligned} \eta_1(kl) &= \frac{3}{4}\int_{-1}^{1} (1-\xi^2)\sin^2\left(\frac{kl\xi}{2}\right) \mathrm{d}\xi, \\ \eta_2(kl) &= \frac{3}{8}\int_{-1}^{1} (1-3\xi^2)\sin^2\left(\frac{kl\xi}{2}\right) \mathrm{d}\xi, \end{aligned} \tag{4.3}$$

where $\eta_1 \simeq 1$ and $\eta_2 \simeq 0$ for short nanorods with $kl \ll 1$ in the generalized Rayleigh-Gans approximation [53].

Intuitively, in contrast to linearly polarised light, the polarisation direction of circularly polarised light rotates at the optical frequency, which is too fast for the nanoparticle to follow. The maximum rotational frequency ω_{rot} is given by the balance between the optical driven torque N_{opt} from the light field and the damping from the collisions with residual gas molecules Γ_{rot}:

$$\omega_{\mathrm{rot}}^{\mathrm{max}} = \frac{N_{\mathrm{opt}}}{I\Gamma_{\mathrm{rot}}}, \tag{4.4}$$

where the rotational damping rate Γ_{rot} for diffuse reflection of gas molecules in the free molecular regime for a nanorod (i.e., the mean free path of the gas molecules exceeds the diameter of the nanorod) is given by [53]:

$$\Gamma_{\mathrm{rot,rod}} = \frac{dlP_{\mathrm{gas}}}{2M}\sqrt{\frac{2\pi m_{\mathrm{gas}}}{k_{\mathrm{B}} T_{\mathrm{gas}}}}\left(\frac{3}{2}+\frac{\pi}{4}\right), \tag{4.5}$$

and the moment of inertia for a nanorod along its longest axis with the length of l is:

$$I_{\mathrm{rod}} = \frac{Ml^2}{12}. \tag{4.6}$$

4.2.2 Rotational dynamics of levitated nanorods

Compared to the translational motion or harmonically bound motion, the rotational motion is fundamentally different, showing nonlinear dynamics. The corresponding equation of motion for describing the dynamics of the levitated nanorotor can be written as:

$$\dot{\omega}_{\mathrm{rot}} + \Gamma_{\mathrm{rot}}\omega_{\mathrm{rot}} = \frac{1}{I}N_{\mathrm{opt}}, \tag{4.7}$$

where the total optical torque N_{opt} is the sum of three contributions from photon absorption N_{abs}, birefringence N_{brf} and shape-induced asymmetry N_{shape} [54]. The torque contribution from photon absorption is:

$$N_{\mathrm{abs}} = \frac{I\lambda}{2\pi c}\sigma_{\mathrm{abs}}\Delta s_{\mathrm{abs}}, \tag{4.8}$$

where σ_{abs} is the absorption cross-section of the nanoparticle, and $\Delta s_{\mathrm{abs}} \in [-1, +1]$ denotes the degree of circular polarisation with -1 for completely left circularly polarised light and $+1$ for completely right circularly polarised light. The torque originating from birefringence N_{brf} is according to the material properties of the particle, which is very small for silica nanospheres and silicon nanorods in our experiments. The shaped-induced torque N_{shape} resulted from the shape asymmetry, leading to a susceptibility anisotropy. All the contributions are proportional to the intensity of the trapping light I_{opt}. As discussed in the previous section, we operate the experiments in the free molecular regime, where the levitated nanorotor rotates continuously at a rotational frequency $\omega_{\mathrm{opt}} \propto N_{\mathrm{opt}}/P_{\mathrm{gas}}$, and reaching the maximum rate shown in Equation (4.4).

Figure 4.1 shows the 0.1 ms duration time trace of a levitated silicon nanorod (600 nm long and 120 nm diameter) in the linearly polarised (top panel) and circularly polarised (bottom panel) polarised light under the pressure of 10 mbar. The polarisation states in each arm are set as the same and the laser power in total is about 1.36 W. We use the MMF detection and polarisation measurement techniques to detect the full rotations of a rotating nanorod in the experimental system (see details in Section 2.4).

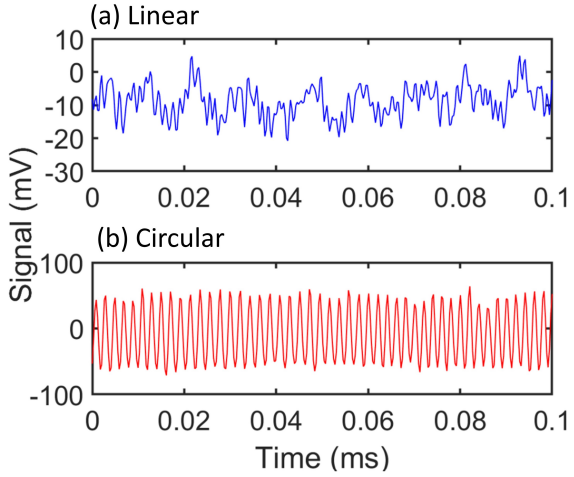

Figure 4.1: The time trace of dynamics of levitated silicon nanorod with different polarisation states of trapping light: linearly polarised at the top panel (blue) and circularly polarised at the bottom panel (red). These are detected by the scattered light via MMF detection with a duration of 0.1 ms. The pressure is 10 mbar and the total power of the trapping light is ~ 1.36 W with a pair of focusing lenses of NA=0.3.

By converting the time trace to the frequency domain of the angular velocity based on the Fourier transform, the PSD spectrum of rotational dynamics of levitated nanorotor becomes:

$$\begin{aligned} S_{\mathrm{rot}}(\omega) &= \int_{-\infty}^{\infty} \langle \omega_{\mathrm{rot}}(t)\omega_{\mathrm{rot}}(t-t')e^{-i\omega t}\mathrm{d}t' \\ &= \frac{2\Gamma_{\mathrm{rot}}k_{\mathrm{B}}T_b}{I(\omega^2+\Gamma_{\mathrm{rot}}^2)}. \end{aligned} \tag{4.9}$$

As shown in Figure 4.2 of the PSD converted from the time trace in Figure 4.1, we can measure the translational frequencies in z-direction $f_z \simeq 85$ kHz, and librational frequency in α-direction $f_\alpha \simeq 110$ kHz, and their second harmonics $2f_z$ and $2f_\alpha$, with the linearly polarised light. The reason why the fundamental frequency signals (i.e., f_z and f_α) appear is due to the misalignment of the detection fibre and the optical trap. When the polarisation state of the trapping light switches to completely circular with the opposite handedness in each arm, the levitated nanorod starts to rotate, as shown in the bottom panel of Figure 4.1 and its PSD spectrum in Figure 4.2. The librational mode f_α vanishes compared to linearly polarised light, and the translational frequencies (e.g., f_z) also

decrease due to the decrease of the potential with a circularly polarised light field. The width of the peak at $2f_{\mathrm{rot}}$ is relatively broad, arising from the instability of rotational frequency gas at a relatively long time scale. It can be locked to an external clock for obtaining an extremely narrow linewidth [62]. The signals in x, y-direction do not appear clearly in the PSD due to their relatively low frequencies (about 1 kHz) and the signal-to-noise ratio (SNR) is necessarily further improved especially in the low-frequency range.

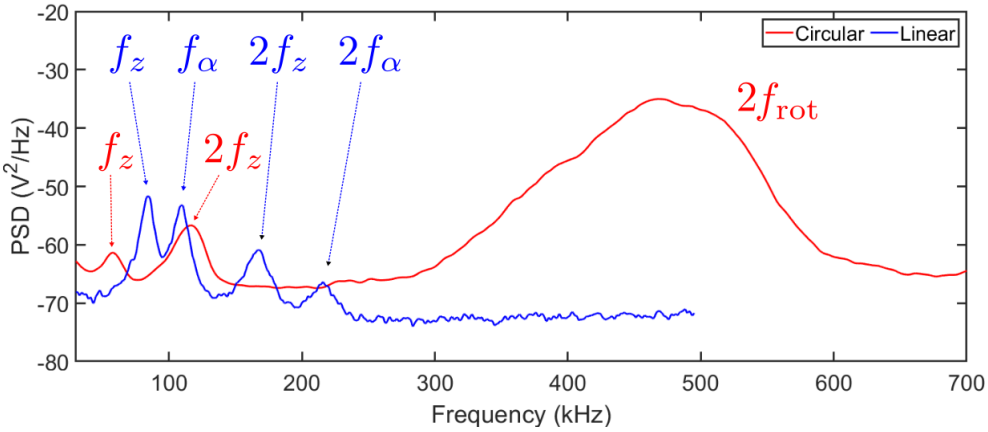

Figure 4.2: The PSD spectrum of a levitated silicon nanorod (600 nm long and 100 nm diameter) in linearly (blue) and circularly (red) polarised light at about 10 mbar. With linearly polarised trapping light, the PSD exhibits the librational mode f_α; while it vanishes with circularly polarised light, replaced by a broad rotational peak $2f_{\mathrm{rot}}$.

4.2.3 Power and pressure dependence

The rotation rate of levitated nanorotors is determined by the balance between the optical-driven torque and the damping from the surrounding gas molecules. For higher optical power, more photons carrying angular momenta can be transferred to the nanorotor via light-matter interactions, yielding the optical driven torque N_{opt} proportional to the laser power P_{opt} described by Equation (4.2).

Figure 4.3 shows the linear dependence of the rotation rate of a levitated nanorod on the optical power as theoretically predicted under the pressure of about 10 mbar. Compared to the rotation speed of silica nanospheres or nanodumbells [54, 55, 61], the silicon nanorod can experience larger torque with the

equivalent volume under the same optical power and pressure, which is caused by the higher geometry-induced susceptibility.

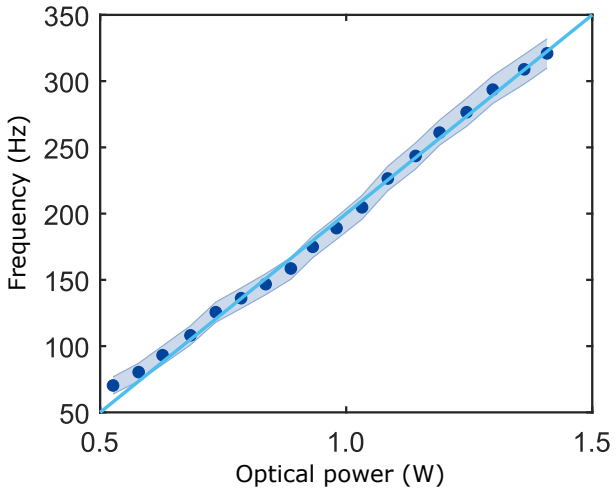

Figure 4.3: The rotation frequency of a levitated nanorod (600 nm long, 120 nm diameter) linearly scales with the optical power ranging from 0.5 W to 1.5 W as theoretically predicted. The pressure is about 10 mbar. The blue dots denote the average value of measured data. The shade areas represent the full range of the rotational frequency.

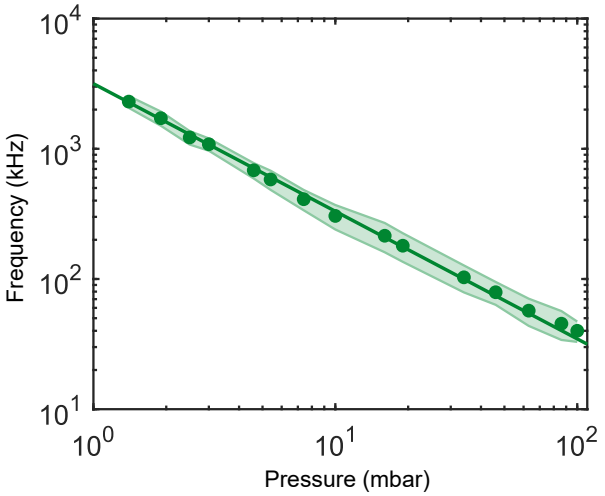

Figure 4.4: The rotation frequency of a levitated nanorod (600 nm long, 120 nm diameter) inversely linearly scales with the gas pressure increasing from 1 mbar to 100 mbar. The optical power is approximately 1.2 W. The green dots represent the average value of measured rotational frequency data and the shade areas show its full frequency range.

In terms of pressure dependence, rotational damping is also approximately linearly dependent on gas pressure shown in Equation (4.5), which further imprints a linear response on the rotation speed of a levitated nanorotor. Figure 4.4 shows the rotational frequency of a levitated silicon nanorod linearly increases with the linear decrease of pressure from 100 mbar to 1 mbar.

Driven by circularly polarised light, the levitated nanorotor has great potential for developing torque sensing and pressure sensing applications, especially benefiting from its linear response [63, 62].

4.3 Rotation with transverse orbit angular momentum

Optical angular momentum itself can also manifest in the form of OAM. Different to spin angular angular momentum (SAM) originating from the rotation of the electromagnetic field vector, OAM is the direct analogue of the classical angular momentum defined by $\mathbf{L} = \mathbf{r} \times \mathbf{P}$, where $\mathbf{r}$ is the displacement from the coordinate origin and $\mathbf{P}$ is the optical linear momentum density [126]. OAM seems, by definition, to be dependent on the choice of the coordinate system, and so can be called *extrinsic*. However, *intrinsic* (coordinate-independent) OAM can be obtained when the integral of the OAM density over space yields a non-zero value regardless of the coordinates chosen. This is the case in optical vortex beams, which exhibit OAM through their wavefronts spiralling around a phase singularity [127, 128, 129]. For paraxial light beams, the intrinsic OAM is *longitudinal* since $\mathbf{L}$ is parallel to the beam's propagation direction. It is also possible to engineer *transverse* SAM, via evanescent waves [130, 131], focused beams [132] and multiple wave interference patterns [133]. Transverse orbital angular momentum (TOAM) is rarely observed, unless we are considering polychromatic fields [134, 135, 136] or extrinsic momentum when a beam propagates away from the coordinate origin [137, 138]. *Intrinsic* TOAM in monochromatic fields, appearing as intricate transverse phase singularity vortex lines, has been proposed in superimposed co-propagating beams with different beam-widths and/or amplitudes

[139, 140, 141].

In this section, we create an optical angular momentum structure using two monochromatic offset counter-propagating beams, which carries both transverse SAM and intrinsic TOAM and demonstrate the measurement of intrinsic TOAM. The light field contains a robust array of synthesised transverse optical vortices. We verify and probe the optical angular momentum structure using a levitated nanoparticle optomechanical sensor [7], and demonstrate the tuneable nature of the induced torque.

The rotation of levitated nanoparticles via *longitudinal* SAM from circularly polarised light has recently been the focus of several studies [63, 61, 62]. In this work, we produce a torque five orders of magnitude larger than previously demonstrated, driving MHz rotation at 10 mbar of background gas pressure. The rotation of levitated particles has applications in torque sensing [63, 62], studies of vacuum friction [65, 125] and the exploration of macroscopic quantum physics [44, 88]. The orbit of nanospheres via longitudinal OAM has been studied [123], and the presence of transverse SAM in focused circularly polarised light incident upon a microparticle has been inferred [142].

This work presents a straightforward and robust method for generating intrinsic TOAM, the use of levitated nanoparticles as sensitive probes of structured light fields, and the first manipulation of particle motion using TOAM. The ability to fully control the alignment and rotation of nanoparticles levitated in vacuum is of great importance for cavity optomechanics [73], alignment of targets in high-energy beam experiments and quantum control at the nanoscale [44].

4.3.1 Origin of transverse orbit angular momentum

We consider an illumination geometry consisting of two counter-propagating Gaussian beams with the same optical frequency ν and both linearly polarised in the y-direction, as illustrated in Figure 4.5. The waist plane of each beam is located at $z = 0$, and the positions of their axes are $(0, \pm\delta, 0)$.

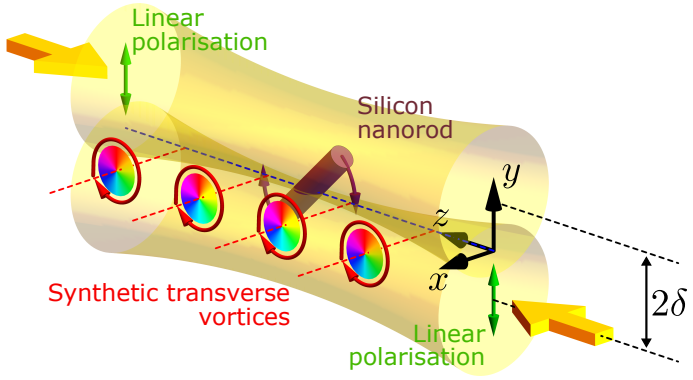

Figure 4.5: Generation of structured transverse orbital angular momentum. When two focused counter-propagating linearly polarised Gaussian beams are separated along the polarisation axis, an array of optical vortices is generated, carrying angular momentum which is transverse to the propagation direction. A silicon nanorod is suspended within the structure, generating a torque, and driving rotation in the y-z plane.

Assuming the time-dependence factor $e^{-i\nu t}$, one may analytically express the transverse electric and magnetic fields as:

$$\begin{aligned} E_y &= u(x, y+\delta, z)e^{ikz} + u(x, y-\delta, -z)e^{-ikz}, \\ B_x &= -\frac{1}{c}u(x, y+\delta, z)e^{ikz} + \frac{1}{c}u(x, y-\delta, -z)e^{-ikz}, \end{aligned} \tag{4.10}$$

where

$$u(x, y, z) = E_0 \frac{w_0}{w(z)} e^{-i\varphi(z)} e^{ik(x^2+y^2)/[2q(z)]}, \tag{4.11}$$

is the Gaussian beam solution to the scalar Helmholtz equation in the slow-varying approximation [143]. Here, E_0 is a constant field amplitude, $w_0 = w(z=0)$ is the beam waist radius, $q(z) = z - iz_0$ and $\varphi(z) = \tan^{-1}(z/z_0)$ the Gouy phase, with $z_0 = \pi w_0^2/\lambda$ being the Rayleigh range.

It follows from Equation (4.10) that the phases of the electric and magnetic field, ϕ_e and ϕ_m, satisfies:

$$\begin{aligned} \tan\phi_e &= \frac{\Im(E_y)}{\Re(E_y)} = \frac{C(x, y-\delta, z) - C(x, y+\delta, z)}{D(x, y-\delta, z) + D(x, y+\delta, z)}, \\ \tan\phi_m &= \frac{\Im(B_x)}{\Re(B_x)} = \frac{C(x, y-\delta, z) + C(x, y+\delta, z)}{D(x, y-\delta, z) - D(x, y+\delta, z)}, \end{aligned} \tag{4.12}$$

where

$$\begin{aligned} C(x,y,z) &= e^{-kr^2 z_0/(z^2+z_0^2)} \sin\left[\frac{kr^2 z}{z^2+z_0^2} - \varphi(z) + kz\right], \\ D(x,y,z) &= e^{-kr^2 z_0/(z^2+z_0^2)} \cos\left[\frac{kr^2 z}{z^2+z_0^2} - \varphi(z) + kz\right], \end{aligned} \tag{4.13}$$

with $r^2 = x^2 + y^2$. For $\delta = 0$, ϕ_e and ϕ_m are constant, and thus the phase profile will be planar. This is the expected result for a standing wave.

The appearance of a phase singularity or dislocation, which is the physical origin of phase vortices, requires $\delta \neq 0$, and

$$\Im(E_y) = \Re(E_y) = 0, \tag{4.14}$$

(for electric field singularities) or

$$\Im(B_x) = \Re(B_x) = 0, \tag{4.15}$$

(for magnetic field singularities) [144].

It can be proven that the intersection lines of $y = 0$ and

$$\frac{k(x^2+\delta^2)z}{z^2+z_0^2} - \varphi(z) + kz = \frac{n\pi}{2}, \tag{4.16}$$

are the solutions to Equation (4.14) for odd n and to Equation (4.15) when n is even.

Figure 4.6 illustrates the calculated field characteristics for a beam offset $2\delta = 1.0$ μm; the wavelength and waist radius are set to $\lambda = 1550$ nm and $w_0 = 1.0$ μm, corresponding to beams focused with numerical aperture NA = 0.6. Both the electric and magnetic fields exhibit an intensity profile typical of standing waves: the positions of the electric field nodes (Figure 4.6(a)) coincide with those of the magnetic field antinodes (Figure 4.6(b)). The lines passing through the planes represent the location of the phase dislocations, namely, the solutions to Equation (4.16) for $-6 \leq n \leq 6$. They stretch transversely along the x-direction, and pass through the nodes of the electric and magnetic fields for odd and even

n, respectively. The red and blue solid circles mark the position of electric and magnetic field vortices.

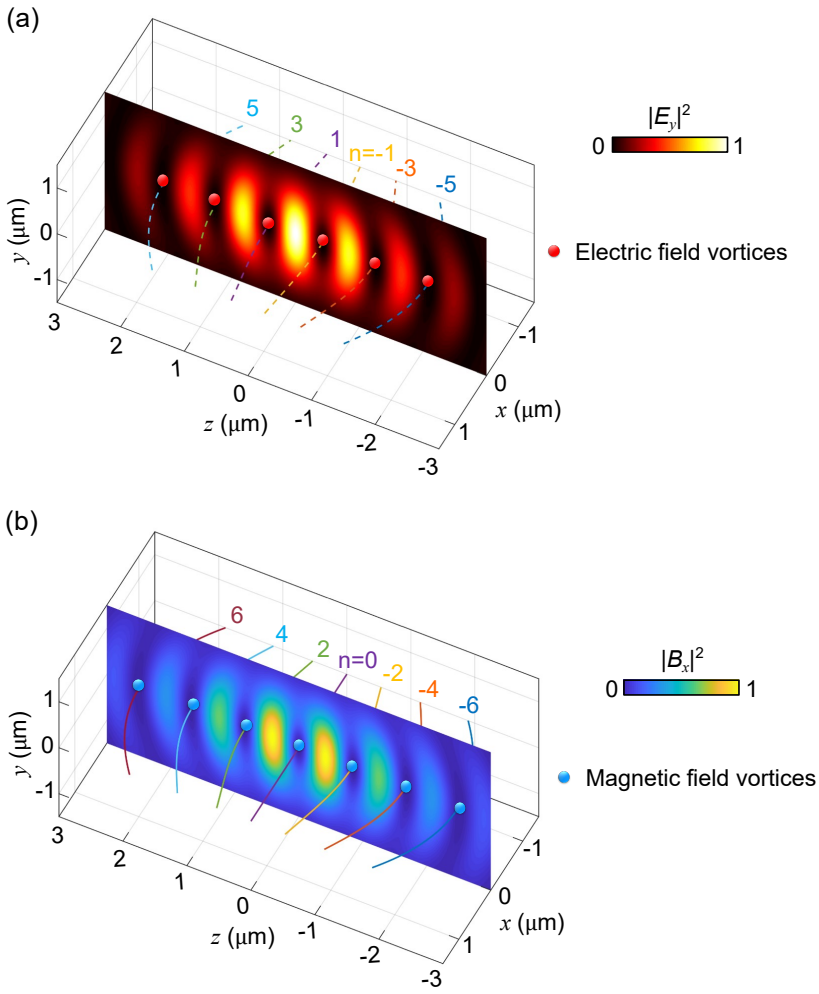

Figure 4.6: Intensity profiles of the electric (a) and magnetic fields (b) in the axial plane. Dashed and solid curves show the phase singularity lines calculated based on Equation (4.16). The red and blue solid circles mark the position of electric and magnetic field vortices, respectively.

From the phase profile shown in Figure 4.7, we can clearly identify the dislocation points for the electric and magnetic fields. For each point, the strength (a.k.a., topological charge) is -1, because the phase increases by 2π in a negative circuit with respect to the $+x$ direction. Therefore, the field carries a net OAM in the $-x$ direction. The black and white arrows show the electric $\mathbf{P}^{\mathrm{e}}$ and magnetic

$\mathbf{P}^{\mathrm{m}}$ parts of the orbital momentum density [126]:

$$\mathbf{P} = \mathbf{P}^{\mathrm{e}} + \mathbf{P}^{\mathrm{m}} = \frac{1}{4\nu}\Im\left[\varepsilon_{\mathbf{0}}\mathbf{E}^{*}\cdot\nabla\mathbf{E} + \frac{\mathbf{1}}{\mu_{\mathbf{0}}}\mathbf{B}^{*}\cdot\nabla\mathbf{B}\right], \tag{4.17}$$

which, together with the position vector $\mathbf{r}$, defines the density of OAM $\mathbf{L} = \mathbf{r} \times \mathbf{P}$.

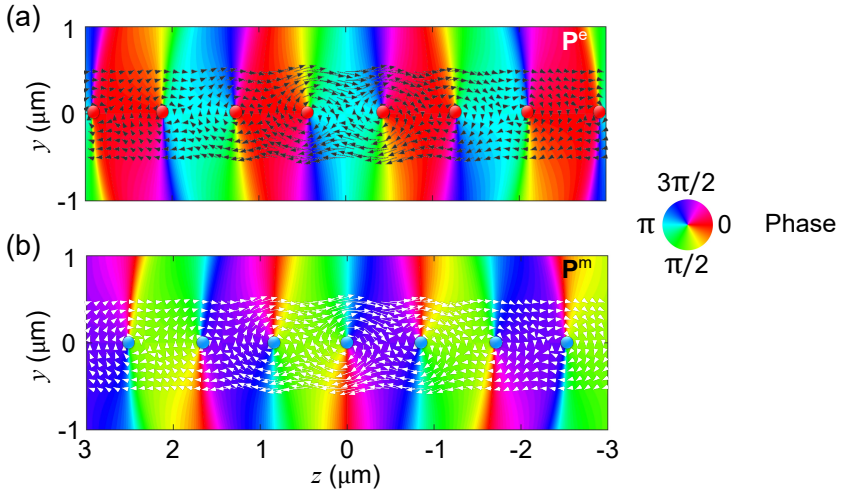

Figure 4.7: Phase singularities and vortices due to electric and magnetic fields. In-plane phase distribution for the transverse electric (a) and magnetic (b) fields. Arrows indicate the magnitude and direction of the electric and magnetic orbital momentum densities, $\mathbf{P}^{\mathrm{e}}$ and $\mathbf{P}^{\mathrm{m}}$, in the vicinity of singularity points.

Around the dislocation points, $\mathbf{P}^{\mathrm{e}}$ and $\mathbf{P}^{\mathrm{m}}$ circulate in the same sense, such that all the phase vortices are of the same handedness. The integral OAM carried by the field, $\langle\mathbf{L}\rangle$, is intrinsic since it is independent of the choice of origin; for a translational transformation of the coordinates $\mathbf{r} \to \mathbf{r} + \mathbf{r}_0$, there is no change since $\langle\mathbf{L}\rangle \to \langle\mathbf{L}\rangle + \mathbf{r}_0 \times \langle\mathbf{P}\rangle = \langle\mathbf{L}\rangle$, where we invoke $\langle\mathbf{P}\rangle = 0$ for the counterpropagating configuration. Each of the Gaussian beams, considered separately, would possess a transverse extrinsic TOAM due to their propagation axis not crossing the origin. However, when taken together, their common centroid lies exactly in the origin, and no extrinsic TOAM exists - instead, an array of transverse vortex lines is synthesized, carrying intrinsic TOAM.

When a single linearly polarised collimated beam is focused, the polarisation at the focus becomes elliptically polarised in the transverse plane because of the

generation of a longitudinal field with a phase difference with respect to the transverse field [145]. This transverse elliptical polarisation corresponds to a transverse spin and is associated with a transverse SAM.

According to Maxwell's equations, the longitudinal fields can be expressed as:

$$\begin{aligned} E_z &= -\frac{ic^2}{\nu}\frac{\partial B_x}{\partial y}, \\ B_z &= -\frac{i}{\nu}\frac{\partial E_y}{\partial x}. \end{aligned} \tag{4.18}$$

These would be negligible in the case of weak focusing; however, in moderate or strong focusing, the coexistence of both longitudinal and transverse fields can give rise to a circular polarisation in a plane transverse to the propagation, namely transverse SAM. The dual-symmetric SAM density of electromagnetic fields read [133]:

$$\mathbf{S} = \mathbf{S}^{\mathrm{e}} + \mathbf{S}^{\mathrm{m}} = \frac{1}{4\nu}\Im\left[\varepsilon_0 \mathbf{E}^* \times \mathbf{E} + \frac{1}{\mu_0}\mathbf{B}^* \times \mathbf{B}\right]. \tag{4.19}$$

In our setup, with the individual beam linear polarisation direction parallel to the direction of beam offset (along y-direction), the spin on the $x = 0$ plane is purely electric and has an x-component only, $S_x = S_x^{\mathrm{e}} \propto \Im(E_y^* E_z)$. The calcu-

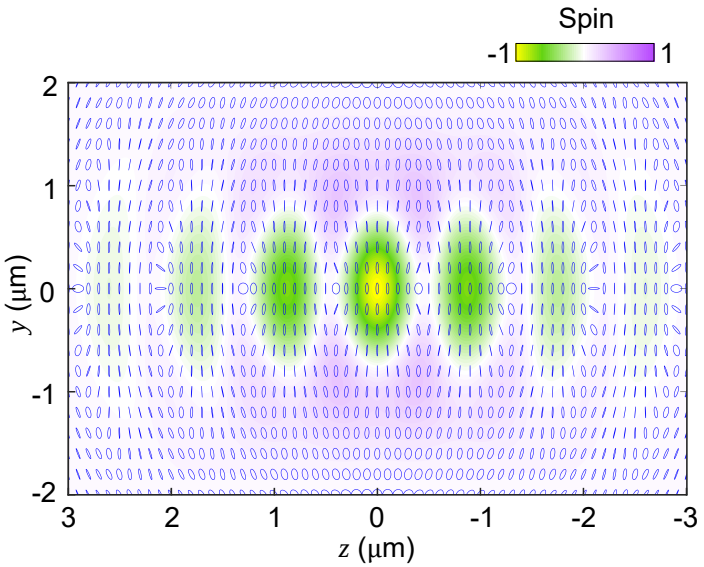

Figure 4.8: Transverse spin S_x and normalized polarisation ellipses indicate that the points of close-to-circular polarisation are near electric field nodes.

lated spin is shown in Figure 4.8, where polarisation states are visualized by the local electric field ellipse. The spin exhibits a magnitude distribution similar to the electric field intensity (Figure 4.6 (a)), with a negative x-component of the spin near the maximum intensity, aligned with the intrinsic TOAM. However, the polarisation tends to be linear at the locations where the spin is significant, with circular polarisation appearing at the field nodes.

4.3.2 Numerical calculation of optical torque

An intuitive description of the torque on the nanorod in this complex structured wave field is not simple, and we resort to modelling the torque using numerical techniques. Newton's second law of motion dictates that any change in linear/angular momentum invokes a force/torque. This principle leads to an induced torque on any particle within an optical field carrying OAM and SAM which we calculate using Maxwell's Stress Tensor (MST) method.

A particle can experience optical forces by either absorbing or scattering light, as accounted for by the Maxwell stress tensor $\overleftrightarrow{\mathbf{T}}$ which represents the overall time-averaged flow of momentum in an electromagnetic field [96, 146]:

$$\overleftrightarrow{\mathbf{T}} = \frac{1}{2}\Re\left\{\varepsilon_0 \mathbf{E}\otimes\mathbf{E}^* + \frac{1}{\mu_0}\mathbf{B}\otimes\mathbf{B}^* - \frac{1}{2}(\varepsilon_0|\mathbf{E}|^2 + \frac{1}{\mu_0}|\mathbf{B}|^2)\overleftrightarrow{\mathbf{I}}\right\}, \tag{4.20}$$

where $\otimes$ corresponds to an outer product, and $\overleftrightarrow{\mathbf{I}}$ is the three-dimensional (3D) identity matrix. This can be extended to electromagnetic angular momentum via a cross product with the spatial coordinates $\mathbf{r}\times\overleftrightarrow{\mathbf{T}}$, and the torque is calculated from the surface integral of a closed surface enclosing the particle [147, 148, 149],

$$\mathbf{N} = \oiint(\mathbf{r}\times\overleftrightarrow{\mathbf{T}})\cdot\hat{\mathbf{n}}\,\mathrm{d}S, \tag{4.21}$$

where $\mathbf{N}$ is the torque, $\mathbf{r}$ is the position vector, and $\hat{\mathbf{n}}$ is the unit vector normal to the surface S.

A calculation of the torque using the MST is a time-consuming process that requires knowing the total electric and magnetic fields incident on, and scattered

by, the nanorod. These fields are calculated numerically as described below. The nanorod was approximated as a cylinder, and the relative permittivity of silicon was assumed to be 12.1.

Normally, the 3D electric and magnetic fields scattering off the nanorod are required for each pixel in the colour plot (e.g., Figure 4.9), with the nanorod placed at different positions within the structured illumination. In order to do this efficiently, a procedure previously implemented in Ref. [150] was followed, in which each beam is decomposed into a collection of plane waves using a spatial Fourier transform. To incorporate the nanomechanical sensor, each plane wave component is then replaced with a numerical simulation of the total fields from a nanorod illuminated with the same plane wave. The nanorod's cylindrical symmetry is exploited to reduce the number of unique simulations. The beam is then reconstructed using an inverse Fourier transform and the beam is augmented with the appropriate total scattering of the nanorod. In this way, the only required numerical simulations are those of the nanorod under plane wave illumination in vacuum at various angles of incidence, easily performed via frequency-domain 3D finite-element-method simulations using the commercial software package *CST Microwave Studio* (Dassault Systemes).

Considering the linearity of Maxwell's equations, the fields for individual plane waves can be combined, with appropriate weighted amplitudes and phases, to synthesise the scattering from any desired structured far-field illumination - a step done in post-processing using MATLAB, which is applied to synthesise the counter-propagating Gaussian beams. The phases of the plane waves can be adjusted to shift the position of the beams and hence sweep the different nanorod locations. For each location, the result of this post-processing is the full 3D scattering field of the nanorod in a given position of the optical trap to no approximation beyond numerical accuracy. Once the 3D fields are obtained, calculating the torque requires performing the integration of Equation (4.21) over an arbitrary surface enclosing the nanorod. We chose a cube centred around the nanorod, and varied the cube's dimensions to ensure convergence of the result.

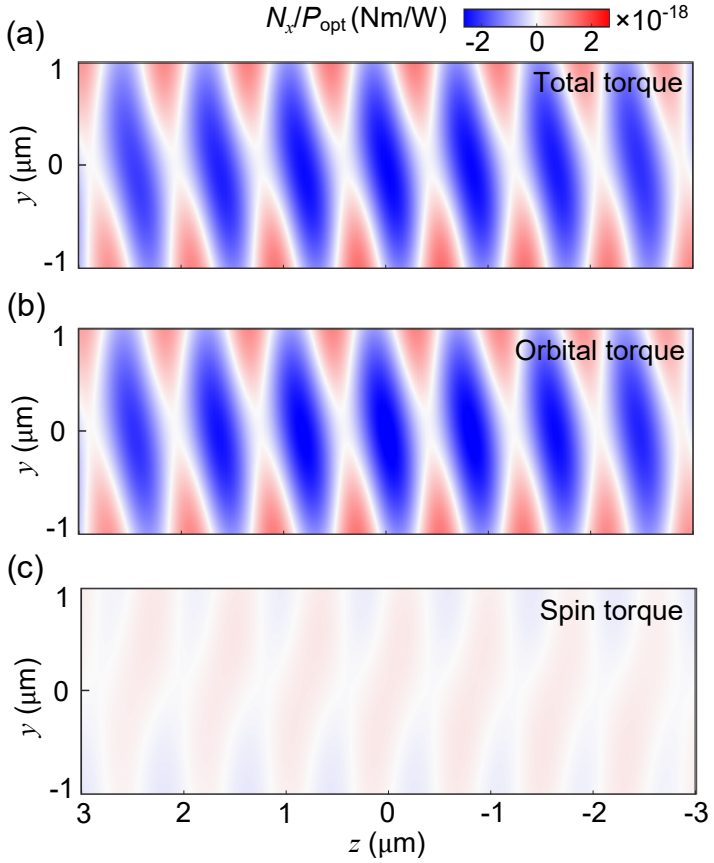

Figure 4.9: Torque calculation and decomposition. Numerically calculated torque component N_x acting on a y-oriented silicon nanorod placed at different positions in the y-z plane, using Maxwell's stress tensor. Each pixel comes from a full electromagnetic scattering simulation. (a) The map of the total torque on the nanorod as the position of the nanorod is changed. (b) A map of the TOAM torque. (c) A map of Transverse SAM torque.

The torque experienced by the nanorod is numerically computed for different positions of the nanorod on the y-z plane, with the rod oriented along y-direction, and the result is shown in Figure 4.9 (a). The resulting torque is oriented in the $-x$ direction, as expected from the illuminating TOAM, and is strongest at the electric field maxima where the rod is levitated by optical gradient forces.

The previous section shows the existence of a transverse SAM density in the centre of the optical trap, so there is both OAM and SAM in this system for the nanorod to experience a torque from. With respect to a possible role of transverse SAM on the rotation, we numerically calculated the torque coming from the flux of the spin and the orbital parts of the angular momentum separately [147, 149].

Using the torque decomposition method described in [149], we split the total torque in Figure 4.9 (a) into orbital and spin components. Figure 4.9 (b) and (c) show this decomposition and at the origin where the total torque is strongest, the orbital torque is roughly 15 times larger than the spin torque. The two torques also have opposite signs and so act against each other. We can therefore conclude that the OAM is the dominant source of torque in this optical trap, and the SAM torque is negligible compared to the OAM torque.

Figure 4.10 shows the theoretical calculated total torque of the levitated silicon nanorod at the trap centre with different offsets δ_x and δ_y in x- and y-directions respectively. As the sign of the y-direction offset δ_y changes, the normalized torque N_x/P_{opt} also alters its direction accordingly; however, the offset δ_x in the other direction only changes the magnitude of applied torque without changing its sign. We also notice that there is zero torque at the origin point when no offset is applied in both directions (i.e., $\delta_x = \delta_y = 0$).

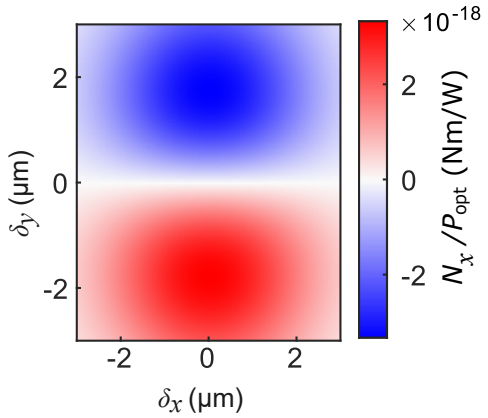

Figure 4.10: The theoretical variation in applied torque with the 2D offset of the beam. The colour map shows the sign (red: $+x$ direction; blue: $-x$ direction) and the magnitude of the normalized torque.

4.3.3 Experimental implementation

We use a standing wave optical dipole trap formed by two counter-propagating linearly polarised light beams focused inside a vacuum chamber. A pair of 1550 nm Gaussian beams are focused by two NA=0.6 lenses, such that their foci coincide, and a silicon nanorod is levitated in the anti-nodes of the resultant standing wave

field. The nanofabricated silicon nanorods (880 nm length and 210 nm diameter, Kelvin Nanotechnology) are grown on a silicon wafer before directly launching to the optical trap by LIAD described in Chapter 3 at the pressure of a few millibar [151].

Although the optical field defines where the particles are trapped in the x-y plane, they can be trapped in one of several antinodes of the optical standing wave. The field intensity, and therefore the torque, varies at the different antinodes. Our experimental measurement provides the absolute value of the torque, while our calculations provide the torque at the central antinode normalised by the power carried by the beams. The nanorods can be translated in the z-direction by changing the relative phase of the two beams, which we achieve by translating one of the fibre out-couplers in the z-direction.

Regarding the trapping location, the levitated nanorod is translationally trapped at the local maximum intensity (i.e., antinodes for a standing wave) where magnetic field vortices exist. However, in these locations, the levitated nanorod experience the largest transverse orbit and total torques due to its finite size, as shown in Figure 4.9, while the deeper physical mechanism is worthy of further investigation.

To generate the offset between the two beams, we linearly translate one of the fibre out-couplers by an amount ΔL. The two beams still overlap at the focus, but away from the focus an offset δ is introduced. The translation ΔL and the offset δ are linearly proportional to each other [152], with a proportionality constant that depends on the position along the z-axis. Since the absolute position along the z-axis is not known, we treat this proportionality constant as a free parameter when compared to theory. This described technique for generating a separation also induces a small angle between the beams (~ 0.04 rad), which has a negligible effect on the results of our numerical simulations.

We detect the motion of the levitated nanorod using a variety of methods, all based on collecting the light which has passed through the focus of the optical trap, as described in Section 2.4.5. The x, y-motion is measured by imaging the

beam onto a quadrant photodiode. The z-motion is monitored using balanced homodyne with light that hasn't interacted with the particle. This method is sensitive to rotation in the y-z plane, since the intensity of the collected scattered light is strongly dependent on the alignment of the nanorod. The α, β-motion is detected by passing the light through a polarising beam-splitter and performing a balanced polarisation measurement on the two output ports.

When a separation $|\delta_y| > 0$ is introduced, intrinsic TOAM is generated at the optical antinode, where the nanorod is trapped. The optical OAM is transferred to the nanorod, driving it to rotate. This is evident in the frequency spectrum of the nanorod motion, where rotation at MHz rates f_{rot} is detected (Figure 4.11 (a)), while the translational degrees of freedom remain harmonically confined with frequencies $f_{\{x,y,z\}}$. When $\delta_x = \delta_y = 0$, there is no rotation, and the nanorod is harmonically confined in all five degrees of freedom (Figure 4.11 (b)). When rotating, there is no confinement in the β direction, since this is the plane of rotation, and the motion in the α direction is gyroscopically stabilized [53].

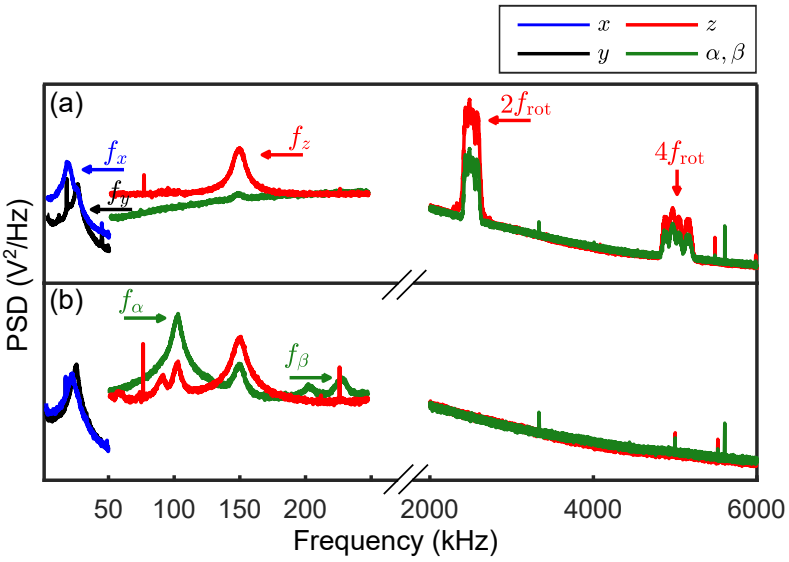

Figure 4.11: (a) PSD of the nanorod motion when driven to rotate at a frequency f_{rot} by TOAM. The centre-of-mass is confined with harmonic frequencies $f_{\{x,y,z\}}$. (b) PSD of a nanorod with no TOAM present, showing that the particle no longer rotates and is additionally confined in the librational degrees of freedom $\{\alpha, \beta\}$. Vertical-axis scales are not given as the data comes from a combination of detectors.

4.3.4 Transverse torque measurement

We probe the structured transverse optical momentum using the levitated silicon nanorod as an optomechanical sensor. The force and torque of small dipolar scatter can be directly associated to the field gradients and the local densities of optical linear and angular momenta in the illumination. In contrast, the size of a levitated nanorod used in our experiment is comparable to the optical wavelength, and its internal resonances can develop electric and magnetic high-order multipoles which interact with the incident fields.

The rotation rate of the nanorod is set by the balance between the optically induced torque N_{opt} and the damping due to the presence of gas Γ_{rot}, described in Equation (4.4):

$$f_{\mathrm{rot}} = \frac{N_{\mathrm{opt}}}{2\pi I \Gamma_{\mathrm{rot}}}, \tag{4.22}$$

Since Γ_{rot} is known (as discussed in Section 4.2) [104], the rotation rate is a probe of the torque induced by TOAM. We compare to the theoretically calculated

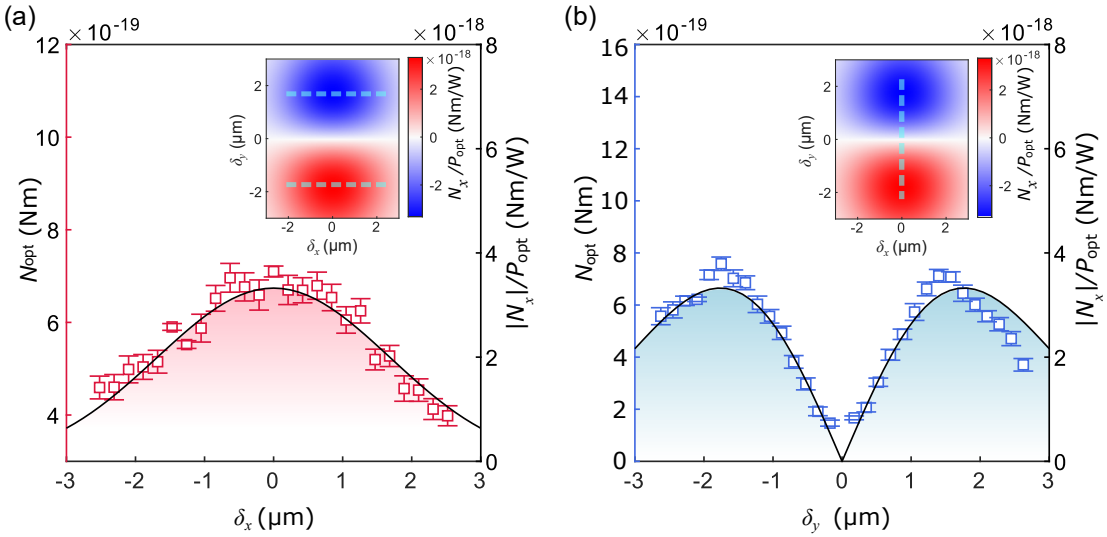

Figure 4.12: (a) The experimentally measured torque applied to the nanorod as a function of the offset δ_x (red squares), compared to the theoretical prediction (solid black line). The inset (adopted from Figure 4.10) shows the theoretical variation in applied torque with the 2D offset of the beams, and the dotted line indicated the separation explored in the figure. (b) The effect of a transverse offset δ_y on the torque applied to the nanorod by TOAM, with comparisons to theory as in (a).

torque by measuring the variation in torque as δ_y is varied, and note a maximum in N_{opt} for a finite separation $|\delta_y| > 0$, in Figure 4.12 (b), where the predicted torque is shown in the inset (adopted from Figure 4.10) and by the solid black line. If the rotation were simply due to the transfer of momentum from a single beam (e.g., in circularly polarised light) the maximum rotation rate would be when the optical intensity was a maximum ($\delta_y = 0$). For finite $|\delta_y|$, a separation along the x-direction yields a single maximum at $|\delta_x| = 0$, as predicted in solid black line and inset of Figure 4.12 (a).

For small $|\delta_y|$, there is a transition from rotation (Figure 4.13 (a)) to harmonic confinement (Figure 4.13 (b)) when the torque isn't large enough to overcome the optical potential which causes the nanorods to align along the polarisation direction. At the boundary, we observe bistable dynamics as stochastic forces due to collisions with gas molecules periodically driving the nanorod into rotation, as shown in (Figure 4.13 (c)).

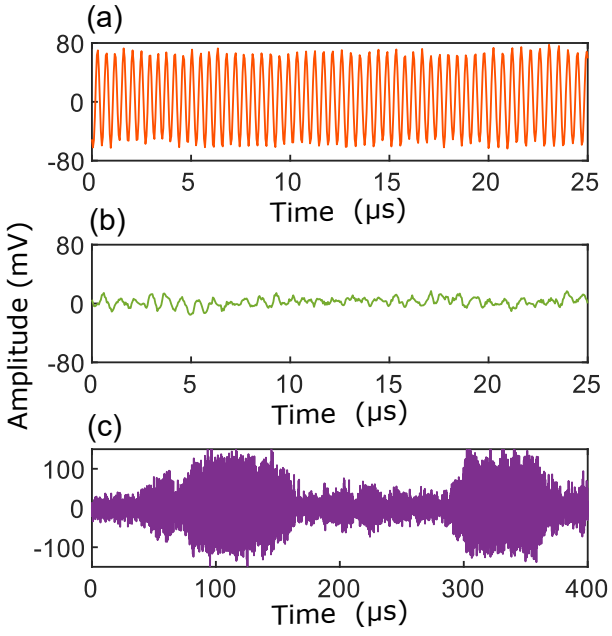

Figure 4.13: Time-series of the signal (along the z-axis) for a nanorod undergoing rotation driven by TOAM (a) for large $|\delta_y|$, and harmonically confined (b) for small $|\delta_y|$ when the torque isn't large enough to drive rotation. At the boundary of these regimes, bi-stable rotations are observed (c).

We observe that the rotation frequency of the nanorod due to the TOAM linearly depends on the gas pressure (Figure 4.14, blue points), which would not be the case for a motional frequency due to harmonic confinement [53]. Since the TOAM has a topological charge of -1, it would be expected that the optical torque is the same as for a particle exposed to circularly polarised light, which we confirm in Figure 4.14 (red squares), where the separation is reduced to $\delta_{\{x,y\}} = 0$ and the polarisation of each beam is switched to circular. By comparing to the literature [54, 63, 61], we note that the maximal torque we induce on our silicon nanorods ($\sim 3 \times 10^{-18}$ Nm) is five orders of magnitude larger than previously observed for particles levitated in vacuum. This is due to the shape enhanced susceptibility of our nanorods [53] as compared to nanospheres, ellipsoids or nanodumbells previously studied.

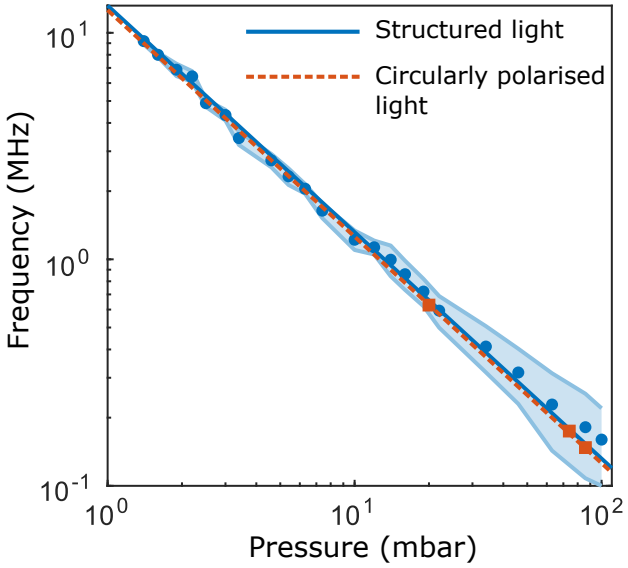

Figure 4.14: The rotational frequency scales linearly with pressure. The blue circles represent the mean value of f_{rot} when driven by TOAM and the shaded areas represent the full range of f_{rot}. This can be compared with the rotational frequency of a nanorod driven by circularly polarised light (red squares).

4.3.5 Summary and discussion

In this work, we have presented a straightforward method for synthesising a robust and stationary array of optical vortices carrying intrinsic TOAM, and carried out a unique study of this exotic optical orbital angular momentum using a levitated optomechanical sensor as a probe. Being able to exert significant optical forces transverse to the propagation direction of free-space beams, without the need to have critical optical alignment, localised interference patterns or polychromatic light, provides a powerful new tool for the optical manipulation of matter. Our work represents the first use of levitated particles as probes of structured light fields, exploiting the anisotropy of nanorods to measure optically induced torque.

Furthermore, we have introduced an exciting new method for the precise optical control of nanoparticles levitated in vacuum [7], where the intrinsic nature of the TOAM and still-present optical trap at the electric-field antinode enables the control of alignment and rotation without driving orbits. This new way of manipulating nanoparticles will be instrumental in cavity optomechanics [73] and the quantum control and exploitation of rotation [44]. The large optical torque we exert on the levitated silicon nanorods will enable sensitive torque sensing [63], and the transverse direction of the particle's angular momentum will allow the rotating particle to be brought close to surfaces to measure quantum friction [153], lateral Casimir [66], and other short-range forces [36].

Chapter 5

Ro-translational Optomechanical Cooling

5.1 Introduction

With the advantage of low dissipation by thermal contact with the environment or mechanical stress and strain, the levitated nanoparticle in vacuum provides an excellent approach to studying macroscopic quantum interference and microscopic thermodynamics. Having demonstrated the ability to implement measurement and control of all degrees of freedom motion (both translational and rotational) of levitated nanoparticles. It is of great interest and importance to develop methods to cool down the energy of a mechanical resonator towards the quantum regime.

In the 1970s, A. Ashkin *et al.* adopted an active feedback method to stabilize the motion of levitated microparticles against gravity [92]. In 2011, T. Li *et al.* first used three pairs of counter-propagating beams to actively cool a silica microsphere (1.5 μm radius) to 1.5 mK by utilising radiation pressure force in three spatial dimensions [23]. This active feedback with additional beams has been recently used to cool the librational mode of a levitated nanodumbbell to an effective temperature of around 10 K [77].

Applying electrostatic forces on charged nanoparticles also can introduce an additional damping [27, 154, 28]. The electrodes placed near the optical trap apply a Coulomb force $\mathbf{F}_Q = Q\mathbf{E}$, where Q is the total charge on the nanoparticle and $\mathbf{E}$

is the electric field at the location of the particle. Similar approaches successfully achieved ground-state cooling in 2021 by adopting optimal control feedback [29] or improving the measurement efficiency under a cryogenic environment [30].

Since the linear feedback force is velocity-dependent only, this feedback scheme is called cold damping. The feedback term is proportional to the velocity of the nanoparticle by:

$$F_{\mathrm{fb}} = -\mathrm{k}_{\mathrm{fb}}\dot{q}, \;\; q \in \{x, y, z\}, \tag{5.1}$$

where k_{fb} is the derivative feedback gain.

Although this linear feedback scheme is very efficient and powerful, it requires experimental implementations in each degree of freedom which increases the experimental complexity and challenge. The all-optical linear feedback using three auxiliary laser beams adds recoil heating noise, and electrical feedback relies on a finite net charge on the levitated nano-oscillator [49]. A novel parametric feedback cooling scheme by modulating the gradient force of the trapping light was demonstrated by J. Gieseler *et al.* in 2012, which achieved the centre-of-mass cooling of a charge-neutral silica nanosphere from room temperature to $\sim$ 50 mK [25], and reached the photon recoil limits with a minimum average phonon occupation number of $\bar{n} \simeq 63$ [26]. This method also was applied to cool the librational motion of a nano-dumbbell from room temperature to 240 mK recently, where the torque fluctuations arising from the zero-point fluctuations of the light field have been observed [76].

This chapter focus on the implementation of parametric feedback for cooling the ro-translational motions of levitated nanoparticles and proposed a new polarisation feedback method for cooling the librational motion of levitated nanorods in our experimental system.

5.2 Parametric feedback cooling

5.2.1 Working principle

In the parametric feedback scheme, the centre-of-mass motion of the levitated nanoparticle is monitored in real-time, and the intensity of the trapping light

is modulated based on the detected signal to adjust the trapping potential synchronously. The parametric feedback force becomes position-dependent and velocity-dependent:

$$F_{\text{para}} = -\mathrm{k}_{\text{para}} q^2 \dot{q}, \tag{5.2}$$

where $\mathrm{k}_{\text{para}} = \omega_q M \eta_{\text{para}}$ is the parametric feedback gain by applying a laser power modulation:

$$\delta P_{\text{opt}}(t) = P_{\text{opt}} \frac{\eta_{\text{para}}}{\omega_q} q\dot{q}. \tag{5.3}$$

The right phase relation between the feedback signal and the motion of nanoparticles is the crucial point of this method to extract or deposit the particle's motional energy. For parametric feedback cooling, the phase of the feedback signal is shifted to ensure that the trap potential is stiffened when the particle is away from the centre and loosened when the particle moves towards the centre, as illustrated in Figure 5.1.

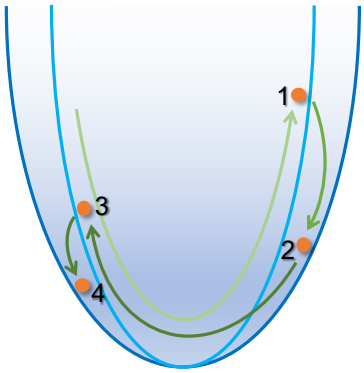

Figure 5.1: Working principle of parametric feedback cooling via modulating the optical potential. The trap stiffness is increased when the trapped nanoparticle travels away from the centre, which hinders the motion of the trapped particle. When the particle moves towards the centre of the trap, the trap potential decreases, thereby reducing the energy of the particle.

As a result of the feedback modulation, the centre-of-mass energy of the nanoparticle decreases. On the contrary, we can amplify the motion by an additional phase shift.

By introducing the modulation signal, Equation (2.42) can be modified as:

$$\ddot{q}(t) + (\Gamma_{\mathrm{CM}} + \delta\Gamma)\dot{q}(t) + (\omega_q + \delta\omega_q)^2 q(t) = \frac{1}{M}\left[F_{\mathrm{fluct}}(t) + F_{\mathrm{para}}(t)\right], \tag{5.4}$$

where $F_{\mathrm{para}}(t)$ is a time-varying, non-conservative force introduced by parametric feedback control. $\delta\Gamma$ and $\delta\omega_q$ are the additional damping rate and the frequency shift resulting from the parametric feedback loop. The frequency shift $\delta\omega_q$ is proportional to the square root of the optical power P_{opt}, since the oscillation frequency is determined by the trap stiffness k_q in Equation (2.31). From the aspect of energy space, the dynamics of the levitation system with feedback can be considered as equilibrium dynamics occurring in a system with an additional force term [31]. It is worth noting that parametric feedback can be performed on all degrees of freedom simultaneously since the optical gradient force points towards the trap centre in all directions.

5.2.2 Experimental implementation

Figure 5.2 sketches the experimental implementation of parametric feedback cooling. The motion of the levitated nanoparticle in different directions is detected by various detection configurations as described in Chapter 2.

After we obtain the position information for each spatial direction, we send the signal output from the photodetectors to a lock-in amplifier with phase-locked loops (PLLs). The locked-in amplifier can track the oscillation frequency and phase of the detected signal. Appropriate high-pass filters and band-pass filters (the centre frequency set to the nanoparticle's oscillation frequency) are applied to effectively isolate the DC component noise and other electronic noise. In order to apply parametric feedback, the signal in each axis is frequency doubled with a phase shift and an amplitude gain. By summing the feedback signal together for all three directions, it is connected to an AOM driver (Agile RF Synthesizer, MOGLabs) to drive an in-fibre AOM for laser intensity modulation, therefore generating a parametric modulation of the optical trap. Under the modulation of the optical trap, the effective temperature of the levitated nanoparticle is cooled

down or heated up with different phase shifts.

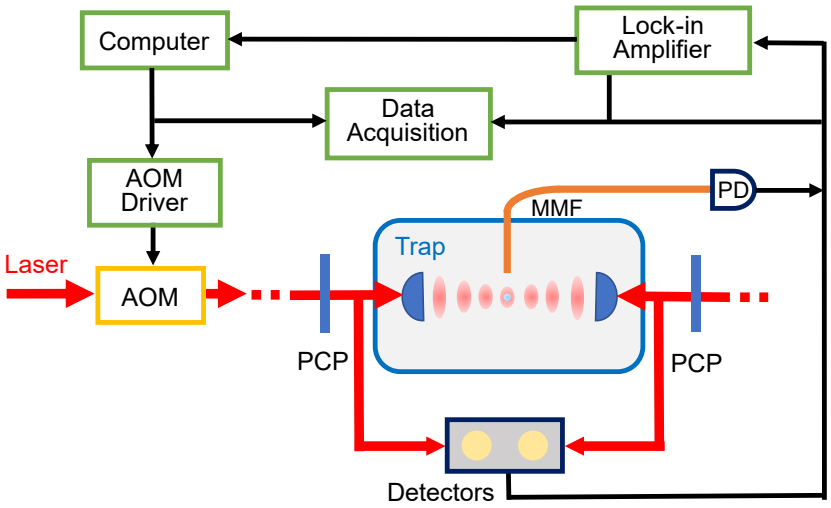

Figure 5.2: Schematic of the parametric feedback cooling. A standing wave trap formed by two counter-propagating beams is used to levitate a nanoparticle inside a vacuum chamber. The scattered light of the levitated nanoparticle and its interference field are detected by different detectors. A lock-in amplifier with PLLs is used to track the phase of the oscillation signal from levitated nanoparticles, double the frequency, and output a feedback signal with an amplitude gain and a phase shift. The three-axis combined feedback signal is sent to a digital AOM driver to drive the AOM with intensity modulation.

5.2.3 Experimental results

By modulating the optical potential with a correct phase shift, the energy of the levitated particle decreases, and its centre-of-mass effective temperature can be cooled down. According to the equipartition theorem, the effective temperature of its centre-of-mass motion:

$$k_{\mathrm{B}} T_{\mathrm{CM}}^{(q)} = M\omega_q^2 \left\langle q^2 \right\rangle, \tag{5.5}$$

can be modified as:

$$T_{\mathrm{eff}} = T_{\mathrm{CM}}^{(q)} \frac{\Gamma_{\mathrm{CM}}}{\Gamma_{\mathrm{CM}} + \delta\Gamma}, \tag{5.6}$$

where $\delta\Gamma$ is the additional feedback damping. T_{CM} is the equilibrium temperature in the absence of the parametric feedback when $\delta\Gamma = 0$. The effective temperature

T_{eff} of the particle can be increased by negative damping and decreased by positive damping based on the sign of $\delta\Gamma$.

Correspondingly, the PSD spectrum can be written as:

$$\begin{aligned} S_{\text{qq}}(\omega) &= \frac{1}{2\pi}\int_{-\infty}^{\infty}\langle q(t)q(t-t')\rangle\, e^{-i\omega t'}dt' \\ &= \frac{k_{\text{B}}T_{\text{eff}}}{\pi M}\frac{\Gamma_{\text{CM}}}{\left[(\omega_q+\delta\omega_q)^2-\omega_q^2\right]^2+\omega_q^2(\Gamma_{\text{CM}}+\delta\Gamma_q)^2}. \end{aligned} \tag{5.7}$$

Figure 5.3 shows the PSD spectra of the z-motion acquired in different pressures and effective temperatures with parametric feedback. The colour area under the curves is proportional to T_{eff}. The shift of oscillation frequency probably resulted from the laser power fluctuation which slightly alters the trap stiffness and introduces a fluctuation in the mechanical oscillation frequency.

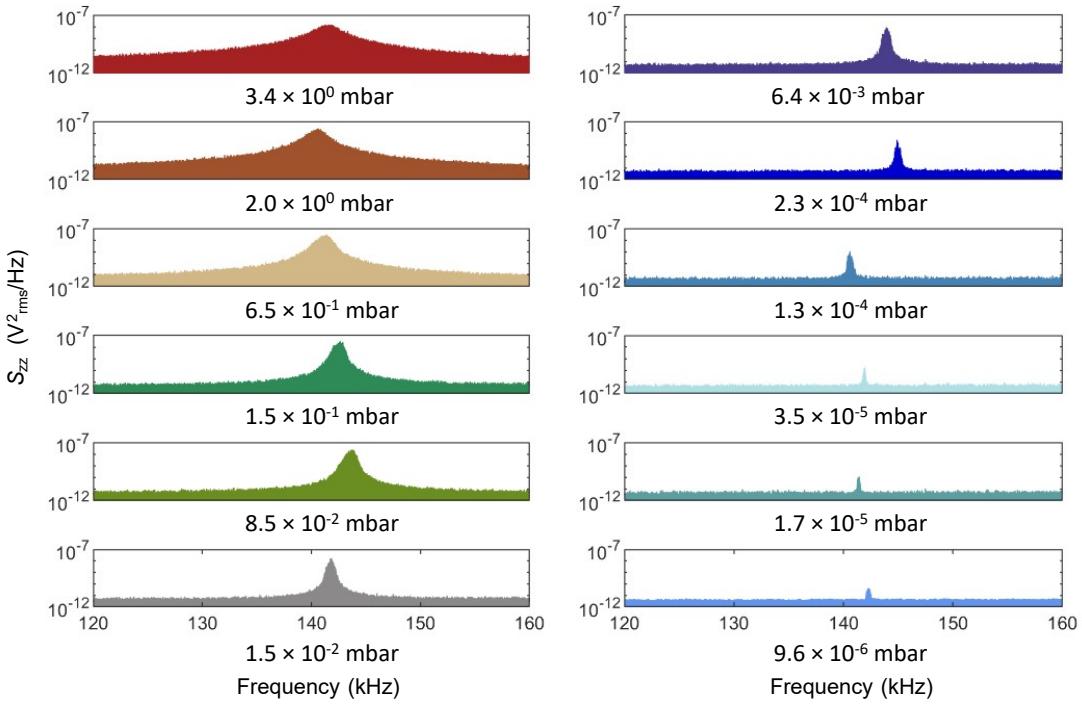

Figure 5.3: PSD spectra of z-motion of a 300nm diameter silica nanosphere for different pressures and effective temperatures T_{eff} with parametric feedback cooling. The trapping power is about 400mW in total with a pair of focusing lenses NA = 0.43.

We extract the effective temperature of the levitated oscillator by fitting the PSD spectrum based on Equation (5.7). Figure 5.4 presents the experimental results of parametric feedback cooling. Under the same feedback gain, decreasing the pressure reduces the heating from the residual gas molecules and a lower effective temperature can be achieved. When the pressure is lower enough, the feedback can bring the detected motion closer to the noise floor, and even "noise squashing" (i.e., the measured signal curve is below the noise floor) can be observed with larger feedback gain [27].

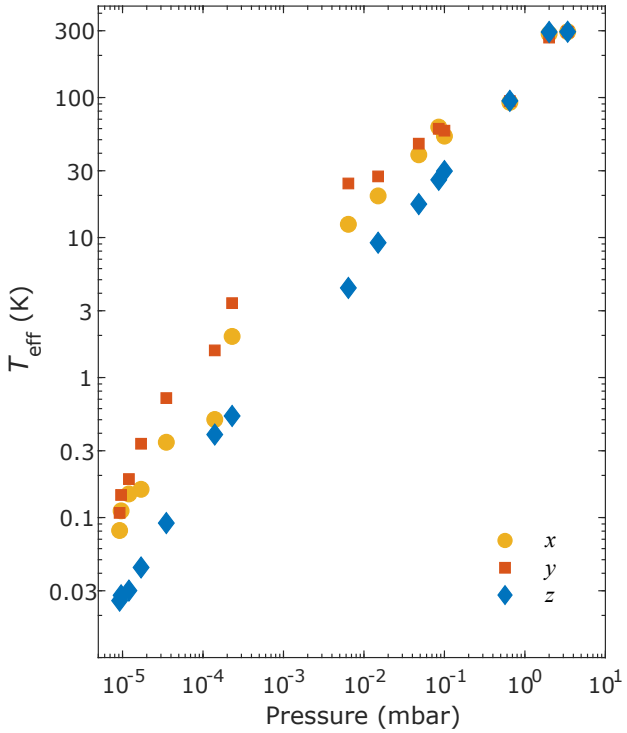

Figure 5.4: The dependence of the effective temperature T_{eff} of centre-of-motion of a levitated nanosphere on pressure P_{gas} ranging from $\sim$ 10 mbar to $\sim 10^{-5}$ mbar. The lowest achieved T_{eff} is $\sim$ 100 mK for x,y-motion, and $\sim$ 30 mK z-motion.

The ultimate minimum achievable temperature T_{eff} is limited by the feedback control competing with reheating due to energy exchange with gas molecules for each pressure value, which is $\sim$ 100 mK for x,y-motion, and $\sim$ 30 mK z-motion at the pressure of $\sim 1 \times 10^{-5}$ mbar in our experiments. The effective temperature is proportional to $\sqrt{\Gamma_{\mathrm{CM}}}$, as theoretically predicted.

We also investigate the effect of different feedback gains on the performance in our feedback cooling scheme at a pressure of $\sim 1 \times 10^{-5}$ mbar, as plotted in Figure 5.5. By changing the modulation amplitude of the feedback signal, the feedback gain and the induced feedback damping rate on the levitated oscillator can be adjusted. According to the theoretical relationship, the effective temperature is inversely proportional to the square root of feedback gain in theory. Starting with a lower gain, the effective temperature decreases with the increased gain; while it also increases with the further increase of modulation amplitude, yielding a minimum temperature with an optimal feedback gain.

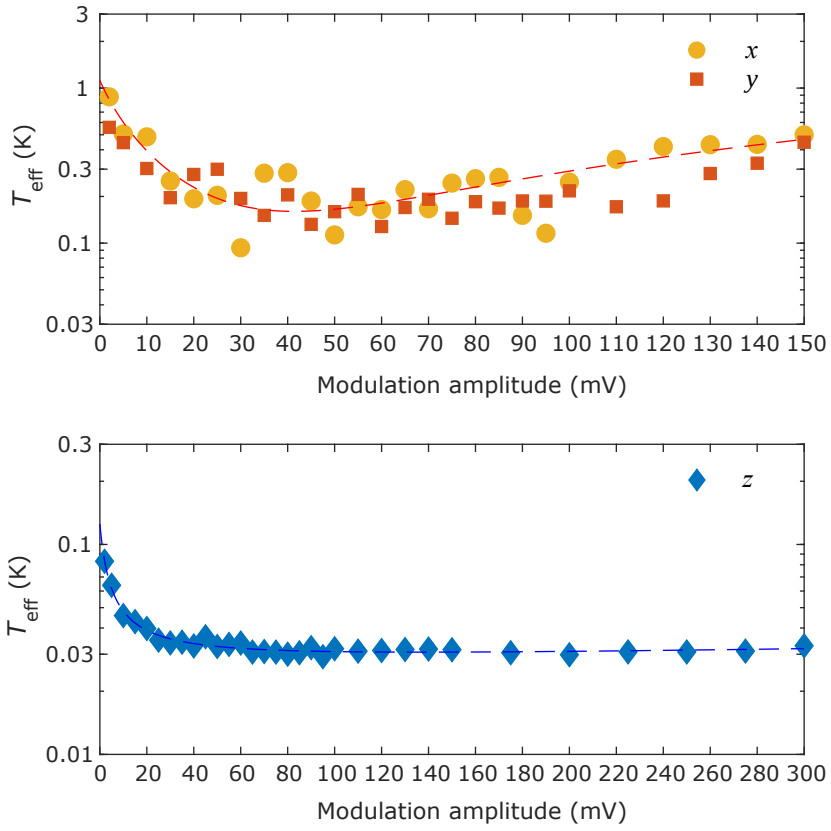

Figure 5.5: Dependence of the effective temperature of translational motion of a levitated nanosphere on the parametric feedback modulation amplitude. The dashed fitted line is consistent with the theoretical relationship.

5.3 Polarisation feedback cooling

While the parametric feedback method provides an efficient approach to cool centre-of-mass motion, the control and cooling of rotational degrees of freedom remain to be the central readout of interest. In this section, a new polarisation feedback method for simultaneously cooling the librational motion (α and β) of a levitated nanorod is proposed and numerically simulated. This novel method is based on the modulation of the linearly polarised trapping light to feedback damping librational motion. Combined with the parametric feedback cooling on the centre-of-mass motion, it is promising to achieve five degrees of freedom cooling for levitated nanorods, which paves the way to explore macroscopic quantum phenomenon by utilising the ro-translational degrees of freedom.

5.3.1 Hamiltonian of levitated nanorods

The general form of the ro-translational kinetic energy of a levitated asymmetrical nanoparticle is given by:

$$\begin{aligned}\mathcal{H}_0 = \frac{\mathbf{p}^2}{2M} &+ \frac{1}{2I_a}\left(\cos\gamma\frac{p_\alpha - p_\gamma\cos\beta}{\sin\beta} - p_\beta\sin\gamma\right)^2 \\ &+ \frac{1}{2I_b}\left(\sin\gamma\frac{p_\alpha - p_\gamma\cos\beta}{\sin\beta} + p_\beta\cos\gamma\right)^2 \\ &+ \frac{p_\gamma^2}{2I_c},\end{aligned} \tag{5.8}$$

where $\{I_a, I_b, I_c\}$ is the moment of inertia for each axis in the body-fixed frame, $\mathbf{p}$ is the momentum of translational degrees of freedom and $\{p_\alpha, p_\beta, p_\gamma\}$ is the angular momentum in each angle.

For a levitated nanorod with symmetrical shape in α and β directions, this leads to $I_\alpha = I_\beta \equiv I$, $I_c \equiv I_\gamma$ and the Equation (5.8) can be rewritten as:

$$\mathcal{H}_{0,\mathrm{rod}} = \frac{\mathbf{p}^2}{2M} + \frac{1}{2I}\left[\frac{(p_\alpha - \cos\beta p_\gamma)^2}{\sin^2\beta} + p_\beta^2\right] + \frac{p_\gamma^2}{2I_\gamma}, \tag{5.9}$$

where we can notice that the ro-translational kinetic energy and the optical potential in Equation (2.41) are independent of the Euler angle γ, therefore the angular

momentum p_γ is conserved which cannot be controlled by the linearly polarised trapping field.

By summing up the kinetic energy and optical potential terms, we have the total Hamiltonian of the optically levitated nanorod $\mathcal{H}_{\text{total}} = \mathcal{H}_{0,\text{rod}} + U_{\text{opt,rod}}$. The equations of motion for the Euler angles and their momenta can be derived from the total Hamiltonian:

$$\begin{aligned}
\dot{\alpha} =& \frac{\cos\gamma}{I\sin\beta}\left[\cos\gamma\left(\frac{p_\alpha - p_\beta\cos\beta}{\sin\beta}\right) - p_\beta\sin\gamma\right] \\
&+ \frac{\sin\gamma}{I\sin\beta}\left[\sin\gamma\left(\frac{p_\alpha - p_\gamma\cos\beta}{\sin\beta}\right) + p_\beta\cos\gamma\right], \\
\dot{\beta} =& -\frac{\sin\gamma}{I}\left[\cos\gamma\left(\frac{p_\alpha - p_\gamma\cos\beta}{\sin\beta}\right) - p_\beta\cos\gamma\right] \\
&+ \frac{\cos\gamma}{I}\left[\sin\gamma\left(\frac{p_\alpha - p_\beta\cos\beta}{\sin\beta}\right) + p_\beta\cos\gamma\right], \\
\dot{\gamma} =& \frac{p_\gamma}{I_\gamma} - \frac{\cos\gamma\cos\beta}{I\sin\beta}\left[\cos\gamma\left(\frac{p_\alpha - p_\beta\cos\beta}{\sin\beta}\right) - p_\beta\sin\gamma\right] \\
&- \frac{\sin\gamma\cos\beta}{I\sin\beta}\left[\sin\gamma\left(\frac{p_\alpha - p_\beta\cos\beta}{\sin\beta}\right) + p_\beta\cos\gamma\right],
\end{aligned} \tag{5.10}$$

and the corresponding angular momenta:

$$\begin{aligned}
\dot{p}_\alpha =& \frac{2\epsilon_0 V E_0^2}{4}\Big\{\chi_\perp[\hat{\mathbf{n}}_a\cdot\mathbf{e}][e_x(-\sin\alpha\cos\beta\cos\gamma - \cos\alpha\sin\gamma) \\
&+ e_y(\cos\alpha\cos\beta\cos\gamma)] \\
&+ \chi_\perp[\hat{\mathbf{n}}_b\cdot\mathbf{e}][e_x(\sin\alpha\cos\beta\sin\gamma - \cos\alpha\cos\gamma) \\
&+ e_y(-\cos\alpha\cos\beta\sin\gamma - \sin\alpha\cos\beta)] \\
&+ \chi_\parallel[\hat{\mathbf{n}}_c\cdot\mathbf{e}][e_x(-\sin\alpha\sin\beta) + e_y(\cos\alpha\sin\beta)]\Big\},
\end{aligned} \tag{5.11}$$

$$
\begin{aligned}
\dot{p}_\beta = &-\frac{1}{I}\left[p_\gamma\cos\gamma - \frac{\cos\gamma\cos\beta}{\sin\beta}\left(\frac{p_\alpha - p_\beta\cos\beta}{\sin\beta}\right)\right] \\
&\cdot\left[\sin\gamma\left(\frac{p_\alpha - p_\beta\cos\beta}{\sin\beta}\right) - p_\beta\sin\gamma\right] \\
&-\frac{1}{I}\left[p_\gamma\sin\gamma - \frac{\sin\gamma\cos\beta}{\sin\beta}\left(\frac{p_\alpha - p_\beta\cos\beta}{\sin\beta}\right)\right] \\
&\cdot\left[\sin\gamma\left(\frac{p_\alpha - p_\beta\cos\beta}{\sin\beta}\right) + p_\beta\cos\gamma\right] \\
&+\frac{2\epsilon_0 V E_0^2}{4}\Big\{\chi_\perp[\hat{\mathbf{n}}_a\cdot\mathbf{e}][e_x(-\cos\alpha\sin\beta\cos\gamma) \\
&+ e_y(-\sin\alpha\sin\beta\cos\gamma)] \\
&+\chi_\perp[\hat{\mathbf{n}}_b\cdot\mathbf{e}][e_x(\cos\alpha\sin\beta\sin\gamma) + e_y(\sin\alpha\sin\beta\sin\gamma)] \\
&+\chi_\parallel[\hat{\mathbf{n}}_c\cdot\mathbf{e}][e_x(\cos\alpha\cos\beta) + e_y(\sin\alpha\cos\beta)]\Big\},
\end{aligned}
\tag{5.12}
$$

$$
\begin{aligned}
\dot{p}_\gamma = &-\frac{1}{I}\left[-p_\beta\sin\gamma + \cos\gamma - \left(\frac{p_\alpha - p_\beta\cos\beta}{\sin\beta}\right)\right] \\
&\cdot\left[-\sin\gamma\left(\frac{p_\alpha - p_\beta\cos\beta}{\sin\beta}\right) - p_\beta\cos\gamma\right] \\
&-\frac{1}{I}\left[-p_\beta\sin\gamma + \cos\gamma\left(\frac{p_\alpha - p_\beta\cos\beta}{\sin\beta}\right)\right] \\
&\cdot\left[\sin\gamma\left(\frac{p_\alpha - p_\beta\cos\beta}{\sin\beta}\right) + p_\gamma\right] \\
&+\frac{2\epsilon_0 V E_0^2}{4}\Big\{\chi_\perp[\hat{\mathbf{n}}_a\cdot\mathbf{e}][e_x(-\cos\alpha\cos\beta\sin\gamma - \sin\alpha\cos\gamma) \\
&+ e_y(-\sin\alpha\cos\beta\cos\gamma - \cos\gamma\sin\gamma)] \\
&+\chi_\perp[\hat{\mathbf{n}}_b\cdot\mathbf{e}][e_x(-\cos\alpha\cos\beta\cos\gamma) \\
&+ e_y(-\sin\alpha\cos\beta\cos\gamma - \cos\alpha\sin\gamma)]\Big\},
\end{aligned}
\tag{5.13}
$$

where $\{\hat{\mathbf{n}}_a, \hat{\mathbf{n}}_b, \hat{\mathbf{n}}_c\}$ are the orientation unit vectors in terms of Euler angles in the body-fixed frame, and $\mathbf{e}$ is the polarisation vector of the light field with two components $\{e_x, e_y\}$ in the x-y space-fixed coordinates respectively.

However, these equations mentioned above have not considered the damping and the stochastic forces or torques from background gas molecules and other noise sources. We modify the equations of motion by considering additional white noise terms:

$$\begin{aligned}
\dot{z} &= \frac{p_z}{M}, \\
\dot{\alpha} &= \frac{p_\alpha - p_\gamma \cos\beta}{I \sin^2\beta}, \\
\dot{\beta} &= \frac{p_\beta}{I}, \\
\dot{\gamma} &= -\cos\beta \frac{p_\alpha - p_\gamma \cos\beta}{I \sin^2\beta} + \frac{p_\gamma}{I_\gamma},
\end{aligned} \tag{5.14}$$

and their corresponding momenta are described by:

$$\begin{aligned}
\dot{p}_z =& -\frac{\epsilon_0 V \chi_\parallel E_0^2}{4} k \sin(2kz) \left[\frac{\chi_\perp}{\chi_\parallel} + \frac{\Delta\chi}{\chi_\parallel}(\mathbf{m}\cdot\mathbf{e})^2\right] \\
& - \Gamma_z p_z + \sqrt{2M\Gamma_z k_\mathrm{B} T_b} W_z, \\
\dot{p}_\alpha =& \frac{2\epsilon_0 V \Delta\chi E_0^2}{4} \cos^2(kz)(\mathbf{m}\cdot\mathbf{e})(e_y\cos\alpha - e_x\sin\alpha) \\
& - \Gamma_\perp p_\alpha - (\Gamma_\parallel - \Gamma_\perp)\cos\beta p_\gamma \\
& + \sqrt{2I\Gamma_\perp k_\mathrm{B} T_b} W_\alpha + \sqrt{2I_\gamma \Gamma_\parallel k_\mathrm{B} T_b}\cos\beta W_\gamma, \\
\dot{p}_\beta =& \frac{1}{I}\left[\frac{(p_\alpha - p_\gamma\cos\beta)^2}{\sin^2\beta} cos\beta - p_\gamma \frac{p_\alpha - p_\gamma\cos\beta}{\sin\beta}\right] \\
& + \frac{2\epsilon_0 V \Delta\chi E_0^2}{4} \cos^2(kz)(\mathbf{m}\cdot\mathbf{e})\cos\beta(e_x\cos\alpha + e_y\sin\alpha) \\
& - \Gamma_\perp p_\beta + \sqrt{2I\Gamma_\perp k_\mathrm{b} T_b} W_\beta, \\
\dot{p}_\gamma =& \Gamma_\parallel p_\gamma + \sqrt{2I\gamma_\perp k_\mathrm{B} T_b} W_\gamma,
\end{aligned} \tag{5.15}$$

where $\Gamma_z, \Gamma_\perp, \Gamma_\parallel$ are the damping rates discussed in Chapter 2, and $W_z, W_\alpha, W_\beta, W_\gamma$ are independent white noise terms.

5.3.2 Protocol of polarisation feedback cooling

In the previous section, the ro-translational dynamics of the levitated nano-oscillator have been studied, and we can acquire information of the centre-of-mass motion and librational motion of levitated nanorods in experiments. Based on the measurement of its motion, we can control and cool the motion in each de-

gree of freedom with different approaches. For centre-of-mass motion, parametric feedback cooling is discussed in previous sections. Here we present a new path for cooling the energy of librational modes via polarisation feedback scheme.

Figure 5.6 shows the schematic of the polarisation feedback cooling. We use the phased-locked module of the lock-in amplifier to real-time track the frequencies and phase-locked of the rotational degrees of freedom of the particle, then generate a modulation signal. The modulation signal is processed by the computer with an FPGA module. With the varying modulation signal from the lock-in amplifier, the FPGA process and output signals correspond to the polarisation state based on the calibrated voltages (see Appendix A). The analogue signals are amplified by a voltage amplifier and applied on a high-speed EOM for polarisation modulation.

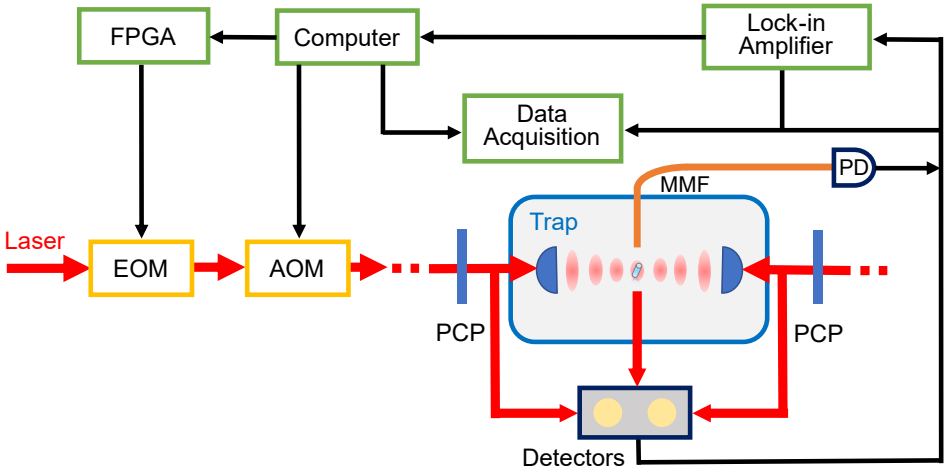

Figure 5.6: The basic schematic of the polarisation feedback cooling. The information of the librational motion can be acquired in real-time from the balanced polarisation measurement, which is sent to a lock-in amplifier for frequency tracking and phase locking and then generates feedback signals to the computer with an FPGA module. The polarisation state of trapping light is modulated by an EOM according to the feedback signal.

In the polarisation feedback, the nanorod is levitated by a pair of linearly polarised beams which we define as:

$$\mathbf{e}(\varphi(t)) = \cos(\varphi(t))\hat{\mathbf{e}}_x + \sin(\varphi(t))\hat{\mathbf{e}}_y, \tag{5.16}$$

where $\varphi(t)$ is the time variable, and $\hat{\mathbf{e}}_x, \hat{\mathbf{e}}_y$ are the unit vector in x, y-direction.

The linearly polarised field has the x, y components on the x-y plane, which is the same plane as the rotational degree of freedom of α. This means the orientation of the levitated nanorod tends to align with the linear polarisation direction, yielding a minimum optical potential. If we set $\varphi \propto \alpha$, it reduces the potential initially, but it does not slow the motion and p_α remains constant without additional damping. If we introduce an angular velocity of the librational motion $\dot{\alpha}$:

$$\varphi(t) = \alpha(t) - \tau\dot{\alpha}(t), \tag{5.17}$$

where τ is a constant time parameter which satisfy $0 < \tau < 1/(2f_\alpha)$ and f_α is the α-librational frequency of a deeply trapped nanorod. However, this parameterization does introduce damping in the α-motion, but leaves β-motion largely untouched with an uncooled angular momentum p_γ. Since both α and β motion are gyroscopically coupled to the angular momentum p_γ which is a conserved quantity for levitated nanorods, it has the potential to heat the α-motion via the coupling between these modes. Therefore, we seek to simultaneously cool α and β motion so that they can be effectively decoupled and achieve the lowest attainable energy limited by p_γ and measurement noise. This can be achieved by setting the polarisation as:

$$\begin{aligned} \varphi(t) &= \alpha(t) - \tau\left[\dot{\alpha}(t) - \dot{\beta}(t)\right] \quad \text{for } p_\gamma > 0, \\ \varphi(t) &= \alpha(t) - \tau\left[\dot{\alpha}(t) + \dot{\beta}(t)\right] \quad \text{for } p_\gamma < 0. \end{aligned} \tag{5.18}$$

Without considering the translational degrees of freedom, the rotational Hamiltonian of a levitated nanorod is given by combining Equations (2.41) and (5.9):

$$\mathcal{H}_{\text{rot}} = \frac{(p_\alpha - p_\gamma \cos\beta)^2}{2I\sin^2\beta} + \frac{p_\beta^2}{2I} + \frac{p_\gamma^2}{2I_\gamma} - \frac{1}{2}I\omega_{\text{libr}}^2(\mathbf{m}\cdot\mathbf{e})^2, \tag{5.19}$$

where ω_{libr} is the angular librational frequency which is approximated to ω_α and ω_β with $\omega_{\text{libr}} = \omega_\alpha = \omega_\beta \simeq \sqrt{(\epsilon_0 V \Delta\chi E_0^2)/(2I)}$ in the deeply trapped regime where the nanorod remains largely aligned with the filed and $\dot{\alpha}$, $\dot{\beta}$ are small. By

introducing the time variable φ, the term $(\mathbf{m}\cdot\mathbf{e})$ can be written as:

$$\begin{aligned}(\mathbf{m}\cdot\mathbf{e}) &= \sin\beta(\cos\alpha\cos\varphi+\sin\alpha\sin\beta) = \sin\beta\cos(\alpha-\varphi),\\ (\mathbf{m}\cdot\mathbf{e})^2 &= \sin^2\beta\cos^2(\alpha-\varphi),\end{aligned} \tag{5.20}$$

for Equation (5.15), therefore the Hamiltonian for rotational degrees of freedom becomes:

$$\mathcal{H}_{\text{rot}} = \frac{(p_\alpha - p_\gamma\cos\beta)^2}{2I\sin^2\beta} + \frac{p_\beta^2}{2I} + \frac{p_\gamma^2}{2I_\gamma} - \frac{1}{2}I\omega_{\text{libr}}^2\sin^2\beta\cos^2(\alpha-\varphi). \tag{5.21}$$

With the parameterization equation in Equation (5.18) and we make the following mapping:

$$\begin{aligned}\alpha &\simeq \varphi \simeq \zeta_1,\\ \beta - \frac{\pi}{2} &\simeq \zeta_2 \ll 1,\end{aligned} \tag{5.22}$$

and

$$\begin{aligned}\dot{\zeta}_1 &= \dot{\alpha},\\ \dot{\zeta}_2 &= \dot{\beta}.\end{aligned} \tag{5.23}$$

By substituting Equation (5.23) to Equations (5.14) and (5.15) and taking the first order expansion of $\sin, \cos, \sin^2\cos^2$, the equations of librational motion becomes (here omit the white noise term in each equation):

$$\begin{aligned}\dot{\zeta}_1 &\simeq \frac{p_\alpha}{I} + \zeta_2\frac{p_\gamma}{I},\\ \dot{\zeta}_2 &\simeq \frac{p_\beta}{I},\end{aligned} \tag{5.24}$$

and

$$\begin{aligned}\dot{p}_\alpha &\simeq -I\omega_{\text{libr}}^2(\zeta_1-\varphi),\\ \dot{p}_\beta &\simeq -\frac{p_\alpha p_\gamma}{I} - \frac{\zeta_2 p_\gamma^2}{I} - I\omega_{\text{libr}}^2\zeta_2.\end{aligned} \tag{5.25}$$

Taking the time derivative of $\dot{\zeta}_1$ and $\dot{\zeta}_2$, we can obtain the angular accelera-

tions which show the information on how the angular velocity changes:

$$\begin{aligned}\ddot{\zeta_1} &= \frac{p_\gamma}{I}\dot{\zeta_2} - \omega_{\text{libr}}^2(\zeta_1 - \varphi),\\ \ddot{\zeta_2} &= -\frac{p_\gamma}{I}\dot{\zeta_1} - \omega_{\text{libr}}^2\zeta_2.\end{aligned} \tag{5.26}$$

From the first terms of the above Equation (5.26), we can clearly see that ζ_1 and ζ_2 (i.e., α and β) are coupled to each other via the bridge of non-zero angular momentum p_γ. By choosing $\varphi(t)$ in Equation (5.18), the above equation becomes:

$$\ddot{\zeta_1} = -\omega_{\text{libr}}^2\tau\dot{\zeta_1} + \left(\omega_{\text{libr}}^2\tau + \frac{p_\gamma}{I}\right)\dot{\zeta_2}, \tag{5.27}$$

where the choice of parameterization introduces a damping term for ζ_1 (i.e., α), and it reach a quasi-steady state $\zeta_1 = 0$ when:

$$\dot{\zeta_1} = \left(1 + \frac{p_\gamma}{I\omega_{\text{libr}}^2\tau}\right)\dot{\zeta_2}, \tag{5.28}$$

and at this moment for ζ_2 (i.e., β) motion in Equation (5.26):

$$\ddot{\zeta_2} = -\frac{p_\gamma}{I}\dot{\zeta_2} - \frac{p_\gamma^2}{I^2\omega_{\text{libr}}^2\tau}\dot{\zeta_2} - \omega_{\text{libr}}^2\zeta_2. \tag{5.29}$$

By rearranging Equations (5.27) and (5.29), the equations of motion for α and β are given by :

$$\begin{aligned}\ddot{\alpha} &= -\omega_{\text{libr}}^2\tau\dot{\alpha} + \left(\omega_{\text{libr}}^2\tau + \frac{p_\gamma}{I}\right)\dot{\beta},\\ \ddot{\beta} &= -\frac{p_\gamma}{I}\dot{\beta} - \frac{p_\gamma^2}{I^2\omega_{\text{libr}}^2\tau}\dot{\beta} - \omega_{\text{libr}}^2\left(\beta - \frac{\pi}{2}\right),\end{aligned} \tag{5.30}$$

where the largest damping contribution is from the first term on the right-hand side when $p_\gamma > 0$. For $p_\gamma < 0$, we can choose the opposite sign in Equations (5.18) and (5.30). In principle, the introduced damping for α and β-motion yields simultaneously cooling the energy of librational modes p_α and p_β via an untouched non-zero p_γ. During the decrease of $\dot{\beta}$, it breaks the quasi-steady state which allows for further damping on α until reaching a quasi-steady again. This cycle continues

and brings $\dot{\alpha}$ and $\dot{\beta}$ simultaneously lower and lower, yielding the simultaneous cooling of both rotational degrees of freedom via polarisation feedback.

5.3.3 Numerical simulation

As discussed in Chapter 3, the stochastic differential equations can be solved by different numerical methods, such as the Euler method or the Runge-Kutta method (e.g., algorithm *ode45* based on higher-order Runge-Kutta in MATLAB). Considering the measurement error of the particle's motion needs to be added in the implementation of feedback cooling with extra independent stochasticity, we use the explicit Euler method to numerically solve the first order of ordinary differential equations discussed in the previous section and simulate the dynamics of the levitated nanorod under polarisation feedback.

We use dimensionless variables in our simulation, which is to avoid computational rounding errors that can occur when dealing with very small numerical values. For example, the value of momentum p_α is proportional to $\epsilon_0 V$ at the order of magnitude of 10^{-32}, which is easily rounded to zero during calculation. The transformation of variables to dimensionless for the levitated nanorod is:

$$\begin{aligned}
&\tilde{t} = \omega t, \\
&\tilde{q} = kq, \quad q \in \{x, y, z\}, \\
&\tilde{p} = \frac{k}{M\omega} p, \\
&\tilde{\Omega} = \Omega, \quad \Omega \in \{\alpha, \beta, \gamma\}, \\
&\tilde{p}_\Omega = \frac{1}{I\omega} p_\Omega.
\end{aligned} \tag{5.31}$$

Based on the above definition, the equation of motion is of order unity, and the time derivative is from $\dot{t}$ to $\omega\dot{\tilde{t}}$, and for a white noise term W_i becomes $\eta_i = W_i/\sqrt{\omega}$ in dimensionless units. The parameter ω is a free timescale parameter which we just choose $\omega = \omega_\alpha$ for the timescale of librations.

The constant time parameter τ in Equation (5.18) follows $0 < \tau < 1/(2f_\Omega)$ for the librational modes with librational frequency $f_{\{\alpha,\beta\}}$. In order to implement the simulation more efficiently for the particle to reach a steady state with less number

of timesteps, we choose $\tau = 0.7 \times (1/(2f_\Omega))$ in our simulation. The dimensionless timestep $\Delta\tilde{t}$ is chosen as 1×10^{-3} for the total dimensionless time period $\tilde{T} > 250$.

We also consider the measurement error of angular position and librational motion detection in the real experimental condition. This is treated by adding a measurement noise term to the $\Omega \in \{\alpha, \beta\}$ and their time derivatives (e.g., angular speeds). In detail, a random sequence $\{\delta\alpha_i, \delta\beta_i, \delta\dot{\alpha}_i, \delta\dot{\beta}_i\}$ (here i denotes the iteration number in the discretised form) is initiated following a Gaussian distribution with zero mean and an adjustable standard deviation $\sigma_{\alpha,\beta}$. The different measurement errors will lead to different steady-state energies.

Accordingly, the parameterized Equation (5.18) for polarisation feedback becomes:

$$\begin{aligned} \varphi_i &= (\alpha_i + \delta\alpha_i) - \tau\left[(\dot{\alpha}_i + \delta\dot{\alpha}_i) - (\dot{\beta}_i + \delta\dot{\beta}_i)\right] \quad \text{for } p_\gamma > 0, \\ \varphi_i &= (\alpha_i + \delta\alpha_i) - \tau\left[(\dot{\alpha}_i + \delta\dot{\alpha}_i) + (\dot{\beta}_i + \delta\dot{\beta}_i)\right] \quad \text{for } p_\gamma < 0. \end{aligned} \tag{5.32}$$

During the implementation of polarisation feedback cooling, the nanorod is regarded as deeply trapped by the linearly polarised light field such that their translational motion is uncoupled and ignored in the simulation.

For the initial states of $\tilde{\alpha}$ & $\tilde{\beta}$, they are following Gaussian distributions with a zero mean for α, $\pi/2$ mean for β and a standard deviation of $\Delta\alpha_{\text{initial}} = \Delta\beta_{\text{initial}}$ for all possible angular positions. The initial angular momenta also follow independent Gaussian distributions with zero mean and a standard deviation of $\Delta\tilde{p}_\alpha = \Delta\tilde{p}_\beta = \sqrt{k_\text{B}T_\text{b}/(I\omega^2)}$. These settings are consistent with the deeply trapped regime.

5.3.4 Simulation results

In the following results, we simulate a levitated silicon nanorod with 600 nm long and 100 nm diameter trapped by two counter-propagating laser beams with the wavelength of $\lambda = 1550$ nm and total optical power of $P_{\text{opt}} = 200$ mW. Two beams are focused by a pair of lenses with NA = 0.43. According to the parameters acquired in our previous experiments, we use a beam waist of $w_0 = 6.8$ μm. The bath temperature T_b is set as room temperature 298 K, and the pressure is $P_{\text{gas}} = 0.1$ mbar.

Figure 5.7 shows an example of five random initial dimensionless angular positions $\tilde{\alpha}$ & $\tilde{\beta}$ and independent random dimensionless angular momenta $\tilde{p}_\alpha$ & $\tilde{p}_\beta$. The initial dimensionless $\tilde{\gamma}$ is 0, and $\tilde{p}_\gamma$ is set to 0.1. After about 120 rounds of librational oscillations ($\tilde{t} > 120$), both $\tilde{\alpha}$ & $\tilde{\beta}$ reaches a new steady-state with minimum angular momenta $\tilde{p}_\alpha$ & $\tilde{p}_\beta$ close to zero, demonstrating optically cooled angular energy of the levitated librator. In terms of the degree of freedom $\tilde{\gamma}$, it remains untouched with a constant $\tilde{p}_\gamma = 0.1$ as predicted. It is also interesting to notice that β always aligns to $\pi/2$ no matter what initial angles for the minimum potential of β-direction with a linearly polarised light field.

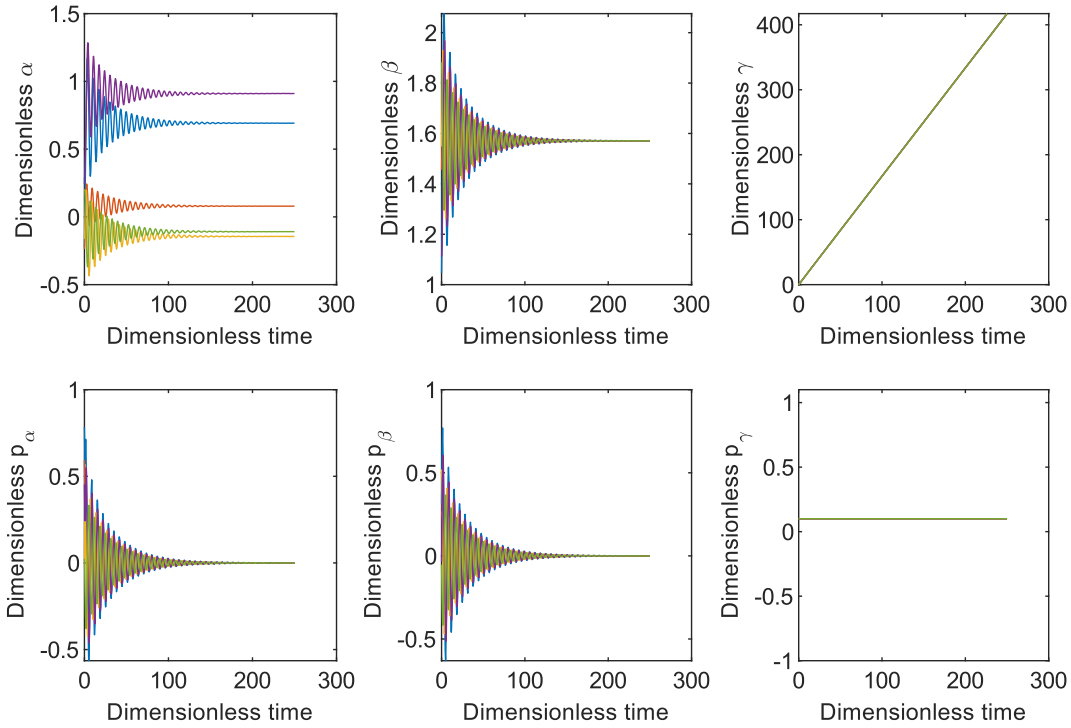

Figure 5.7: Simulated dynamics of librational modes and the evolution of angular momenta under the implementation of polarisation feedback cooling from $\tilde{t} = 0$. All the axes are in dimensionless units. Five different colours represent five random initial dimensionless angular positions $\tilde{\alpha}$ & $\tilde{\beta}$ and independent random dimensionless angular momenta $\tilde{p}_\alpha$ & $\tilde{p}_\beta$. The initial dimensionless $\tilde{\gamma}$ is 0, and $\tilde{p}_\gamma$ is set to 0.1. After about 120 rounds of librational oscillations ($\tilde{t} > 120$), all $\tilde{\alpha}$ & $\tilde{\beta}$ reaches a new steady-state with minimum angular momenta $\tilde{p}_\alpha$ & $\tilde{p}_\beta$, demonstrating optically cooled angular energy of the levitated librator. For the degree of freedom $\tilde{\gamma}$, it still keeps untouched with a constant $\tilde{p}_\gamma = 0.1$.

From the dynamics of the levitated nanoparticle, we can analyse the change of energy of the levitated mechanical librator after the implementation of polarisation feedback. As discussed in the previous section, we calculate the new steady-state energy E_{tot} above the potential minimum V_{min} and the minimum possible energy E_{min} in every timestep. The former is potential energy in the scenario where the nanorod is perfectly aligned with the polarisation direction of the trapping beam; while the latter is the minimum potential energy adding the energy of γ-motion which is the only motion that cannot be controlled in our scheme.

Figure 5.8 shows an example of the time evolution of the energy change of the levitated librator with five different initial states shown in Figure 5.7. We can see that the librational energy and total energy decrease with time to approach zero, which implies both α and β degrees of freedom are cooled and only leave γ untouched.

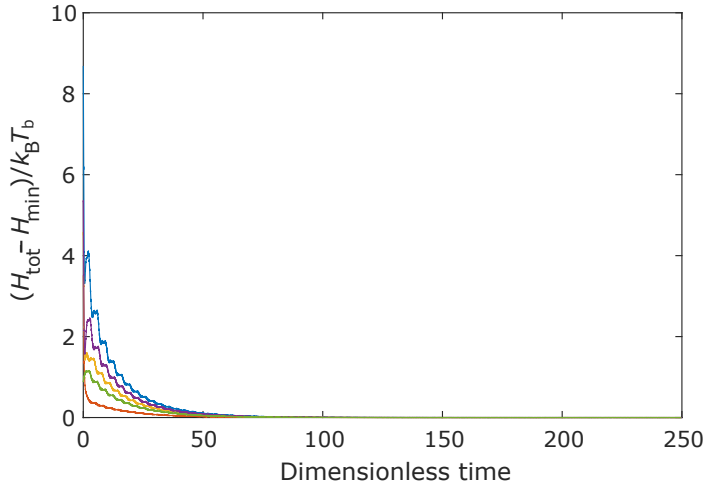

Figure 5.8: The time evolution of the energy change of the levitated librator with five initial states shown in the previous figure. Under the implementation of polarisation feedback cooling, the total Hamiltonian $\mathcal{H}_{\mathrm{tot}}$ is decreased to the possible minimum Hamiltonian of the system $\mathcal{H}_{\mathrm{min}}$.

Since the initial states are set to be stochastic, we run the simulations for 150 tails to verify the cooling effect of this cooling method and calculate the averaged energy and its standard deviations. Figure 5.9 and 5.10 show the averaged steady-state energy above the minimum potential and the minimum total energy after a period of $\tilde{T} = 1500$. From the simulation results, $\langle E_{\mathrm{tot}} - E_{\mathrm{min}} \rangle$ is independent on

p_γ shown in Figure 5.10, while $\langle E_{\text{tot}} - V_{\text{min}} \rangle$ is dependent on p_γ^2 in Figure 5.9 as expected in Equation (5.9).

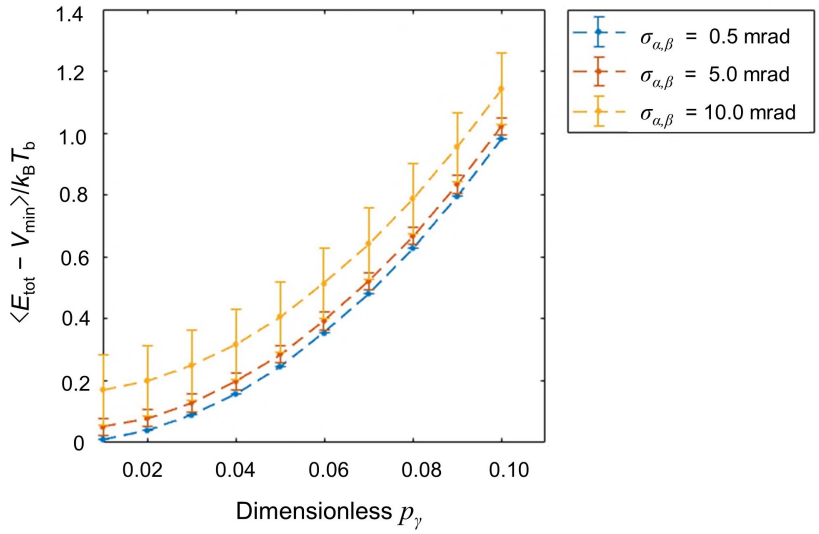

Figure 5.9: Averaged final total energy above the minimum potential $\langle E_{\text{tot}} - V_{\text{min}} \rangle$ with respect to different $\tilde{p}_\gamma$ after a period of $\tilde{T} = 1500$. There different measurement error $\sigma_{\alpha,\beta} = 0.5, 5.0, 10.0$ mrad are added during the simulation. Error bars represent the standard deviation of the averaged energy obtained.

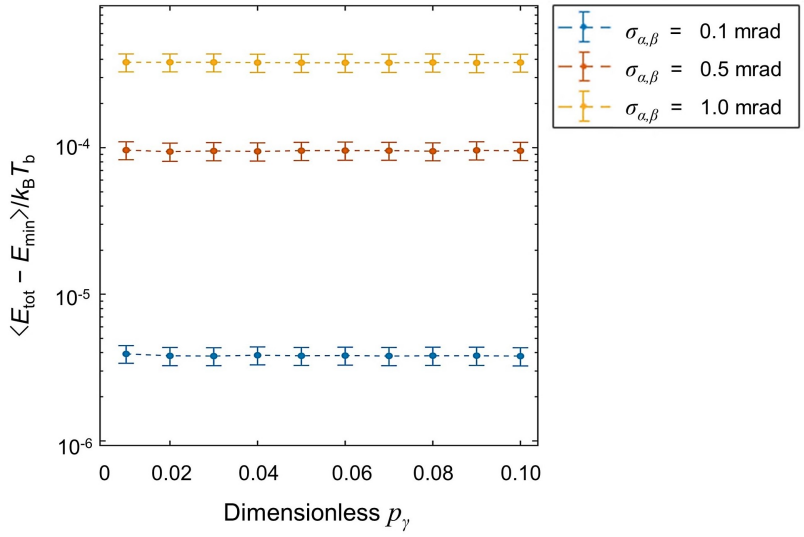

Figure 5.10: Averaged final total energy above the minimum energy $\langle E_{\text{tot}} - E_{\text{min}} \rangle$ with respect to different dimensionless angular momentum $\tilde{p}_\gamma$ after a period of $\tilde{T} = 1500$. There different measurement error $\sigma_{\alpha,\beta} = 0.1, 0.5, 1.0$ mrad are added during the simulation.

As plotted in Figure 5.11, the achieved lowest energy above the minimum energy is in the order of magnitude of 10^{-4}, 10^{-5} and 10^{-6} $k_{\mathrm{B}}T_{\mathrm{b}}$ for the measurement error $\sigma_{\alpha,\beta} = 0.1, 0.5, 1.0$ mrad respectively, corresponding to the effective temperature of 10^{-2}, 10^{-3} and 10^{-4} K, demonstrating an effective cooling of the librational motion.

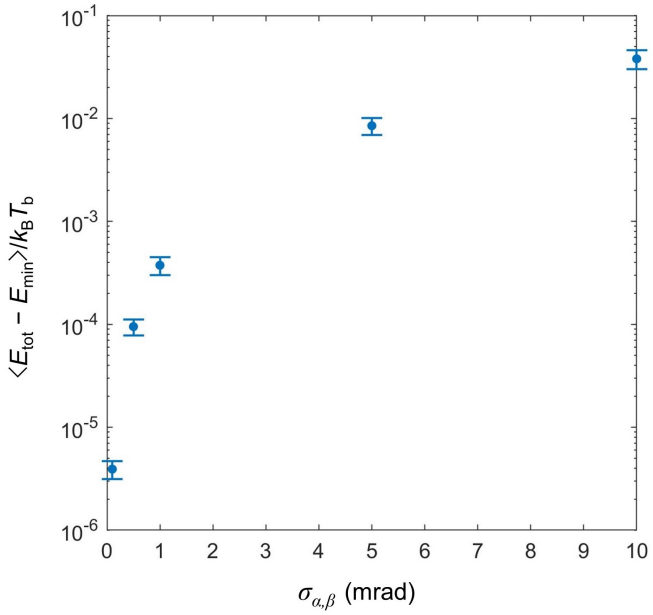

Figure 5.11: The achievable lowest energy above the minimum energy with respect to different measurement errors. Five different measurement errors with the standard deviation $\sigma_{\alpha,\beta} = 0.1$, 0.5, 1.0, 5.0, 10.0 mrad are simulated with stochastic initial states. The dimensionless angular momentum $\tilde{p}_{\gamma}$ is set to 0.05.

5.4 Ro-translational optomechanical cooling limits

In this section, we discuss the ro-translational cooling limits based on the previously introduced feedback cooling methods.

Towards to quantum regime, the motion of levitated mechanical oscillator is required to be cooled near or within its ground state with the mean occupation number $\bar{n} < 1$. Heisenberg's uncertainty relation imposes a lower bound for the product with $\delta x\, \delta p \geq \hbar/2$. In feedback cooling, the position (or angular position)

information of particles must be measured for implementation of the feedback loop, thus measurement accuracy of these quantities fundamentally limits the lowest achievable temperatures following the uncertainty principle. This also means the dissipation mechanism in the system needs to be considered and reduced.

In the levitated optomechanical system, the position fluctuations arising from the thermal dissipation of surrounding gas molecules become negligible at low pressures; however, the recoil heating starts to become the dominating decoherence noise source. Here, we only consider the cooling limits set by the measurement imprecision and measurement backaction in this scenario.

The imprecision of position (angular position) measurement is determined by the shot noise (torque shot noise) [105]:

$$\langle \hat{x}^2 \rangle_{\text{imprecision}} = \frac{\hbar\nu}{2k^2\eta_{\text{det}}\lambda_i}\frac{1}{P_{\text{scat}}}\frac{1}{\Delta t}, \tag{5.33}$$

where η_{det} denotes the detection efficiency with the limits of $\eta_{\text{det}} = 1$ for an ideal maximum detection efficiency, λ_i accounts for the geometric distribution of the dipole radiation field, P_{scat} is the scattered light power and Δt is the measurement time.

From this equation, higher precision measurement of the particle's motion can be obtained by increasing the photon numbers; however, this leads to a larger measurement backaction due to photon recoil heating [26]:

$$\langle \hat{x}^2 \rangle_{\text{backaction}} = \frac{\lambda_i\hbar\nu}{M\omega_m^2}\frac{1}{\Gamma_{\text{tot}}^2}\frac{P_{\text{scat}}}{2Mc^2}\frac{1}{\Delta t}, \tag{5.34}$$

where Γ_{tot} is the total damping rate including the feedback damping Γ_{fb}.

The standard quantum limit is achieved when the measurement imprecision and backaction contribute equally, yielding a minimum energy given by the imprecision-backaction product. In the configuration of our experiments, increasing measurement efficiency with lower photon numbers is an important next step to achieve better cooling performance and lower energy of levitated mechanical oscillators.

Chapter 6

Conclusion and Outlook

6.1 Conclusion

The fascinating research topic on the quantum control and measurement of mechanical systems has been generating wide interest in the research community. Nanoparticles levitated in high vacuum are a promising platform for exploiting the transition between the classical and quantum world, in an unexplored regime with macroscopic mass and size, which has profound implications for our understanding of nature. Meanwhile, the exquisite control of all degrees of freedom of levitated optomechanical oscillators enables the rapid and vast development of technological applications.

Ro-translational dynamics of mechanical oscillators in the quantum regime are promising to observe pronounced quantum phenomena and develop quantum-enhanced technologies. In this thesis, we have discussed an experimental platform established for studying the ro-translational optomechanics of levitated nanoparticles. For the loading method, direct loading in vacuum is one of the challenges for optical trapping, we demonstrated an efficient loading technique in vacuum based on LIAD, which enriches the toolbox. We show the control of full rotations of levitated nanoparticles via the transfer of spin angular momentum and a novel way of transferring transverse orbit angular momentum. The exquisite control of nanoscale rotations provides promising routes towards explorations of quantum rotational effect and benchmarks the ultra-precise sensing technologies. In the last

part of this thesis, we focus on the feedback cooling methods on ro-translational motion, paving the way for the next macroscopic quantum experiments.

We hope the work presented in this thesis can contribute to overcoming some existing challenges for the levitated optomechanical system to prepare, manipulate and measure quantum states with control of more degrees of freedom. This optomechanical platform is also appealing for further studies on quantum measurements and realizable sensing applications.

6.2 Outlook

6.2.1 Quantum rotations experiments

Quantum rotations of levitated nanoparticles offer another promising route towards exploring macroscopic quantum physics in an unexplored regime. The free rigid-body rotations can exhibit some pronounced non-linear and non-harmonic quantum effects which do not have classical analogues [44]. With the advantage of these unique properties, we can exploit such rotational quantum phenomena in different schemes. Apart from the proposal of observing orientational quantum revivals discussed in the Introduction, an alternative approach based on quantum-persistent tennis-racket rotations of an asymmetric rotor has been proposed [155], which is predicted to observe quantum tennis-racket flips considering quantum tunnelling and above-barrier reflection in the quantum realm. Other proposals based on spin-rotational coupling for spin-stabilization levitation with levitated magnets also provide another way to study quantum rotations [156] and quantum interference [157].

6.2.2 Further sensing applications

Quantum-enhanced sensing motivated by the advances in levitated optomechanical systems has been used in many fields [158]. In terms of the rotational dynamics of nanorotors, quantum-enhanced torque sensing at and beyond the standard quantum limit can be achieved once nanorotors have been prepared in the quantum regime. Current state-of-art ultrasensitive torque sensor achieved an unprecedented torque sensitivity at the order of magnitude 10^{-27} $\mathrm{NmHz}^{-1/2}$, which is

proposed for detecting the Casimir effect by levitating a nanorotor close to a surface [63]. The levitated ferromagnetic rotors can be used to implement quantum-limited measurements of external magnetic fields [159, 160]. In addition, sensing static electromagnetic fields become conceivable by using interactions with rotational superposition states of polar or magnetized nanorotors. The theoretical predicted spatial resolution of can be achieved on the order of mV m^{-1}, and corresponding torque on the order of 10^{-30} Nm [44, 88].

Appendix A

Calibration and control of polarisation state of light

In terms of anisotropic particles, the polarisation state of light has a great influence on the optical potential, thus it is crucial to calibrate and control the polarisation within the trap. A low-loss, high-speed EOM is used for setting arbitrary polarisation states. To form a standing wave and ensure the polarisation in each arm is identical, the EOM must be calibrated, and two fibre polarisation control paddles are placed in front of the optical trap for setting the initial polarisation state and phase compensation by applied stresses on the single mode fibre.

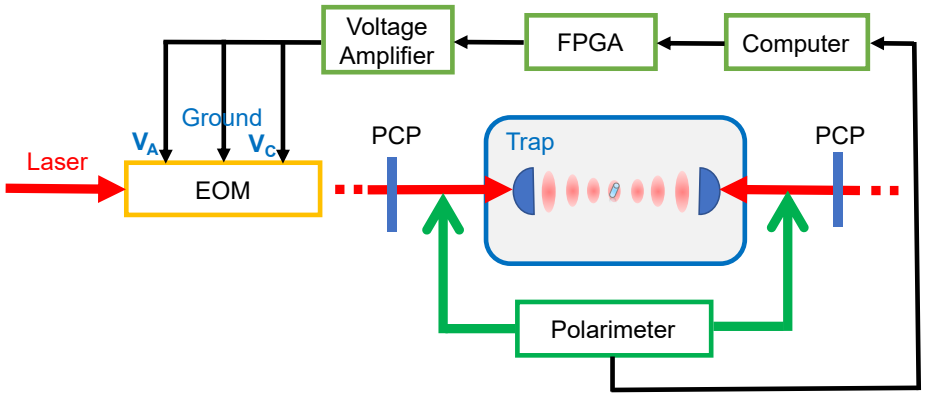

Figure A.1: Optical setup for calibrating the polarisation of the trapping light.

The optical set-up for calibrating the polarisation state is illustrated as Figure A.1. The EOM is controlled by three input voltages (i.e., V_{A}, V_{B} = Ground and V_{C}). With different control of voltages V_{A} and V_{C}, the EOM changes the polarisa-

tion state. The calibration process is automatized in a LabVIEW programme, as shown in Figure A.2. In every step, the control voltage V_A and V_C change a step size (e.g., 0.01 V), then the polarimeter (Thorlabs PAX1000IR1) measures the polarisation state which is recorded by the FPGA module (National Instruments, PXIe-7847). The full range of V_A and V_C is from -10 V to +10 V.

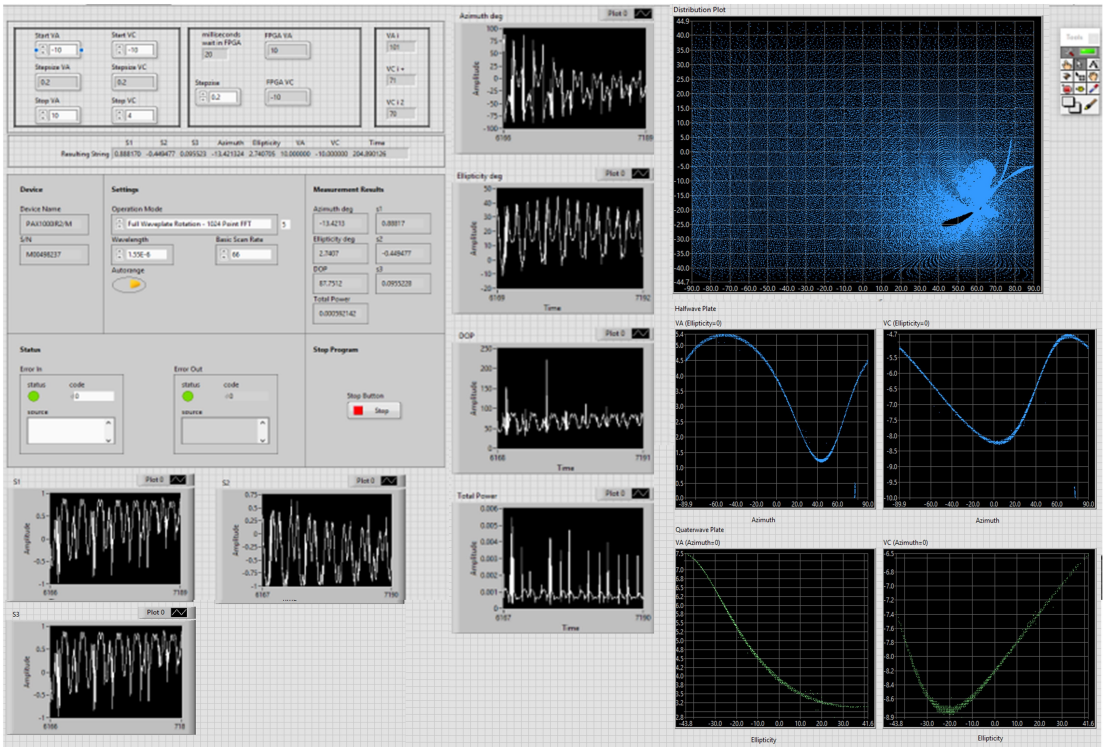

Figure A.2: The LabVIEW programme interface for calibrating the polarisation state. This programme integrates the readout from the polarimeter and the voltage control of the FPGA analogue output. After a full round of voltage scan and polarisation states data recording, the voltages (V_A and V_C) calibrated for controlling the EOM working as a half-wave plate (blue curve) and a quarter-wave plate (green curve) are filtered out.

Before the automatized calibration process, we can adjust the initial polarisation state in each arm with any applied voltages V_A and V_C. Normally, we set the initial polarisation state in each arm as linearly polarised along x-axis with $V_A = V_C = 0$ by manually adjusting the fibre polarisation control paddles. The set of fibre polarisation control paddles changes the polarisation state of light transmitted in the optical fibre by introducing birefringence induced by stresses and

bending of the fibre. These can be appropriately adjusted to make the polarisation state in each arm behave the same but with opposite handedness, under the same pair of voltages V_A and V_C applied on EOM.

Figure A.3 shows an example of the EOM calibration result. Once the EOM is calibrated, we can set the initial polarisation state in two arms in an arbitrary state by setting corresponding a pair of applied voltages V_A and V_C, which also can be implemented based on the LabVIEW programme shown in Figure A.4.

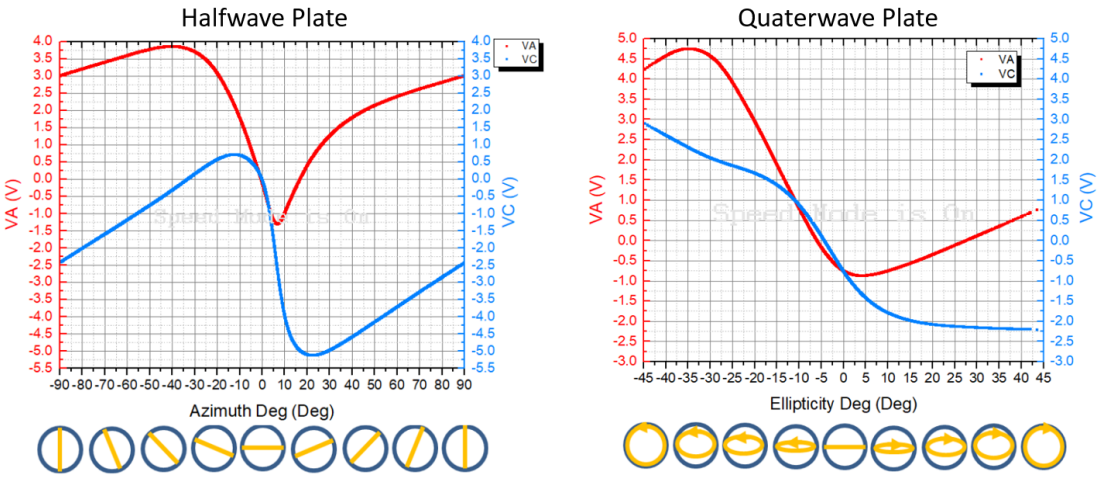

Figure A.3: The calibration results for EOM working as a halfwave plate (left panel) and a quarter-wave plate (right panel) in different pair of control voltages V_A and V_C. The left panel shows the EOM rotates the azimuth degree of an input linearly polarised light, while the right panel shows the EOM changes the polarisation state of an input light from linearly to circularly polarised with different ellipticity degrees.

Figure A.4 presents the LabVIEW interface for setting the polarisation states of the trapping light via a pair of calibrated voltages V_A and V_C. The left upper panel shows the switch between LP and CP with different V_A and V_C outputs from the Analogue outputs (AO0 and AO1) of the NI PXIe FPGA module. The left bottom panel shows the control of the azimuth degree of linear polarisation (i.e., linearly polarisation direction) by inputting the desired value of azimuth degree. The LabVIEW programme can search for the corresponding voltages V_A and V_C via the look-up table function. The right panel shows an example of a linearly and circularly polarised state measured by the polarimeter.

For full rotation experiments, the LabVIEW programme provides a way to switch the polarisation states directly. It also can be connected to an arbitrary function generator to generate arbitrary waveforms or locked to an external clock with fast modulation of polarisation states. In the polarisation feedback experiments, the control voltages V_A and V_C can be real-time modulated according to the feedback signals.

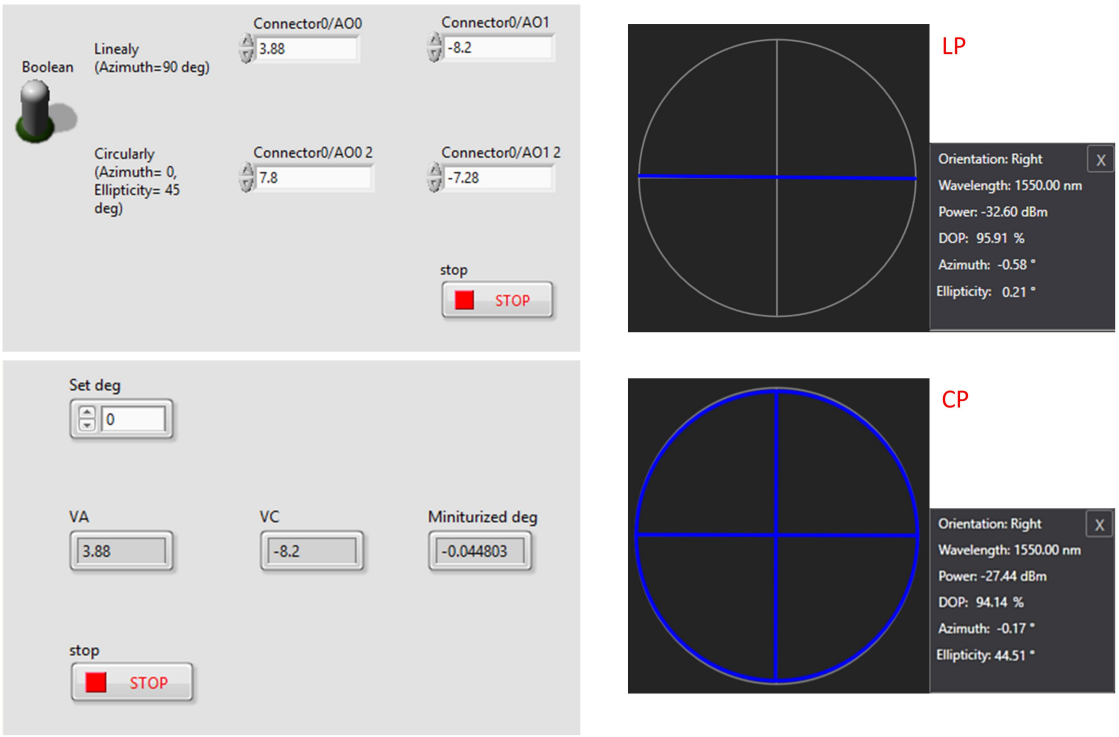

Figure A.4: The LabVIEW interface for setting the polarisation states of the trapping light via a pair of calibrated voltages V_A and V_C. The left upper panel shows the switch between LP and CP with different V_A and V_C output from the Analogue outputs of the FPGA module. The left bottom panel shows the control of the azimuth degree of linear polarisation (i.e., linearly polarisation direction) by inputting the desired value of azimuth degree. The LabVIEW programme will find the corresponding voltages V_A and V_C via Look-up Table (LUT) function. The right panel shows an example of a linearly and circularly polarised state measured by the polarimeter.

Appendix B

Circuit diagrams

Appendix B contains two electronic circuit diagrams designed and utilised for EOM polarisation control and feedback (B.1) and detection of motions of levitated nanoparticles (B.2). These are designed and tested with technical support from Alastair Symon.

B.1 DC amplifier with offset

This circuit is a DC amplifier for doubling the input voltage within ±10 V plus an adjustable offset ranging ±10 V.

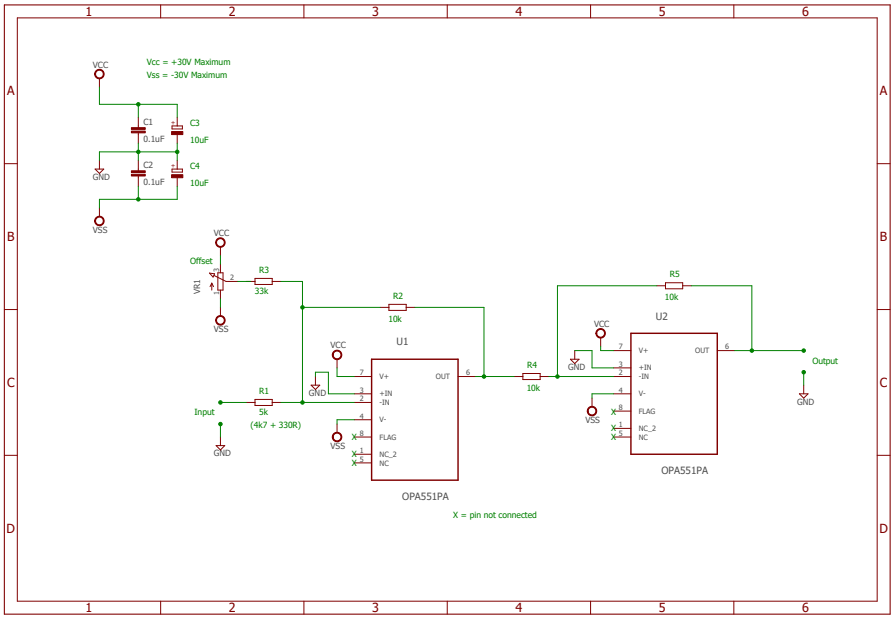

Figure B.1: DC amplifier with offset.

B.2 Quadrant photodetector circuit

This circuit is designed for the low-noise, high bandwidth quadrant photodiode (QPD) (G6849, Hamamatsu Photonics) of four quadrants (A,B,C&D) with three outputs (X,Y&SUM): X=(A+B)-(C+D), Y=(A+D)-(B+C), SUM=A+B+C+D.

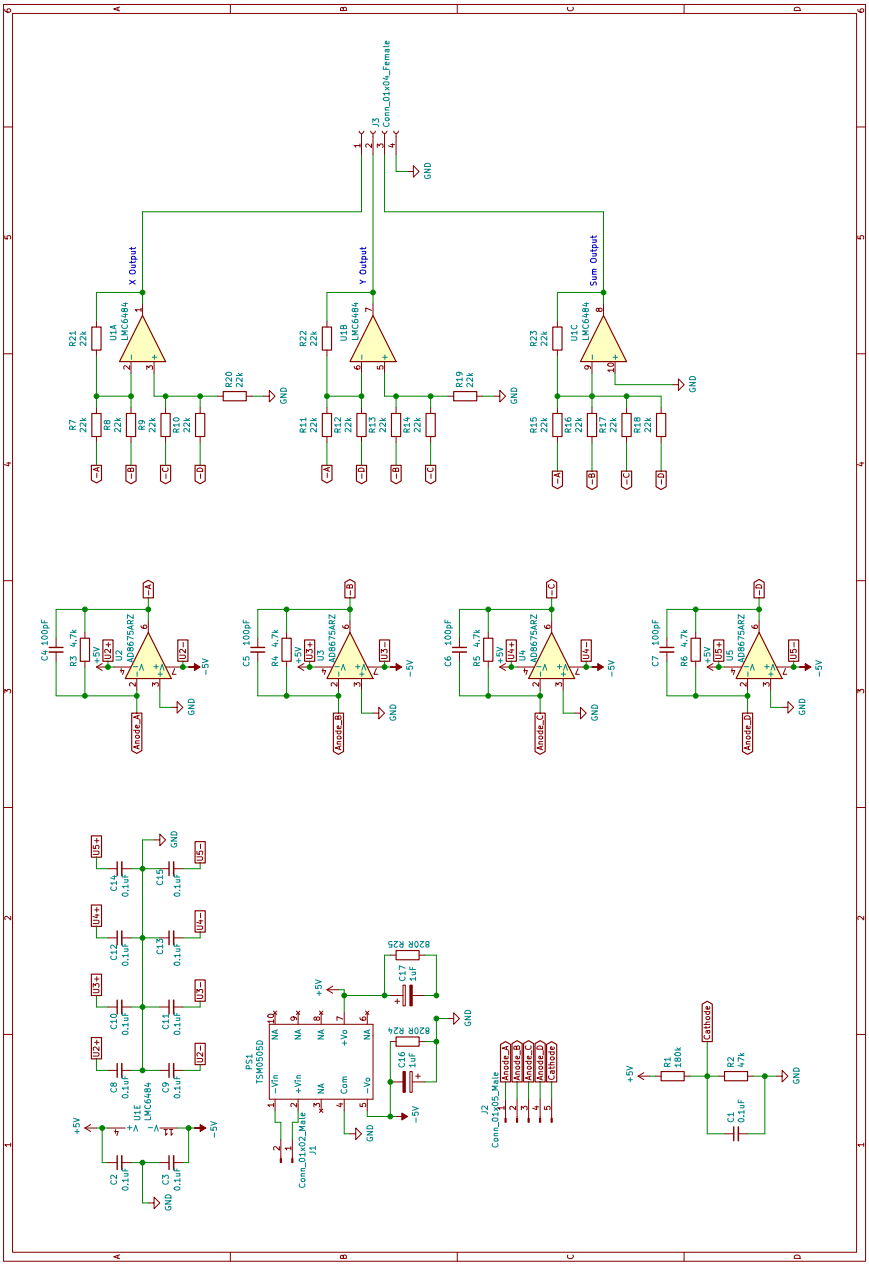

Figure B.2: Circuit diagram for QPD detector.

Bibliography

[1] Anton Zeilinger. Experiment and the foundations of quantum physics. *Reviews of Modern Physics*, 71(2):S288, 1999.

[2] Markus Arndt and Klaus Hornberger. Testing the limits of quantum mechanical superpositions. *Nature Physics*, 10(4):271, 2014.

[3] Florian Marquardt and Steven M Girvin. Optomechanics. *Physics*, 2:40, 2009.

[4] Pierre Meystre. A short walk through quantum optomechanics. *Annalen der Physik*, 525(3):215–233, 2013.

[5] Markus Aspelmeyer, Tobias J Kippenberg, and Florian Marquardt. Cavity optomechanics. *Reviews of Modern Physics*, 86(4):1391, 2014.

[6] Warwick P Bowen and Gerard J Milburn. *Quantum optomechanics*. CRC press, 2015.

[7] James Millen, Tania S Monteiro, Robert Pettit, and A Nick Vamivakas. Optomechanics with levitated particles. *Reports on Progress in Physics*, 83(2):026401, 2020.

[8] James Millen and Benjamin A Stickler. Quantum experiments with microscale particles. *Contemporary Physics*, 61(3):155–168, 2020.

[9] C Gonzalez-Ballestero, M Aspelmeyer, L Novotny, R Quidant, and O Romero-Isart. Levitodynamics: Levitation and control of microscopic objects in vacuum. *Science*, 374(6564):eabg3027, 2021.

[10] Klaus Hornberger, Stefan Gerlich, Philipp Haslinger, Stefan Nimmrichter, and Markus Arndt. Colloquium: Quantum interference of clusters and molecules. *Reviews of Modern Physics*, 84(1):157, 2012.

[11] James Bateman, Stefan Nimmrichter, Klaus Hornberger, and Hendrik Ulbricht. Near-field interferometry of a free-falling nanoparticle from a point-like source. *Nature Communications*, 5:4788, 2014.

[12] Stefan Nimmrichter. *Macroscopic matter wave interferometry*. Springer, 2014.

[13] P F Barker and M N Shneider. Cavity cooling of an optically trapped nanoparticle. *Physical Review A*, 81(2):023826, 2010.

[14] Oriol Romero-Isart, Mathieu L Juan, Romain Quidant, and J Ignacio Cirac. Toward quantum superposition of living organisms. *New Journal of Physics*, 12(3):033015, 2010.

[15] Darrick E Chang, C A Regal, S B Papp, D J Wilson, J Ye, O Painter, H Jeff Kimble, and P Zoller. Cavity opto-mechanics using an optically levitated nanosphere. *Proceedings of the National Academy of Sciences*, 107(3):1005–1010, 2010.

[16] Nikolai Kiesel, Florian Blaser, Uroš Delić, David Grass, Rainer Kaltenbaek, and Markus Aspelmeyer. Cavity cooling of an optically levitated submicron particle. *Proceedings of the National Academy of Sciences*, 110(35):14180–14185, 2013.

[17] Peter Asenbaum, Stefan Kuhn, Stefan Nimmrichter, Ugur Sezer, and Markus Arndt. Cavity cooling of free silicon nanoparticles in high vacuum. *Nature Communications*, 4(1):1–7, 2013.

[18] J Millen, P Z G Fonseca, T Mavrogordatos, T S Monteiro, and P F Barker. Cavity cooling a single charged levitated nanosphere. *Physical Review Letters*, 114(12):123602, 2015.

[19] P Z G Fonseca, E B Aranas, J Millen, T S Monteiro, and P F Barker. Nonlinear dynamics and strong cavity cooling of levitated nanoparticles. *Physical Review Letters*, 117(17):173602, 2016.

[20] Dominik Windey, Carlos Gonzalez-Ballestero, Patrick Maurer, Lukas Novotny, Oriol Romero-Isart, and René Reimann. Cavity-based 3d cooling of a levitated nanoparticle via coherent scattering. *Physical Review Letters*, 122(12):123601, 2019.

[21] Uroš Delić, Manuel Reisenbauer, David Grass, Nikolai Kiesel, Vladan Vuletić, and Markus Aspelmeyer. Cavity cooling of a levitated nanosphere by coherent scattering. *Physical Review Letters*, 122(12):123602, 2019.

[22] Uroš Delić, Manuel Reisenbauer, Kahan Dare, David Grass, Vladan Vuletić, Nikolai Kiesel, and Markus Aspelmeyer. Cooling of a levitated nanoparticle to the motional quantum ground state. *Science*, 367(6480):892–895, 2020.

[23] Tongcang Li, Mark G Raizen, and Simon Kheifets. Millikelvin cooling of an optically trapped microsphere in vacuum. *Nature Physics*, 7(7):527–530, 2011.

[24] Tongcang Li, Simon Kheifets, David Medellin, and Mark G Raizen. Measurement of the instantaneous velocity of a brownian particle. *Science*, 328(5986):1673–1675, 2010.

[25] Jan Gieseler, Bradley Deutsch, Romain Quidant, and Lukas Novotny. Subkelvin parametric feedback cooling of a laser-trapped nanoparticle. *Physical Review Letters*, 109(10):103603, 2012.

[26] Vijay Jain, Jan Gieseler, Clemens Moritz, Christoph Dellago, Romain Quidant, and Lukas Novotny. Direct measurement of photon recoil from a levitated nanoparticle. *Physical Review Letters*, 116(24):243601, 2016.

[27] Felix Tebbenjohanns, Martin Frimmer, Andrei Militaru, Vijay Jain, and Lukas Novotny. Cold damping of an optically levitated nanoparticle to microkelvin temperatures. *Physical Review Letters*, 122(22):223601, 2019.

[28] Felix Tebbenjohanns, Martin Frimmer, Vijay Jain, Dominik Windey, and Lukas Novotny. Motional sideband asymmetry of a nanoparticle optically levitated in free space. *Physical Review Letters*, 124(1):013603, 2020.

[29] Lorenzo Magrini, Philipp Rosenzweig, Constanze Bach, Andreas Deutschmann-Olek, Sebastian G Hofer, Sungkun Hong, Nikolai Kiesel, Andreas Kugi, and Markus Aspelmeyer. Real-time optimal quantum control of mechanical motion at room temperature. *Nature*, 595(7867):373–377, 2021.

[30] Felix Tebbenjohanns, M Luisa Mattana, Massimiliano Rossi, Martin Frimmer, and Lukas Novotny. Quantum control of a nanoparticle optically levitated in cryogenic free space. *Nature*, 595(7867):378–382, 2021.

[31] Jan Gieseler, Romain Quidant, Christoph Dellago, and Lukas Novotny. Dynamic relaxation of a levitated nanoparticle from a non-equilibrium steady state. *Nature Nanotechnology*, 9(5):358, 2014.

[32] Jan Gieseler, Marko Spasenović, Lukas Novotny, and Romain Quidant. Nonlinear mode coupling and synchronization of a vacuum-trapped nanoparticle. *Physical Review Letters*, 112(10):103603, 2014.

[33] Thai M Hoang, Rui Pan, Jonghoon Ahn, Jaehoon Bang, HT Quan, and Tongcang Li. Experimental test of the differential fluctuation theorem and a generalized jarzynski equality for arbitrary initial states. *Physical Review Letters*, 120(8):080602, 2018.

[34] Christian L Degen, F Reinhard, and P Cappellaro. Quantum sensing. *Reviews of Modern Physics*, 89(3):035002, 2017.

[35] Levi P Neukirch and A Nick Vamivakas. Nano-optomechanics with optically levitated nanoparticles. *Contemporary Physics*, 56(1):48–62, 2015.

[36] David C Moore and Andrew A Geraci. Searching for new physics using optically levitated sensors. *Quantum Science and Technology*, 6(1):014008, 2021.

[37] Andrew A Geraci, Scott B Papp, and John Kitching. Short-range force detection using optically cooled levitated microspheres. *Physical Review Letters*, 105(10):101101, 2010.

[38] Gambhir Ranjit, David P Atherton, Jordan H Stutz, Mark Cunningham, and Andrew A Geraci. Attonewton force detection using microspheres in a dual-beam optical trap in high vacuum. *Physical Review A*, 91(5):051805, 2015.

[39] David Hempston, Jamie Vovrosh, Marko Toroš, George Winstone, Muddassar Rashid, and Hendrik Ulbricht. Force sensing with an optically levitated charged nanoparticle. *Applied Physics Letters*, 111(13):133111, 2017.

[40] T S Monteiro, J Millen, G A T Pender, Florian Marquardt, D Chang, and P F Barker. Dynamics of levitated nanospheres: towards the strong coupling regime. *New Journal of Physics*, 15(1):015001, 2013.

[41] Gadi Afek, Daniel Carney, and David C Moore. Coherent scattering of low mass dark matter from optically trapped sensors. *Physical Review Letters*, 128(10):101301, 2022.

[42] Peiran Yin, Rui Li, Chengjiang Yin, Xiangyu Xu, Xiang Bian, Han Xie, Chang-Kui Duan, Pu Huang, Jian-hua He, and Jiangfeng Du. Experiments with levitated force sensor challenge theories of dark energy. *Nature Physics*, 18(10):1181–1185, 2022.

[43] Nancy Aggarwal, George P Winstone, Mae Teo, Masha Baryakhtar, Shane L Larson, Vicky Kalogera, and Andrew A Geraci. Searching for new physics with a levitated-sensor-based gravitational-wave detector. *Physical Review Letters*, 128(11):111101, 2022.

[44] Benjamin A Stickler, Klaus Hornberger, and M S Kim. Quantum rotations of nanoparticles. *Nature Reviews Physics*, 3(8):589–597, 2021.

[45] Graham D Bruce, Paloma Rodríguez-Sevilla, and Kishan Dholakia. Initiating revolutions for optical manipulation: the origins and applications of rotational dynamics of trapped particles. *Advances in Physics: X*, 6(1):1838322, 2021.

[46] Christiane P Koch, Mikhail Lemeshko, and Dominique Sugny. Quantum control of molecular rotation. *Reviews of Modern Physics*, 91(3):035005, 2019.

[47] Onofrio M Maragò, Philip H Jones, Pietro G Gucciardi, Giovanni Volpe, and Andrea C Ferrari. Optical trapping and manipulation of nanostructures. *Nature Nanotechnology*, 8(11):807, 2013.

[48] Susan E Skelton Spesyvtseva and Kishan Dholakia. Trapping in a material world. *ACS Photonics*, 3(5):719–736, 2016.

[49] Jan Gieseler, Juan Ruben Gomez-Solano, Alessandro Magazzù, Isaac Pérez Castillo, Laura Pérez García, Marta Gironella-Torrent, Xavier Viader-Godoy, Felix Ritort, Giuseppe Pesce, Alejandro V Arzola, et al. Optical tweezers—from calibration to applications: a tutorial. *Advances in Optics and Photonics*, 13(1):74–241, 2021.

[50] V Garcés-Chávez, D McGloin, MJ Padgett, W Dultz, H Schmitzer, and K Dholakia. Observation of the transfer of the local angular momentum

density of a multiringed light beam to an optically trapped particle. *Physical review letters*, 91(9):093602, 2003.

[51] Konstantin Y Bliokh, Francisco J Rodríguez-Fortuño, Franco Nori, and Anatoly V Zayats. Spin–orbit interactions of light. *Nature Photonics*, 9(12):796–808, 2015.

[52] Thai M Hoang, Yue Ma, Jonghoon Ahn, Jaehoon Bang, F Robicheaux, Zhang-Qi Yin, and Tongcang Li. Torsional optomechanics of a levitated nonspherical nanoparticle. *Physical Review Letters*, 117(12):123604, 2016.

[53] Stefan Kuhn, Alon Kosloff, Benjamin A Stickler, Fernando Patolsky, Klaus Hornberger, Markus Arndt, and James Millen. Full rotational control of levitated silicon nanorods. *Optica*, 4(3):356–360, 2017.

[54] René Reimann, Michael Doderer, Erik Hebestreit, Rozenn Diehl, Martin Frimmer, Dominik Windey, Felix Tebbenjohanns, and Lukas Novotny. GHz rotation of an optically trapped nanoparticle in vacuum. *Physical Review Letters*, 121(3):033602, 2018.

[55] Jonghoon Ahn, Zhujing Xu, Jaehoon Bang, Yu-Hao Deng, Thai M Hoang, Qinkai Han, Ren-Min Ma, and Tongcang Li. Optically levitated nanodumbbell torsion balance and GHz nanomechanical rotor. *Physical Review Letters*, 121(3):033603, 2018.

[56] Muddassar Rashid, Marko Toroš, Ashley Setter, and Hendrik Ulbricht. Precession motion in levitated optomechanics. *Physical Review Letters*, 121(25):253601, 2018.

[57] Yoshihiko Arita, Michael Mazilu, and Kishan Dholakia. Laser-induced rotation and cooling of a trapped microgyroscope in vacuum. *Nature communications*, 4(1):1–7, 2013.

[58] Yoshihiko Arita, Joseph M Richards, Michael Mazilu, Gabriel C Spalding, Susan E Skelton Spesyvtseva, Derek Craig, and Kishan Dholakia. Rotational dynamics and heating of trapped nanovaterite particles. *ACS Nano*, 10(12):11505–11510, 2016.

[59] A T M Anishur Rahman and P F Barker. Laser refrigeration, alignment and rotation of levitated Yb3+:YLF nanocrystals. *Nature Photonics*, 11(10):634, 2017.

[60] Fernando Monteiro, Sumita Ghosh, Elizabeth C van Assendelft, and David C Moore. Optical rotation of levitated spheres in high vacuum. *Physical Review A*, 97(5):051802, 2018.

[61] Yuanbin Jin, Jiangwei Yan, Shah Jee Rahman, Jie Li, Xudong Yu, and Jing Zhang. 6 GHz hyperfast rotation of an optically levitated nanoparticle in vacuum. *Photonics Research*, 9(7):1344–1350, 2021.

[62] Stefan Kuhn, Benjamin A Stickler, Alon Kosloff, Fernando Patolsky, Klaus Hornberger, Markus Arndt, and James Millen. Optically driven ultra-stable nanomechanical rotor. *Nature Communications*, 8(1):1670, 2017.

[63] Jonghoon Ahn, Zhujing Xu, Jaehoon Bang, Peng Ju, Xingyu Gao, and Tongcang Li. Ultrasensitive torque detection with an optically levitated nanorotor. *Nature Nanotechnology*, 15(2):89–93, 2020.

[64] Alejandro Manjavacas and FJ Garcia De Abajo. Thermal and vacuum friction acting on rotating particles. *Physical Review A*, 82(6):063827, 2010.

[65] Rongkuo Zhao, Alejandro Manjavacas, F Javier Garcia de Abajo, and J B Pendry. Rotational quantum friction. *Physical Review Letters*, 109(12):123604, 2012.

[66] Alejandro Manjavacas, Francisco J Rodríguez-Fortuño, F Javier García De Abajo, and Anatoly V Zayats. Lateral casimir force on a rotating particle near a planar surface. *Physical Review Letters*, 118(13):133605, 2017.

[67] Stefan Kuhn. *Cooling and manipulating the ro-translational motion of dielectric particles in high vacuum*. PhD thesis, University of Vienna, 2017.

[68] K-K Ni, S Ospelkaus, M H G de Miranda, A Pe'Er, B Neyenhuis, J J Zirbel, S Kotochigova, P S Julienne, D S Jin, and Jun Ye. A high phase-space-density gas of polar molecules. *Science*, 322(5899):231–235, 2008.

[69] Alexander Prehn, Martin Ibrügger, Rosa Glöckner, Gerhard Rempe, and Martin Zeppenfeld. Optoelectrical cooling of polar molecules to submillikelvin temperatures. *Physical Review Letters*, 116(6):063005, 2016.

[70] John L Bohn, Ana Maria Rey, and Jun Ye. Cold molecules: Progress in quantum engineering of chemistry and quantum matter. *Science*, 357(6355):1002–1010, 2017.

[71] Benjamin A Stickler, Stefan Nimmrichter, Lukas Martinetz, Stefan Kuhn, Markus Arndt, and Klaus Hornberger. Rotranslational cavity cooling of dielectric rods and disks. *Physical Review A*, 94(3):033818, 2016.

[72] T Seberson and F Robicheaux. Parametric feedback cooling of rigid body nanodumbbells in levitated optomechanics. *Physical Review A*, 99(1):013821, 2019.

[73] Jonas Schäfer, Henning Rudolph, Klaus Hornberger, and Benjamin A Stickler. Cooling nanorotors by elliptic coherent scattering. *Physical Review Letters*, 126(16):163603, 2021.

[74] Henning Rudolph, Jonas Schäfer, Benjamin A Stickler, and Klaus Hornberger. Theory of nanoparticle cooling by elliptic coherent scattering. *Physical Review A*, 103(4):043514, 2021.

[75] Tom Delord, P Huillery, L Nicolas, and G Hétet. Spin-cooling of the motion of a trapped diamond. *Nature*, 580(7801):56–59, 2020.

[76] Fons van der Laan, Felix Tebbenjohanns, René Reimann, Jayadev Vijayan, Lukas Novotny, and Martin Frimmer. Sub-kelvin feedback cooling and heating dynamics of an optically levitated librator. *Physical Review Letters*, 127(12):123605, 2021.

[77] Jaehoon Bang, Troy Seberson, Peng Ju, Jonghoon Ahn, Zhujing Xu, Xingyu Gao, Francis Robicheaux, and Tongcang Li. Five-dimensional cooling and nonlinear dynamics of an optically levitated nanodumbbell. *Physical Review Research*, 2(4):043054, 2020.

[78] Antonio Pontin, Hayden Fu, Marko Toroš, Tania S Monteiro, and Peter F Barker. Simultaneous cooling of all six degrees of freedom of an optically levitated nanoparticle by elliptic coherent scattering. *arXiv preprint arXiv:2205.10193*, 2022.

[79] Arne L Grimsmo, Joshua Combes, and Ben Q Baragiola. Quantum computing with rotation-symmetric bosonic codes. *Physical Review X*, 10(1):011058, 2020.

[80] Victor V Albert, Jacob P Covey, and John Preskill. Robust encoding of a qubit in a molecule. *Physical Review X*, 10(3):031050, 2020.

[81] Stefan Gerlich, Sandra Eibenberger, Mathias Tomandl, Stefan Nimmrichter, Klaus Hornberger, Paul J Fagan, Jens Tüxen, Marcel Mayor, and Markus Arndt. Quantum interference of large organic molecules. *Nature communications*, 2(1):1–5, 2011.

[82] Thomas Juffmann, Adriana Milic, Michael Müllneritsch, Peter Asenbaum, Alexander Tsukernik, Jens Tüxen, Marcel Mayor, Ori Cheshnovsky, and Markus Arndt. Real-time single-molecule imaging of quantum interference. *Nature nanotechnology*, 7(5):297–300, 2012.

[83] Christian Brand, Filip Kiałka, Stephan Troyer, Christian Knobloch, Ksenija Simonović, Benjamin A Stickler, Klaus Hornberger, and Markus Arndt. Bragg diffraction of large organic molecules. *Physical Review Letters*, 125(3):033604, 2020.

[84] Yaakov Y Fein, Philipp Geyer, Patrick Zwick, Filip Kiałka, Sebastian Pedalino, Marcel Mayor, Stefan Gerlich, and Markus Arndt. Quantum superposition of molecules beyond 25 kda. *Nature Physics*, 15(12):1242–1245, 2019.

[85] Stefan Nimmrichter, Klaus Hornberger, Philipp Haslinger, and Markus Arndt. Testing spontaneous localization theories with matter-wave interferometry. *Physical Review A*, 83(4):043621, 2011.

[86] Oriol Romero-Isart, Anika C Pflanzer, Florian Blaser, Rainer Kaltenbaek, Nikolai Kiesel, Markus Aspelmeyer, and J Ignacio Cirac. Large quantum superpositions and interference of massive nanometer-sized objects. *Physical review letters*, 107(2):020405, 2011.

[87] Oriol Romero-Isart. Quantum superposition of massive objects and collapse models. *Physical Review A*, 84(5):052121, 2011.

[88] Benjamin A Stickler, Birthe Papendell, Stefan Kuhn, Björn Schrinski, James Millen, Markus Arndt, and Klaus Hornberger. Probing macroscopic quantum superpositions with nanorotors. *New Journal of Physics*, 20(12):122001, 2018.

[89] Tamar Seideman. Revival structure of aligned rotational wave packets. *Physical Review Letters*, 83(24):4971, 1999.

[90] Mikael D Poulsen, Emmanuel Peronne, Henrik Stapelfeldt, Christer Z Bisgaard, Simon S Viftrup, Edward Hamilton, and Tamar Seideman. Nonadiabatic alignment of asymmetric top molecules: Rotational revivals. *The Journal of Chemical Physics*, 121(2):783–791, 2004.

[91] Arthur Ashkin. Acceleration and trapping of particles by radiation pressure. *Physical Review Letters*, 24(4):156, 1970.

[92] Arthur Ashkin and J M Dziedzic. Optical levitation by radiation pressure. *Applied Physics Letters*, 19(8):283–285, 1971.

[93] Philip H Jones, Onofrio M Maragò, and Giovanni Volpe. *Optical tweezers: Principles and applications*. Cambridge University Press, 2015.

[94] Marlan O Scully and M Suhail Zubairy. *Quantum optics*. Cambridge University Press, 1997.

[95] Hans-A Bachor and Timothy C Ralph. *A guide to experiments in quantum optics*. John Wiley & Sons, 2019.

[96] Lukas Novotny and Bert Hecht. *Principles of nano-optics*. Cambridge University Press, 2012.

[97] James P Gordon. Radiation forces and momenta in dielectric media. *Physical Review A*, 8(1):14, 1973.

[98] Hao Shi and Mishkat Bhattacharya. Optomechanics based on angular momentum exchange between light and matter. *Journal of Physics B: Atomic, Molecular and Optical Physics*, 49(15):153001, 2016.

[99] James Millen and Jan Gieseler. Single particle thermodynamics with levitated nanoparticles. In *Thermodynamics in the Quantum Regime*, pages 853–885. Springer, 2018.

[100] Alan Robert Edmonds. *Angular momentum in quantum mechanics*. Princeton University Press, 1996.

[101] Stephen M Barnett and Rodney Loudon. On the electromagnetic force on a dielectric medium. *Journal of Physics B: Atomic, Molecular and Optical Physics*, 39(15):S671, 2006.

[102] R Schiffer and K O Thielheim. Light scattering by dielectric needles and disks. *Journal of Applied Physics*, 50(4):2476–2483, 1979.

[103] J Millen, T Deesuwan, P Barker, and J Anders. Nanoscale temperature measurements using non-equilibrium brownian dynamics of a levitated nanosphere. *Nature Nanotechnology*, 9(6):425, 2014.

[104] Lukas Martinetz, Klaus Hornberger, and Benjamin A Stickler. Gas-induced friction and diffusion of rigid rotors. *Physical Review E*, 97(5):052112, 2018.

[105] Vijay Jain. *Levitated optomechanics at the photon recoil limit*. PhD thesis, ETH Zurich, 2017.

[106] Pau Mestres, Johann Berthelot, Marko Spasenović, Jan Gieseler, Lukas Novotny, and Romain Quidant. Cooling and manipulation of a levitated nanoparticle with an optical fiber trap. *Applied Physics Letters*, 107(15):151102, 2015.

[107] Massimo Calamai, Andrea Ranfagni, and Francesco Marin. Transfer of a levitating nanoparticle between optical tweezers. *AIP Advances*, 11(2):025246, 2021.

[108] David Grass, Julian Fesel, Sebastian G Hofer, Nikolai Kiesel, and Markus Aspelmeyer. Optical trapping and control of nanoparticles inside evacuated hollow core photonic crystal fibers. *Applied Physics Letters*, 108(22):221103, 2016.

[109] Wen-Ping Peng, Huan-Chang Lin, Ming-Lee Chu, Huan-Cheng Chang, Hsin-Hung Lin, Alice L Yu, and Chung-Hsuan Chen. Charge monitoring cell mass spectrometry. *Analytical Chemistry*, 80(7):2524–2530, 2008.

[110] Ilko Bald, Iwona Dabkowska, and Eugen Illenberger. Probing biomolecules by laser-induced acoustic desorption: Electrons at near zero electron volts trigger sugar- phosphate cleavage. *Angewandte Chemie*, 120(44):8646–8648, 2008.

[111] Dmitry S Bykov, Pau Mestres, Lorenzo Dania, Lisa Schmöger, and Tracy E Northup. Direct loading of nanoparticles under high vacuum into a paul trap for levitodynamical experiments. *Applied Physics Letters*, 115(3):034101, 2019.

[112] Steen Hansen. Translational friction coefficients for cylinders of arbitrary axial ratios estimated by monte carlo simulation. *The Journal of Chemical Physics*, 121(18):9111–9115, 2004.

[113] A Ortega and J Garcıa de la Torre. Hydrodynamic properties of rodlike and disklike particles in dilute solution. *The Journal of Chemical Physics*, 119(18):9914–9919, 2003.

[114] Giorgio Volpe and Giovanni Volpe. Simulation of a brownian particle in an optical trap. *American Journal of Physics*, 81(3):224–230, 2013.

[115] Stefan Kuhn, Peter Asenbaum, Alon Kosloff, Michele Sclafani, Benjamin A Stickler, Stefan Nimmrichter, Klaus Hornberger, Ori Cheshnovsky, Fernando Patolsky, and Markus Arndt. Cavity-assisted manipulation of freely rotating silicon nanorods in high vacuum. *Nano Letters*, 15(8):5604–5608, 2015.

[116] J Millen, S Kuhn, F Patolsky, A Kosloff, and M Arndt. Cooling and manipulation of nanoparticles in high vacuum. In *Optical Trapping and Optical Micromanipulation XIII*, volume 9922, pages 41–48. SPIE, 2016.

[117] Jan Gieseler and James Millen. Levitated nanoparticles for microscopic thermodynamics—a review. *Entropy*, 20(5):326, 2018.

[118] Cui-Hong Li, Jiang Jing, Lei-Ming Zhou, Zhen-Hai Fu, Xiao-Wen Gao, Nan Li, Xing-Fan Chen, and Hui-Zhu Hu. Fast size estimation of single-levitated nanoparticles in a vacuum optomechanical system. *Optics Letters*, 46(18):4614–4617, 2021.

[119] M Kamba, H Kiuchi, T Yotsuya, and K Aikawa. Recoil-limited feedback cooling of single nanoparticles near the ground state in an optical lattice. *Physical Review A*, 103(5):L051701, 2021.

[120] Ayub Khodaee, Kahan Dare, Aisling Johnson, Uroš Delić, and Markus Aspelmeyer. Dry launching of silica nanoparticles in vacuum. *arXiv preprint arXiv:2209.00482*, 2022.

[121] Joyce E Coppock, Pavel Nagornykh, Jacob PJ Murphy, and Bruce E Kane. Phase locking of the rotation of a graphene nanoplatelet to an rf electric field in a quadrupole ion trap. In *Optical Trapping and Optical Micromanipulation XIII*, volume 9922, pages 56–65. SPIE, 2016.

[122] Yoshihiko Arita, Mingzhou Chen, Ewan M Wright, and Kishan Dholakia. Dynamics of a levitated microparticle in vacuum trapped by a perfect vortex beam: three-dimensional motion around a complex optical potential. *Journal of the Optical Society of America B*, 34(6):C14–C19, 2017.

[123] Michael Mazilu, Yoshihiko Arita, Tom Vettenburg, Juan M Auñón, Ewan M Wright, and Kishan Dholakia. Orbital-angular-momentum transfer to optically levitated microparticles in vacuum. *Physical Review A*, 94(5):053821, 2016.

[124] Lei-Ming Zhou, Ke-Wen Xiao, Jun Chen, and Nan Zhao. Optical levitation of nanodiamonds by doughnut beams in vacuum. *Laser & Photonics Reviews*, 11(2):1600284, 2017.

[125] Alejandro Manjavacas and FJ García De Abajo. Vacuum friction in rotating particles. *Physical review letters*, 105(11):113601, 2010.

[126] Konstantin Y Bliokh and Franco Nori. Transverse and longitudinal angular momenta of light. *Physics Reports*, 592:1–38, 2015.

[127] Alison M Yao and Miles J Padgett. Orbital angular momentum: origins, behavior and applications. *Advances in Optics and Photonics*, 3(2):161–204, 2011.

[128] Jincheng Ni, Can Huang, Lei-Ming Zhou, Min Gu, Qinghai Song, Yuri Kivshar, and Cheng-Wei Qiu. Multidimensional phase singularities in nanophotonics. *Science*, 374(6566):eabj0039, 2021.

[129] Miles Padgett and Richard Bowman. Tweezers with a twist. *Nature Photonics*, 5(6):343–348, 2011.

[130] Konstantin Y Bliokh and Franco Nori. Transverse spin of a surface polariton. *Physical Review A*, 85(6):061801, 2012.

[131] Konstantin Y Bliokh, Aleksandr Y Bekshaev, and Franco Nori. Extraordinary momentum and spin in evanescent waves. *Nature Communications*, 5(1):1–8, 2014.

[132] Martin Neugebauer, Thomas Bauer, Andrea Aiello, and Peter Banzer. Measuring the transverse spin density of light. *Physical Review Letters*, 114(6):063901, 2015.

[133] Aleksandr Y Bekshaev, Konstantin Y Bliokh, and Franco Nori. Transverse spin and momentum in two-wave interference. *Physical Review X*, 5(1):011039, 2015.

[134] Andy Chong, Chenhao Wan, Jian Chen, and Qiwen Zhan. Generation of spatiotemporal optical vortices with controllable transverse orbital angular momentum. *Nature Photonics*, 14(6):350–354, 2020.

[135] S W Hancock, S Zahedpour, A Goffin, and H M Milchberg. Free-space propagation of spatiotemporal optical vortices. *Optica*, 6(12):1547–1553, 2019.

[136] Konstantin Y Bliokh and Franco Nori. Spatiotemporal vortex beams and angular momentum. *Physical Review A*, 86(3):033824, 2012.

[137] Andrea Aiello, Norbert Lindlein, Christoph Marquardt, and Gerd Leuchs. Transverse angular momentum and geometric spin hall effect of light. *Physical Review Letters*, 103(10):100401, 2009.

[138] Konstantin Y Bliokh and Franco Nori. Relativistic hall effect. *Physical Review Letters*, 108(12):120403, 2012.

[139] V A Pas' ko, M S Soskin, and M V Vasnetsov. Transversal optical vortex. *Optics Communications*, 198(1-3):49–56, 2001.

[140] Li-Gang Wang, Li-Qin Wang, and Shi-Yao Zhu. Formation of optical vortices using coherent laser beam arrays. *Optics Communications*, 282(6):1088–1094, 2009.

[141] Yagang Zhang, Zhenkun Wu, Kaibo Yang, Peng Li, Feng Wen, and Yuzong Gu. Splitting, generation, and annihilation of phase singularities in non-coaxial interference of bessel–gaussian beams. *Physica Scripta*, 96(12):125105, 2021.

[142] V Svak, O Brzobohatỳ, M Šiler, P Jákl, J Kaňka, P Zemánek, and SH Simpson. Transverse spin forces and non-equilibrium particle dynamics in a circularly polarized vacuum optical trap. *Nature Communications*, 9(1):1–8, 2018.

[143] Qiwen Zhan. Cylindrical vector beams: from mathematical concepts to applications. *Advances in Optics and Photonics*, 1(1):1–57, 2009.

[144] M V Berry and M R Dennis. Phase singularities in isotropic random waves. *Proceedings of the Royal Society of London. Series A: Mathematical, Physical and Engineering Sciences*, 456(2001):2059–2079, 2000.

[145] Andrea Aiello, Peter Banzer, Martin Neugebauer, and Gerd Leuchs. From transverse angular momentum to photonic wheels. *Nature Photonics*, 9(12):789–795, 2015.

[146] John David Jackson. *Classical Electrodynamics*. John Wiley & Sons Inc., Hoboken, 3rd edition, 1999.

[147] Manuel Nieto-Vesperinas. Optical torque: electromagnetic spin and orbital-angular-momentum conservation laws and their significance. *Physical Review A*, 92(4):043843, 2015.

[148] Manuel Nieto-Vesperinas. Optical torque on small bi-isotropic particles. *Optics Letters*, 40(13):3021–3024, 2015.

[149] Lei Wei and Francisco J Rodríguez-Fortuño. Optical multipolar torque in structured electromagnetic fields: On helicity gradient torque, quadrupolar torque, and spin of the field gradient. *Physical Review B*, 105(12):125424, 2022.

[150] Andrei Afanasev, Jack J Kingsley-Smith, Francisco J Rodríguez-Fortuño, and Anatoly V Zayats. Non-diffractive 3D polarisation features of optical vortex beams. *arXiv:2208.08833*, 2022.

[151] Maryam Nikkhou, Yanhui Hu, James A Sabin, and James Millen. Direct and clean loading of nanoparticles into optical traps at millibar pressures. *Photonics*, 8(11):458, 2021.

[152] A Yoshida and T Asakura. Focusing properties of an off-axis gaussian beam. *Optics & Laser Technology*, 11(1):49–54, 1979.

[153] A I Volokitin and B N J Persson. Quantum friction. *Physical Review Letters*, 106(9):094502, 2011.

[154] Gerard P Conangla, Francesco Ricci, Marc T Cuairan, Andreas W Schell, Nadine Meyer, and Romain Quidant. Optimal feedback cooling of a charged levitated nanoparticle with adaptive control. *Physical Review Letters*, 122(22):223602, 2019.

[155] Yue Ma, Kiran E Khosla, Benjamin A Stickler, and M S Kim. Quantum persistent tennis racket dynamics of nanorotors. *Physical Review Letters*, 125(5):053604, 2020.

[156] Cosimo C Rusconi, Vera Pöchhacker, Katja Kustura, J Ignacio Cirac, and Oriol Romero-Isart. Quantum spin stabilized magnetic levitation. *Physical Review Letters*, 119(16):167202, 2017.

[157] Cosimo C Rusconi, Maxime Perdriat, Gabriel Hétet, Oriol Romero-Isart, and Benjamin A Stickler. Spin-controlled quantum interference of levitated nanorotors. *Physical Review Letters*, 129(9):093605, 2022.

[158] Shabir Barzanjeh, André Xuereb, Simon Gröblacher, Mauro Paternostro, Cindy A Regal, and Eva M Weig. Optomechanics for quantum technologies. *Nature Physics*, 18(1):15–24, 2022.

[159] Derek F Jackson Kimball, Alexander O Sushkov, and Dmitry Budker. Precessing ferromagnetic needle magnetometer. *Physical Review Letters*, 116(19):190801, 2016.

[160] Y B Band, Y Avishai, and Alexander Shnirman. Dynamics of a magnetic needle magnetometer: Sensitivity to landau-lifshitz-gilbert damping. *Physical Review Letters*, 121(16):160801, 2018.